Computer Simulation of Shock Waves in Condensed Matter

Matthew Raymond Farrow

Submitted for the Degree of
Doctor of Philosophy

Department of Physics
University of York

July 2009

Abstract

This thesis documents research into shock waves in solids by using computer simulation techniques. The domain explored was at the atomic scale. Femto-second molecular dynamics simulations employing periodic boundary conditions were used with well-known interatomic empirical potentials to model the atomic interactions as a shock wave was applied to the system. It was found that to create a stable shock wave in a computer simulation, all the atoms in the system had to be given a centre-of-mass velocity towards a plane parallel to the desired shock front. A momentum mirror was used that reversed the momentum of the atoms that reached it, and thereby created a shock wave in the system that propagated away from the momentum mirror. The simulation was completed when the shock wave reached the far surface of the system. The technique was used successfully in Lennard-Jonesium systems, although it was found that the strength of the shock waves began to probe the unphysical region of the Lennard-Jones empirical potential. Shock wave generation in quartz (silicon dioxide) highlighted a number of issues. Firstly, using the well-used interatomic potential of van Beest, Kramer and van Santen (BKS) gave β-quartz as the lowest stable phase at zero kelvin, as opposed to α-quartz which is known to be the most stable phase at this temperature. Hydrostatic compression simulations were performed and at a pressure of 8 GPa the phase of quartz transformed back to α-quartz. The second issue was that a dipole moment was present in the shock wave simulation cell that resulted in an unstable system due to long range Coulomb forces. These Coulomb forces were calculated by Ewald summation and a correction for simulation cells similar to ours had been proposed by Yeh and Berkowitz. The final issue found was that at pressures over 50 GPa the resulting interatomic distance of pair-potential term of the BKS potential turns over and becomes infinitely attractive. This unphysical effect was overcome using a polynomial fitted to the point of inflection. Using this extension to the BKS potential at high pressures and the Ewald summation correction, shock wave simulations through quartz were successfully performed and the results showed that at the very high shock pressures that are generated quartz undergoes amorphisation.

The extension to the BKS potential had no precise justification as to its form and so the pair-potential part of the BKS potential was re-parameterised using Density Functional Theory *ab initio* calculations. This resulted in an improvement over the original BKS potential as it corrected the problem of β-quartz being the lowest stable phase, as the re-parameterised potential correctly gave α-quartz as the most stable phase. It also allowed calculations to be performed up to 70 GPa without requiring the use of an extension.

Contents

List of Figures

List of Tables

Declarations

I declare that the work presented in this thesis, except where otherwise stated, is based on my own research and has not been submitted previously for a degree at this or any other university. Parts of the work reported in this thesis have been published in:

M.R.Farrow and M.I.J.Probert, "Shock wave simulations of alpha-quartz", *Proceedings of New Models and Hydrocodes for Shock Wave Processes in Condensed Matter* (2008)

M.R.Farrow and M.I.J.Probert, "Shock compression of α-quartz" *(in preparation)*

Signed

Matthew Raymond Farrow

Acknowledgements

I would like to thank my supervisor, Dr. Matthew Probert for his invaluable time, patience and guidance, without which I would have been unable to finish. I am also eternally grateful for the help from Dr. Philip Hasnip; for his insight, his useful comments and making sure I did not overdose on coffee by selflessly drinking many a cup from our rather large carafe! Thanks to my good friend Tomas Stanton, who patiently listened to me rant and rave when things did not go to plan. Finally I would like to thank my wife-to-be Sarah, who had to endure many a lonely night whilst I prepared this thesis.

I gratefully acknowledge that this work would not have been possible without funding from the Engineering and Physical Sciences Research Council (EPSRC).

Matthew R. Farrow
June 2009

For my Mum and Dad

Chapter 1

Introduction

1.1 Why use shock wave simulations?

The field of shock wave physics is an active and vibrant one, with much research ongoing to understand the mechanisms of material failure under impact (due to a shock wave), and the use of shock waves to make materials harder and stronger. When a material is subjected to a shock wave, it is rapidly and dynamically altered. The process is highly anisotropic and brings about significant changes in the structure of the material. These changes are difficult, if not impossible to achieve by static compression alone because the material has time for atomic re-structuring, time for the temperature to equilibrate and, for solids, any stresses to dissipate. Recent advances in computer simulation techniques have opened up many areas of science to a new kind of experimentation – that is, the computer simulation. The power of computer simulation lies in its ability to be performed over and over again, at very little extra cost compared with experimental testing and on any time scale. With the ongoing advancement of computer hardware, many calculations that seemed impossible many years ago, or at least, would take many days on the computer mainframes of old can now be performed relatively quickly on a desktop computer. Therefore researchers are devising bigger, and more complex problems to tackle – that tax even today's impressive supercomputers' number crunching ability. Shock wave science is one of those areas that can only gain from bigger computer hardware. That said, not all problems require a supercomputer to be answered and it is hoped that this will be evident from this thesis.

1.2 Shock waves in solids

The foundations of the science of shock waves were laid by Rankine [1869] (1820-1872) and Pierre-Henri Hugoniot[1] (1851-1889) in their studies of discontinuities through fluids. Lord Rayleigh's [Rayleigh, 1910] review showed that the equations of Hugoniot and Rankine where actually the same, albeit from different starting points. These are now referred to as the Rankine-Hugoniot equations and they describe the passage of a steady wave through a fluid.

Shock waves in solids can also make use of these equations, provided that the strength of the shock wave exceeds the yield strength of the solid. For solids, the stresses and internal pressures in shock compression can range from a few gigapascals (GPa) up to terapascals (TPa). Such intense compressive forces happen over very small time-scales (a few nanoseconds) and can bring about huge changes in the material. The mechanisms that govern these changes are of intrinsic value; predictive models are increasingly being used in place of the more expensive experimental methods to design novel high-performance materials.

Shock compression (whether experiment or simulation) allows for the calculation of the Hugoniot. The Hugoniot is a relationship between thermodynamic parameters of states that are reached during shock compression and is used in the construction of the equations of state of the material. Although a complete description of the processes that occur under high-pressure in condensed matter is still far from understood, the complexity of the problem has led researchers to investigate many different time-scales and spatial scales. The atomic scale is ideal for studying shock waves due to the short time-scales involved during shock compression and the fact that shock waves exhibit rapid rises in velocity, density and pressure, with profile widths that can be as small as just a few interatomic lattice spacings.

Molecular dynamics simulations, where Newton's equations of motion are solved for large numbers of atoms on a computer have been shown to give good agreement with experimental data even though the numbers of atoms being simulated is far smaller than one would expect to find in an experimental sample. This powerful technique is also ideal for capturing the dynamic interaction of shock waves with matter.

This work is focussed on the atomic scale using molecular dynamics. Much work has been done, and continues to be done, at the mesoscale using continuum mechanics techniques, and at the macroscale via experimental shock compression. Although these are outside the scope of this thesis, an interested reader is referred to an excellent review by Davison and Graham [1979] and the recent book "Fundamentals of Shock Wave Propagation in Solids" by Davison [2008]. It is the author's opinion that a complete description of shock waves will require knowledge of the processes in each of the spatial scales and interactions between atomic scale, mesoscale and macroscale

[1] Chéret [1992] has written an excellent biography of Hugoniot

researchers in these fields will be essential.

1.2.1 Layout of thesis

This thesis is organised as follows: The remainder of Chaper 1 will discuss the the experimental and simulation work that has led to the modern understanding of shock compression in solids. Chapter 2 will introduce the theoretical background to the work presented, and Chapter 3 will present the computer simulation techniques that have been used extensively in obtaining the results presented herein. Chapters 4 and 5 present the results of simulations that the author has performed on Lennard-Jonesium and quartz materials, respectively. In Chapter 6, the interatomic potential for quartz is re-parameterised using *ab initio* Density Functional Theory calculations. A summary and conclusions are drawn in Chapter 7, along with recommendations for future work.

1.2.2 Scope of this thesis and role of the author

This thesis covers the art of computer simulation applied to shock wave compression of solid matter. The author has developed the methodology and written the software to enable shock wave compression simulations. The software base was already established within the CASTEP [Segall *et al.*, 2002] plane-wave density functional theory code, however significant alterations were undertaken by the author to allow for atomistic shock wave simulations to be performed. Development of the analysis tools, the shock wave methodology and the re-parameterisaton of the empirical potential for quartz was also the author's own work.

1.3 Review of previous work

In this section a review of the experimental approaches to shock wave creation will be given to highlight some of the techniques employed in creating and measuring these short-lived and dynamic events. The section will conclude with a review of shock wave simulation; from its early inception using one-dimensional systems through to the most recent, billion-atom simulations.

1.3.1 Shock wave experiments in solids

Experimental shock waves in solids are most commonly created by using explosives or by a projectile impact driven by a compressed gas delivery system (known as a gas-gun). These experiments can form shock waves of pressures up to a few hundreds

of GPa. Extremely high pressures of up to 10 TPa have been generated by using underground nuclear explosions [Trunin, 1998] (however these are no longer possible due to the ban on nuclear testing).

There are two main experimental methods for generating shock waves using explosives that have been developed [Rice *et al.*, 1958; Altshuler *et al.*, 1958]. The first method is known as the "free surface" method. In this method the solid (typically a metal) is placed into contact with explosives such as TNT (trinitrotoluene) or a mixture of TNT and RDX (Cyclotrimethylenetrinitramine). For moderate pressures (pressures up to a few tens of gigapascals) the free-surface approximation can be used which states that the velocity of the free surface after unloading is approximately double the particle velocity. Figure 1.1 shows the motion in the shock plane with time. After detonation, a shock wave (line AB) travels through the sample and emerges at the free surface (point B) whilst a reflected wave (AC) travels back through the explosives. Line AD is the velocity of the contact surface between the sample and the explosive and is equal to the sample's particle velocity. After reaching the free surface, an unloading wave travels back into the sample (BE) and the boundary of the sample (BF) moves off with double the particle velocity. Pressures of 3.5 GPa have been obtained in iron using this method [Rice *et al.*, 1958]. It is worth noting that the free surface method is unsuitable for porous sample materials as the unloading velocity is considerably less than the particle velocity and the free-surface approximation no longer holds [Zel'dovich and Raizer, 2002].

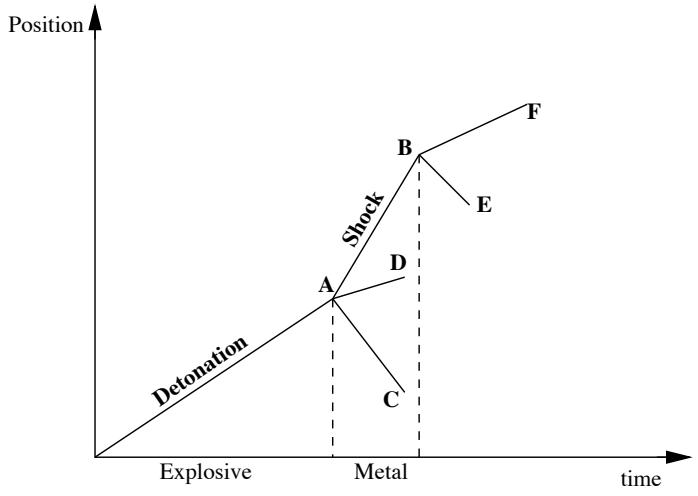

Figure 1.1: Position-time diagram for "the free surface" method of shock wave generation. Line AD is the velocity of the contact surface. After detonation, a shock wave propagates along line AB and on reaching the free surface, the boundary (BF) moves off at double the particle velocity.

The second method is suitable for all materials and is known as the "collision" method (sometimes called the momentum transfer method) as it involves accelerating a plate known as the flyer-plate (or driver plate) which is initially in contact with explosives

into a target sample. A typical experimental schematic is shown in figure 1.2. Pressures up to 40 GPa can be obtained using this experimental methodology [Altshuler, Krupnikov, and Brazhnik, 1958]. In both experiments, the shock waves are generated by a lens-like combination of fast and slow detonating explosives that create a planar detonation wave that can be flat to millimetre precision [Rice *et al.*, 1958]. In addition to the two main methods described above, shock waves are also created by accelerating a projectile or a flyer-plate into the target sample by means of a gas-gun [Setchell, 2003] or by using strong magnetic fields [Knudson *et al.*, 2001].

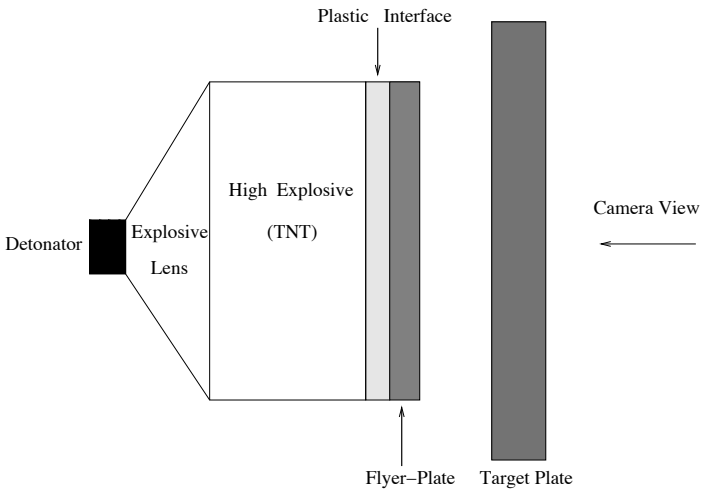

Figure 1.2: Typical schematic of an explosive-driven flyer-plate shock wave experiment.

The particle velocity and the shock-front velocity can be measured by electrical pin-contactors placed at known distances inside the sample. These are set to send a pulse to an oscilloscope as the shock wave passes. Thus using these measurements along with the free surface approximation, the Hugoniot can be derived from the conservation laws of mass and momentum. Another method of shock front measurement is by the use of high-speed photography: as the shock front exits the free surface it drives a shock wave into a gas (argon is typically used) placed in front of the surface. A Lucite block[2] is placed between the gas and the camera so that the shock wave in the gas is reflected back and forth causing luminescence due to heating. Timing information is obtained by placing slits in a plate and sweeping a camera normal to the slits at a predetermined speed. Most modern shock wave experiments utilise lasers to measure particle velocity using a technique called Velocity Interferometer System for Any Reflector (VISAR). VISAR works by reflecting a probe laser off the free surface of the target sample. When the shock front reaches the free surface, the probe laser is frequency-shifted due to the Doppler effect. This frequency-shifted laser beam is directed into an interferometer that produces temporally resolved data. Photomultipliers

[2]a transparent thermoplastic acrylic resin with ability to transmit 98% of visible light

and electronic streak cameras are used as a means of recording data and allow shock wave velocities to be determined.

The collision method was used by Rice *et al.* [1958] and McQueen and Marsh [1960] in experimental shock wave generation in metals while working at Los Alamos Laboratory. Plastic was inserted between the TNT explosives and the flyer-plate to prevent the latter breaking up during the experiment. They fitted their data to the Mie-Grüneisen equation of state and concluded that the following linear equation for a Hugoniot is a good approximation:

$$u_s = a + bu_p \tag{1.1}$$

where u_s is the shock velocity, u_p the particle velocity in the sample and a and b are constants. A quadratic equation of the form:

$$u_s = a + bu_p - cu_p{}^2 \tag{1.2}$$

where a, b and c are constants, is sometimes used for high-pressure experiments [Prieto and Renero, 1970].

The equation of state of matter at high-pressure can also be obtained from shock waves generated with the use of lasers [Koenig *et al.*, 1995]. For example, Silva *et al.* [1997] have used laser generated shock waves to study the equation of state of matter to pressures of 200 GPa. They used a laser focussed onto a target that caused ablation that drove a shock wave through the sample. Remington *et al.* [2006] provides an in-depth review of the use of lasers for generating high-pressures and temperatures as well as hydrodynamic computer simulations. Advances in x-ray techniques allow the material structure to be dynamically probed [Kalantar *et al.*, 2005; Woolsey, 1994; Wark *et al.*, 1989]. This allows the comparison between structures generated during a computer simulation and those of experiment, an important verification for the accuracy of computer simulation.

1.3.2 Shock wave simulations

The macroscopic or continuum scale uses phenomenological descriptions of material response such as dynamic yield strength and phase changes. It is often thought that the reason for failure and phase change effects nucleate at much smaller spatial scales. Such changes occurring at the atomic scale rapidly grow to larger dimensions of the mesoscale scale and then onto the macroscopic scale. Each scale can resolve particular details; such as the dislocations in the material structure at the atomic scale, whereas at the mesoscale one can resolve the effects of grain boundaries and crack propaga-

tion. Atomic scale simulations allow the investigation of the underlying structure of the material. At this scale, the structural deformation of a material as a shock wave passes through can be directly analysed and the mechanism of the subsequent material failure can be determined. This could be due to defects in the material structure, to dislocations, or due to a phase change [Holian and Lomdahl, 1998; Bringa *et al.*, 2004; Barmes *et al.*, 2006]. Therefore atomic scale is well suited to study shock waves but one must still be mindful of its limitations: the short length and time scales put an upper bound on the problems that can be studied because of limited computer resources [Kadau *et al.*, 2005]. It is surprising therefore to find that even at such small length and time scales, macroscopic properties such as temperature and density can be calculated quite accurately [Frenkel and Smit, 2002; Haile, 1997].

The passage of a shock wave is a complicated phenomena that involves different time and length scales, therefore a multiscale approach is required to completely understand what is happening in the material. The results of atomistic scale simulations could be used as inputs to mesoscale simulations to explore longer length and timescale phenomena, such as fracture and spalling, as well as things like shock unloading and elastic-plastic flow. The output of mesoscale simulations can, in turn, be used as inputs to continuum calculations for flow rates and deformations. This thesis is concerned with the atomic scale and so will review the state of the art in this spatial domain.

1.3.2.1 Atomistic shock wave simulations

Computational power by the mid-1970s became sufficient to perform Molecular Dynamics (MD) simulations of shock waves. Researchers first used MD to simulate shock waves using simple interatomic potentials (Morse, Toda and Lennard-Jones) to describe the interactions between atoms [Paskin *et al.*, 1977; Tsai and Macdonald, 1973, 1978; Holian and Straub, 1978; Straub *et al.*, 1979]. The shock waves were initiated by imparting a constant velocity to the front plane of atoms to act as a compressive piston that drove a shock wave ahead. Holian and Straub [1979] showed that a perfect Lennard-Jones type crystal has a steady shock wave, provided the initial temperature is above zero. At zero kelvin, the waves are always found to be non-steady and this resulted in a shock wave thickness that grew linearly with time. Above zero, the shock thickness approaches a constant value. As a general rule, shock thickness is inversely proportional to shock strength, or strain, ε [Holian, 2002]

$$\varepsilon = 1 - \frac{V}{V_0} = 1 - \frac{\rho_0}{\rho} = \frac{u_p}{u_s}$$

In the 1970's, Bill Hoover pioneered the method of Non-Equilibrium Molecular Dynamics (NEMD) [Ashurst and Hoover, 1975]. This technique applies driving forces and constraints at the atomic scale in order to simulate laboratory conditions. These in-

duce non-equilibrium (and ideally, steady-state) flows in mass, momentum and energy. As a consequence of the atomistic scales of the samples under investigation, the strain rates are much larger than those observed in laboratory experiments. Shock waves were ideal phenomena to study using this technique and early shock wave NEMD simulations were performed on dense liquids [Holian *et al*., 1980] and showed good agreement with the well-established continuum mechanics simulations.
Holian [1988] found three regimes a system can be in when shocked; these are in decreasing order of shock strength:

- Steady overdriven plastic wave
- Steady plastic wave preceded by a non-steady elastic precursor
- Unsteady elastic wave

The first two regimes are characterised by shear-stress relaxation and atomic re-arrangement where the plastic wave is at most only a few lattice spacings thick, and the spacing between slipped regions decreased with decreasing shock strength. Holian also identified that the elastic and plastic components of strain rate are related to compressive and dissipative flows, respectively. For 3D solids, dissipative motion occurs in the transverse direction to the shock.

There are other methods besides moving a piston into a simulation cell to generate a shock wave. Kress *et al*. [1999] performed NEMD simulations of shock waves in methane and used contracting periodic boundary conditions in the direction of the shock wave. This method creates a shock wave by moving the boundaries towards each other with the required piston velocity and this creates a symmetrical pair of shock waves moving towards each other. A similar technique to this involves colliding two identical systems. This is similar to the experimental flyer-plate experiments as it creates two shock waves propagating away from the impact plane in both systems. However, the drawback of both the above methods is that it requires twice as many atoms as the piston method and hence will take at least twice the computational effort. A method similar to the piston method was developed by Holian and Lomdahl [1998] called a "Momentum mirror". This places a perfectly reflecting surface at the origin and the particles in the system are moved toward it with the desired piston velocity. This is equivalent, by Galilean invariance, to a piston moving into the system. The momentum mirror approach is discussed in more detail in section 3.8.1. Figure 1.3 shows an illustration of the different shock wave generating methods discussed above.

Zhakhovskiĭ *et al*. [1999] have performed shock wave simulations on Lennard-Jones crystals using MD and a technique called a "moving analytical window". This technique allows the study of the shock front of the shock wave by using a moving window

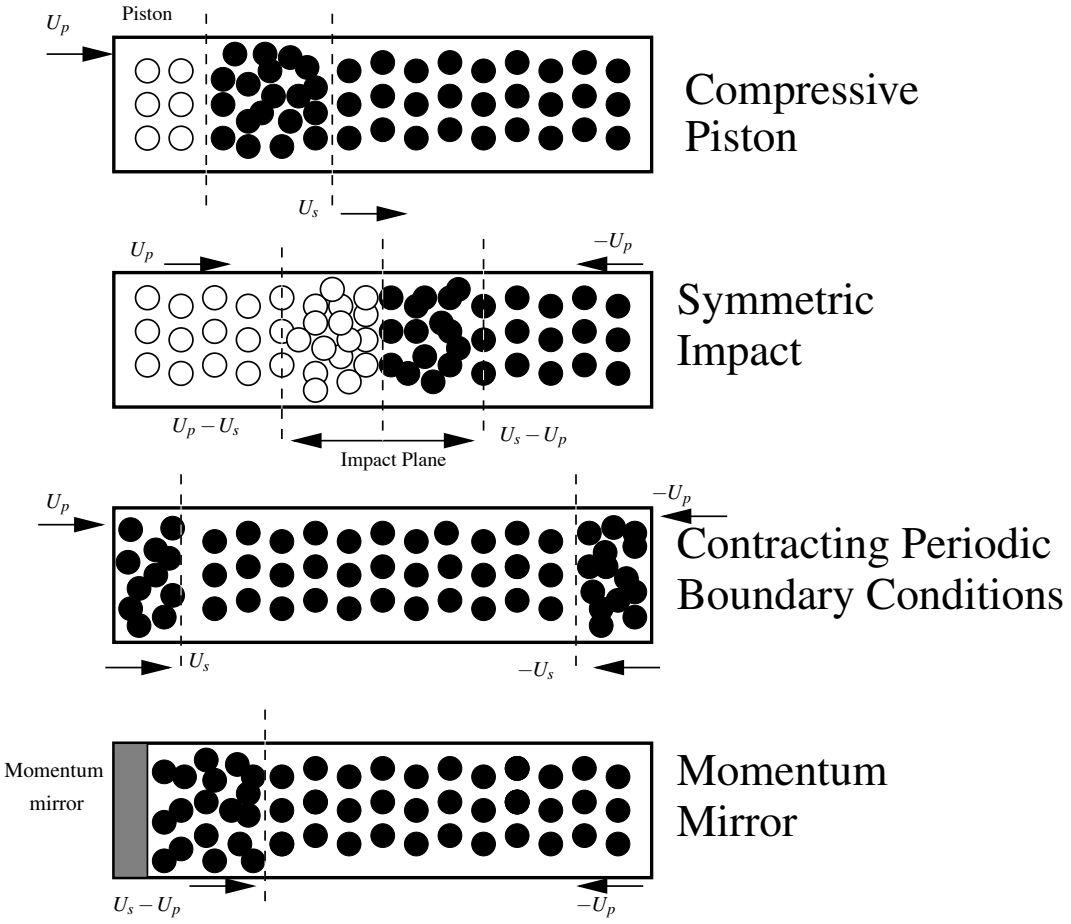

Figure 1.3: An illustration of the four methods of generating shock waves: Compressive piston, symmetric impact, contracting periodic boundary conditions and the momentum mirror. U_p is piston velocity and U_s is the shock velocity.

centered on the shock front. This would normally require an extremely long simulation cell in order to perform any quantitative analysis, however the authors keep their simulation cell constant by removing the leftmost planes of atoms from the "piston" as it moves with constant velocity into the simulation cell and appending them to the rightmost boundary. This allows for long-time averages of the shock front to be constructed.

An alternate method for shock wave simulation has been proposed by Maillet *et al.* [2001] which uses what is termed a Hugoniostat. This is a form of equilibrium MD and allows a system to quickly find the shocked state of the material. The Hugoniot relations are used as constraints on the equations of motion. The Hugoniostat method involves compressing the sample to the final shocked volume instantaneously at time zero, then coupling the system to a thermostat constrained by the Hugoniot relations so that a state on the Hugoniot is guaranteed to be achieved. The authors performed both NEMD and MD with a Hugoniostat and claim that the results are similar, but with an 8-fold decrease in computation time. An improved Hugoniostat was developed by Ravelo, Holian, Germann, and Lomdahl [2004] that compresses the sample

over a short time-period instead of instantaneous compression, by means of a barostat. This method captures the finite strain-rates that a system undergoes during shock compression. Both methods have shown they can re-create the shocked state [Kadau *et al*., 2005].

Atomistic simulations on silicon were performed by Oleynik *et al*. [2006] using NEMD with piston velocities $1 < u_s < 4$ km/s to cover the range from subsonic to supersonic (speed of sound in silicon is 2.2 km/s). Oleynik used an alternative to the momentum mirror in which the "mirror" was replaced by a repulsive potential wall. Four regimes were observed compared with Holian's three. The extra regime observed occured after the strongest shock regime of an overdriven plastic wave. This regime they called the "anomalous elastic" regime.

The use of supercomputers has allowed for a dramatic increase in the numbers of atoms that are capable of being contained in a simulation cell. Kadau *et al*. [2005] have simulated multi-million (up to 8 million atoms) atom shock-induced phase transformation in iron using NEMD. They used up to 512 CPUs and ran for a time equivalent for a shock to travel $2\mu m$. Most recently, Timothy Germann and co-workers have performed simulations at the Los Alamos National Laboratory on the supercomputer "BlueGene/L" using a billion atoms. The simulations ran for between 24 and 48 hours on 212,992 CPUs. If one was to be able to perform the same calculation on a single CPU it would take over a millennium to complete.

1.4 Summary

The future of shock wave simulation lies with the ability to utilise large-scale supercomputer resources. It is evident that shock wave compression is a vibrant and active field of research for both experimentalists and theorists alike. With the advances of computational power larger and larger systems will be able to be simulated which will allow the mesoscale continuum mechanics problems such as crack propagation to be modelled at the atomic scale. This overlap will bridge the gap between atomistic and mesoscale simulations and therefore can help enhance our understanding of the dynamic and short-lived properties of shock waves.

References

L. V. Altshuler, K. K. Krupnikov, and M. I. Brazhnik. Dynamic compressibility of metals under pressures from 400,000 to 4,000,000 atmospheres. *Soviet Phys. JETP (English Transl.)*, 7:614–619, 1958.

W. T. Ashurst and W. G. Hoover. Dense-fluid shear viscosity via nonequilibrium molecular- dynamics. *Phys. Rev. A*, 11:658–678, 1975.

F. Barmes, L. Soulard, and M. Mareschal. Molecular dynamics of shock-wave induced structural changes in silica glasses. *Phys. Rev. B*, 73:224108, 2006.

E. M. Bringa, J. U. Cazamias, P. Erhart, J. Stolken, N. Tanushev, B. D. Wirth, R. E. Rudd, and M. J. Caturla. Atomistic shock Hugoniot simulation of single-crystal copper. *J. Appl. Phys.*, 96:3793–3799, 2004.

R. Chéret. The life and work of Pierre-Henri Hugoniot. *Shock Waves*, 2:1–4, March 1992.

L. Davison. *Fundamentals of Shock Wave Propagation in Solids*. Springer-Verlag, Berlin Heidelberg, 2008. ISBN 978-3-540-74568-6.

L. Davison and R. A. Graham. Shock compression of solids. *Phys. Rep.-Rev. Sec. Phys. Lett.*, 55:255–379, 1979.

D. Frenkel and B Smit. *Understanding Molecular Simulation,*From Algorithms to Applications. Academic Press, 2002. ISBN 0-12-267351-4.

J.M. Haile. *Molecular Dynamics Simulation, Elementary Methods*. Wiley-Interscience, John Wiley and Sons inc., 1997. ISBN 0-471-18439-X.

B. L. Holian. Modeling shock-wave deformation via molecular-dynamics. *Phys. Rev. A.*, 37:2562–2568, 1988.

B. L. Holian and P. S. Lomdahl. Plasticity induced by shock waves in nonequilibrium molecular dynamics simulations. *Science*, 280:2085–2088, 1998.

B. L. Holian and G. K. Straub. Molecular-dynamics of shock-waves in one-dimensional chains. *Phys. Rev. B*, 18:1593–1608, 1978.

B. L. Holian and G. K. Straub. Molecular-dynamics of shock-waves in 3-dimensional solids - transition from nonsteady to steady waves in perfect crystals and implications for the Rankine-Hugoniot conditions. *Phys. Rev. Lett.*, 43:1598–1600, 1979.

B. L. Holian, W. G. Hoover, B. Moran, and G. K. Straub. Shock-wave structure via non-equilibrium molecular-dynamics and Navier-Stokes continuum mechanics. *Phys. Rev. A*, 22:2798–2808, 1980.

B.L. Holian. What is a shock wave? - The view from the atomic scale. In Yasuyuki Horie, Lee Davison, and Naresh N. Thadhani, editors, *High-Pressure Shock Compression of Solids VI*, chapter 4, pages 149–166. Springer-Verlag, 2002. ISBN 0-387-95532-1.

J.N. Johnson and R. Chéret, editors. *Classic Papers in Shock Compression Science*. Springer-Verlag,New York, 1998. ISBN 0-387-98410-0.

K. Kadau, T. C. Germann, P. S. Lomdahl, and B. L. Holian. Atomistic simulations of shock-induced transformations and their orientation dependence in bcc Fe single crystals. *Phys. Rev. B*, 72:064120, 2005.

D. H. Kalantar, J. F. Belak, G. W. Collins, J. D. Colvin, H. M. Davies, J. H. Eggert, T. C. Germann, J. Hawreliak, B. L. Holian, K. Kadau, P. S. Lomdahl, H. E. Lorenzana, M. A. Meyers, K. Rosolankova, M. S. Schneider, J. Sheppard, J. S. Stölken, and J. S. Wark. Direct observation of the $\alpha - \varepsilon$ transition in shock-compressed iron via nanosecond x-ray diffraction. *Phys. Rev. Lett.*, 95(7):075502, Aug 2005.

M. D. Knudson, D. L. Hanson, J. E. Bailey, C. A. Hall, J. R. Asay, and W. W. Anderson. Equation of state measurements in liquid deuterium to 70 GPa. *Phys. Rev. Lett.*, 87 (22):225501, Nov 2001.

M. Koenig, B. Faral, J. M. Boudenne, D. Batani, A. Benuzzi, S. Bossi, C. Remond, J. P. Perrine, M. Temporal, and S. Atzeni. Relative consistency of equations of state by laser driven shock waves. *Phys. Rev. Lett.*, 74(12):2260–2263, 1995.

J. D. Kress, S. R. Bickham, L. A. Collins, B. L. Holian, and S. Goedecker. Tight-binding molecular dynamics of shock waves in methane. *Phys. Rev. Lett.*, 83:3896–3899, 1999.

J. B. Maillet, M. Mareschal, L. Soulard, R. Ravelo, P. S. Lomdahl, T. C. Germann, and B. L. Holian. Uniaxial Hugoniostat: A method for atomistic simulations of shocked materials. *Phys. Rev. E*, 6302:016121, 2001.

R. G. McQueen and S. P. Marsh. Equation of state for 19 metallic elements from shock-wave measurements to 2 megabars. *J. Appl. Phys.*, 31:1253–1269, 1960.

I.I. Oleynik, S.V. Zybin, M.L. Elert, and C.T. White. Nanoscale molecular dynamics simulation of shock compression of silicon. *CP845, Shock Compression of Condensed Matter*, pages 413–416, 2006.

A. Paskin, A. Gohar, and G. J. Dienes. Simulations of shock-waves in solids. *J.Phys. C:Solid State Phys.*, 10:L563–L566, 1977.

F. E. Prieto and C. Renero. Equation for shock adiabat. *J. Appl. Phys.*, 41:3876, 1970.

W. J. M. Rankine. On the thermodynamic theory of waves of finite longitudinal disturbance. *Trans. Roy. Soc. (London)*, 160, 1869.

R. Ravelo, B. L. Holian, T. C. Germann, and P. S. Lomdahl. Constant-stress Hugoniostat method for following the dynamical evolution of shocked matter. *Phys. Rev. B*, 70:014103, 2004.

Lord Rayleigh. Aerial plane waves of finite amplitude. *Proc. R. Soc. (London)*, A84: 247–284, 1910. (Reproduced in: [Johnson and Chéret, 1998]).

B. A. Remington, R. P. Drake, and D. D. Ryutov. Experimental astrophysics with high power lasers and z pinches. *Rev. Mod. Phys.*, 78:755–807, 2006.

M. H. Rice, R. G. Mcqueen, and J. M. Walsh. Compression of solids by strong shock waves. *Solid State Phys*, 6:1–63, 1958.

M. D. Segall, P. J. D. Lindan, M. J. Probert, C. J. Pickard, P. J. Hasnip, S. J. Clark, and M. C. Payne. First-principles simulation: ideas, illustrations and the CASTEP code. *J.Phys.:Cond. Matt.*, 14:2717–2744, 2002.

Robert E. Setchell. Shock wave compression of the ferroelectric ceramic $Pb_{0.99}\left(Z_{0.95}Ti_{0.05}\right)_{0.98}Nb_{0.02}O_3$: Hugoniot states and constitutive mechanical properties. *Journal of Applied Physics*, 94(1):573–588, 2003.

L. B. Da Silva, P. Celliers, G. W. Collins, K. S. Budil, N. C. Holmes, Jr. T. W. Barbee, B. A. Hammel, J. D. Kilkenny, R. J. Wallace, M. Ross, R. Cauble, A. Ng, and G. Chiu. Absolute equation of state measurements on shocked liquid deuterium up to 200 gpa (2 mbar). *Phys. Rev. Lett.*, 78(3):483–486, 1997.

G. K. Straub, B. L. Holian, and R. G. Petschek. Molecular-dynamics of shock-waves in one-dimensional chains. II. Thermalization. *Phys. Rev. B*, 19:4049–4055, 1979.

R.F. Trunin. *Shock Compression of Condensed Materials*. Cambridge University Press, 1998. ISBN 0-521-58290-3.

D. H. Tsai and R. A. Macdonald. Second sound in a solid under shock compression. *J.Phys. C:Solid State Phys.*, 6:L171–L175, 1973.

D. H. Tsai and R. A. Macdonald. Shock-wave profile in a crystalline solid. *J.Phys. C:Solid State Phys.*, 11:L365–L371, 1978.

Justin S. Wark, Robert R. Whitlock, Allan A. Hauer, James E. Swain, and Paul J. Solone. Subnanosecond x-ray diffraction from laser-shocked crystals. *Phys. Rev. B*, 40(8):5705–5714, 1989.

N.C Woolsey. Time resolved*, in situ,* x-ray diffraction from laser shocked solids. PhD thesis, Worcester College, The University of Oxford, 1994.

Ya. B. Zel'dovich and Yu.P. Raizer. *Physics of Shock Waves and High-Temperature Hydrodynamic Phenomena*. Dover Publications, New York, 2002. ISBN 0-486-42002-7.

V. V. Zhakhovskiĭ, S. V. Zybin, K. Nishihara, and S. I. Anisimov. Shock wave structure in Lennard-Jones crystal via molecular dynamics. *Phys. Rev. Lett.*, 83(6):1175–1178, Aug 1999.

Chapter 2

Shock waves

2.1 Introduction

This chapter presents the theory behind shock wave compression of solid matter. In order to explain the development of shock compression in solids, shock waves in fluids must first be outlined. This discussion will lead to the conservation laws for shock waves: the Rankine-Hugoniot relations. The Hugoniot will then be introduced, followed by the mechanical response of solid matter to shock loading.

2.2 Shock waves using gas dynamics

Consider the situation shown in figure 2.1 where a volume of a gas is confined in a box having density ρ_0, pressure P_0 which undergoes compression by a piston moving at velocity u_0. The laws of conservation of mass and energy and momentum allows the calculation of the unknown quantities at a later time t, namely the density ρ_1 and pressure P_1 in the compressed region.

The propagation velocity u_s of the discontinuity (shock front) can also be determined. If a mass of gas (equal to $\rho_0 u_s t$) with unit cross sectional area is set in motion by a piston at time t, then the mass occupies a volume $(u_s - u_0)t$ and so the density of the compressed gas , ρ_1 satisfies:

$$\rho_1(u_s - u_0)t = \rho_0 u_s t \tag{2.1}$$

Newton's second law tells us that the impulse due to the pressure forces will equal the change in momentum that the mass acquires. Thus the resultant force is equal to the pressure difference between the compressed gas side and that on the undisturbed side,

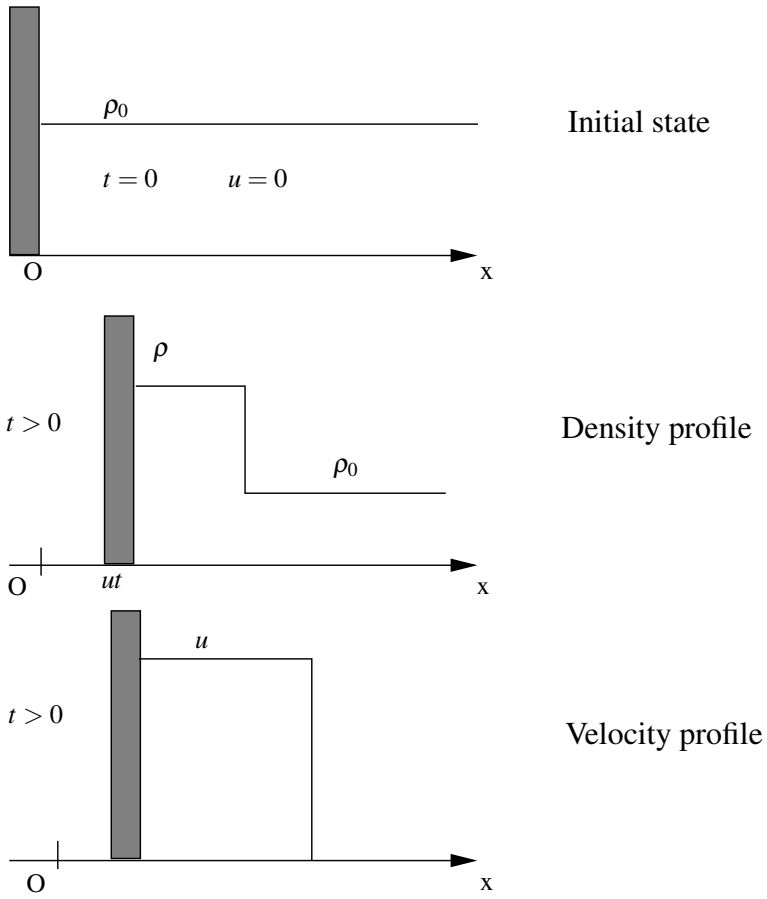

Figure 2.1: A volume of gas under compression by a piston. As time increases, a discontinuity in the density and velocity profiles is created ahead of the moving piston.

that is,

$$(P_1 - P_0)t = \rho_0 u_s u_0 t \tag{2.2}$$

The work done by the piston in compressing the gas, $P_1 u_0 t$, will equal the sum of the increase in the internal and kinetic energies,

$$P_1 u_0 t = \rho_0 u_s t \left(\varepsilon_1 - \varepsilon_0 + \frac{{u_0}^2}{2} \right) \tag{2.3}$$

where $\varepsilon(P, \rho)$ is assumed to be known. It is useful to consider the shock discontinuity as stationary. Changing frames of reference, if u_s is the propagation velocity of the shock front through the material, then $u_0 = -u_s$ is the velocity of the material into the discontinuity. Further, $u_1 = -(u_s - u_0)$ is the velocity of the material flowing out of the shock front. We can now write the conservation of mass, momentum and energy relations as

$$\rho_0 u_0 = \rho_1 u_1 \tag{2.4}$$

$$P_1 + \rho_1 {u_1}^2 = P_0 + \rho_0 {u_0}^2 \tag{2.5}$$

$$h_1 - h_0 = \frac{1}{2}({u_0}^2 - {u_1}^2) \tag{2.6}$$

where the specific enthalpy ($h = \varepsilon + P/\rho$) has been introduced in (2.6) . These relations are a set of continuity equations that are used to describe the conservation of mass, momentum and energy across the discontinuity [Zel'dovich and Raizer, 2002]. These can be re-cast into the well known Rankine-Hugoniot equations for a shock wave in a fluid:

$$V = V_0 \left[\frac{u_s - (u_p - u_0)}{u_s} \right] \tag{2.7}$$

$$P = P_0 + \rho_0 u_s (u_p - u_0) \tag{2.8}$$

$$\varepsilon = \varepsilon_0 + \frac{1}{2}(P + P_0)(V_0 - V) \tag{2.9}$$

where u_s is the shock front velocity relative to the undisturbed medium, V_0 is the initial volume, P is the pressure, u_p is the particle velocity of the medium, ε the internal energy, and ρ is the density. Figure 2.2 illustrates the use of these equations where the thermodynamic variables have been set to zero for the undisturbed fluid.

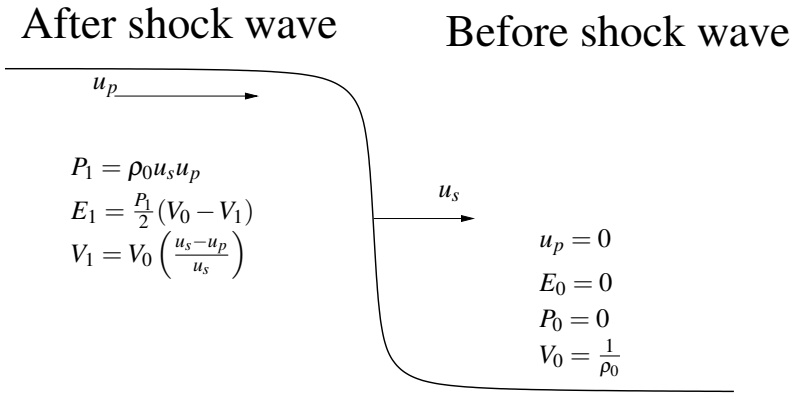

Figure 2.2: Shock wave propagating through a fluid used to develop the Rankine-Hugoniot relations.

Equations 2.7 to 2.9 relate the thermodynamic state variables on each side of the propagating discontinuity but they do not describe the way the material changes from the initial to the final state. There exists a locus of final state points given by a series of different discontinuity (or shock) strengths. This is known as a Hugoniot.

2.3 The Hugoniot

The relationship between the thermodynamic state parameters such as pressure, volume, and temperature, that represents all states that can be reached by a shock wave is known as a Hugoniot. Hugoniots for moderate pressures are well represented by the following relation [Kanel *et al.*, 2004] :

$$U_s = c_0 + a u_p \tag{2.10}$$

Where c_0 is the speed of sound in the material and a is a constant (typically between 1 and 1.7 [Kanel *et al.*, 2004]. For solids this relation holds providing the material does not undergo a phase change [Prieto and Renero, 1970]. Figure 2.3 shows an exemplar Hugoniot along with the relative positions of the isentrope. The straight line connecting the initial state with the final state after a shock is called the Rayleigh line and obeys the following relation (see Appendix A):

$$P = {\rho_0}^2 {u_s}^2 (V_0 - V) \tag{2.11}$$

The Rayleigh line gives an indication of the shock strength. A Rayleigh line with a steep gradient indicates a strong shock wave. In the limit of weak shock waves, the Rayleigh line is tangential to the isentrope of the same initial conditions and the shock speed approaches the sound speed. The isentrope is the region in the equation of state along which there is no change in entropy in the system. The Hugoniot deviates from the isentrope as the strength of the shock increases.

In figure 2.3 it can be seen that $\partial^2 P/\partial V^2 > 0$. In this case, the Rayleigh line equation would give a positive shock velocity. It is known that for a shock wave to be stable, the shock speed must be greater than the speed of sound in the material. The Hugoniot is always above the isentrope as the Rankine-Hugoniot equations demand an increase in entropy across the discontinuity, but if there is a phase transition in the material, then there is the possibility that $\partial^2 P/\partial V^2 < 0$. This means the Hugoniot was convex upwards and the Rayleigh line may have a gradient lower than the tangent at the initial conditions, hence the shock velocity would be lower than the sound velocity in the material and the shock would be unstable. It would be smoothed out into a continuous form. This property is important as it allows unloading shocks to exist.

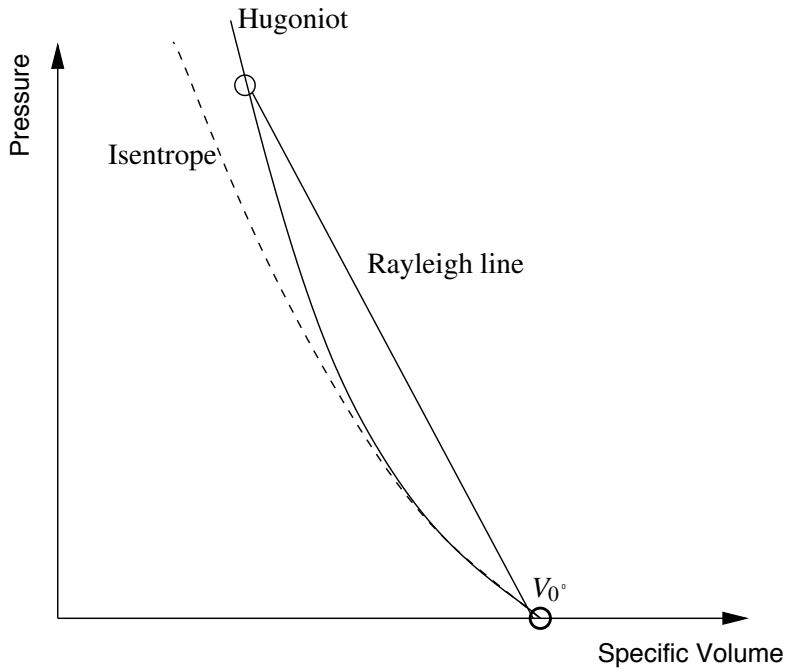

Figure 2.3: An illustration to show a Hugoniot and its relation to the isentrope and the Rayleigh line

2.4 Elastic-plastic response of solids

Interactions in solid matter are governed by interatomic forces, the extent of which is limited to the dimensions of the atoms (of the order of an angstrom). In a solid the atoms are close together and therefore interact strongly. At large distances atoms are attracted to one another and at very small distances atoms are repelled from one another (due to electronic repulsion). There exists a condition when these attractive and repulsive forces are balanced and there is no force on each atom. This is the equilibrium condition and it corresponds to a minimum in the interaction potential energy.

Let us consider two atoms in a solid at equilibrium such as can be seen in figure 2.4. The equilibrium interatomic distance is a_0.

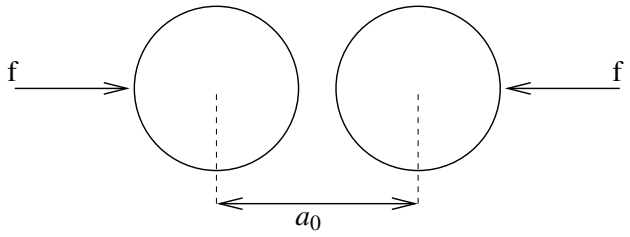

Figure 2.4: Forces between two atoms separated by a distance a_0.

Now if we apply a small force, f to these atoms to create a small displacement u, then the balance between interatomic and applied forces will give us a new equilibrium

distance a where

$$u = a - a_0 \tag{2.12}$$

As the force f is a function of distance, then

$$\mathrm{f}(u) = -\frac{d\phi(u)}{du} \tag{2.13}$$

where $\phi(u)$ is the interaction energy between the atoms. Here, the force is a function of the displacement and it is also reversible. Returning the force to zero also returns the interatomic distance to a_0. This is an example of perfectly elastic deformation. The bulk elastic behaviour is simply the effect of all the individual interactions between the atoms. As long as the deformations are small, the elastic deformation is always proportional to the applied force. This is Hooke's law.

2.4.1 Hooke's law

Hooke's law can be derived from a few considerations. Firstly, that $\phi(u)$ is a continuous function of u, so that it can be expanded as a Taylor series:

$$\phi(u) = \phi_0 + \left(\frac{d\phi}{du}\right)\bigg|_0 u + \frac{1}{2}\left(\frac{d^2\phi}{du^2}\right)\bigg|_0 u^2 + \ldots \tag{2.14}$$

Now we know that at u = 0 is the minima of the interaction energy and so $d\phi/du = 0$. The final consideration is that the displacement is much smaller than the equilibrium distance, and so higher order terms in equation 2.14 can be discarded. Therefore we now have expressions for both the interaction energy and the force:

$$\phi(u) \simeq \phi_0 + \frac{1}{2}\left(\frac{d^2\phi}{du^2}\right)\bigg|_0 u^2 \tag{2.15}$$

$$\mathrm{f}(u) = \left(\frac{d^2\phi}{du^2}\right)\bigg|_0 u \tag{2.16}$$

The force is proportional to the curvature of $\phi(u)$ at the minima (which is a constant) and also to u. Therefore $\mathrm{f} \propto u$, i.e. Hooke's law. The curvature of $\phi(u)$ can be expressed in terms of stress and strain. This is known as the elastic constant of the material. Deformations that obey Hooke's law also obey the principle of superposition. That is, forces on a body $\mathrm{f}_1 + \mathrm{f}_2$ produce displacements $u_1 + u_2$.

2.4.2 Plasticity

If the applied force causes large displacements then the higher order terms in equation 2.14 can no longer be disregarded and Hooke's law is no longer valid. The response of the material to non-elastic processes dominates and overshadows the elastic region and the atoms move past each other into entirely new equilibrium positions. This is a plastic deformation response.

2.4.3 Mechanical stress and strain

Solids under the application of external forces undergo a deformation; a change in volume or shape. The deformation is hydrostatic if the volume changes and not the shape, and deviatoric if the shape changes and not the volume. Most deformations are a combination of hydrostatic and deviatoric deformations. A deformation can be described using the stress tensor and the strain tensor. Knowledge of these tensors allows the full description of the deformation state of the material [Landau and Lifshitz, 2006]. The stress tensor, σ_{ik} where i and k represent the coordinate directions in an orthogonal reference frame (usually chosen to be x, y, and z) is the force per unit area in the direction of i, acting on an area with normal oriented along k. When $i = k$, i.e. the components σ_{xx}, σ_{yy} , σ_{zz} are known as the normal stresses. The tangential stress (or shear stress) components are when $\sigma_{xy} = \sigma_{yx}$, $\sigma_{yz} = \sigma_{zy}$, $\sigma_{zx} = \sigma_{xz}$. Cauchy discovered that the stress at any point can be defined by nine components of the stress tensor, which can further be reduced to six components by symmetry ($\sigma_{ij} = \sigma_{ji}$):

$$\sigma = [\sigma_{11}, \sigma_{22}, \sigma_{33}, \sigma_{23}, \sigma_{31}, \sigma_{12}] \tag{2.17}$$

When there are no tangential components, the principal stresses form the pressure:

$$\sigma_{11} = \sigma_{22} = \sigma_{33} = \frac{1}{3}\sigma_{ik} = -P \tag{2.18}$$

where P is said to be the hydrostatic pressure. Figure 2.5 shows a diagram of the Cauchy stress tensor on a unit volume of a body.

The strain tensor, ε_{ik} also has normal components which describe the elongation along axes, and tangential components that describe the amount of deformation. It is usual to describe states in compression as positive stresses and strains and states under tension as negative stresses and strains.

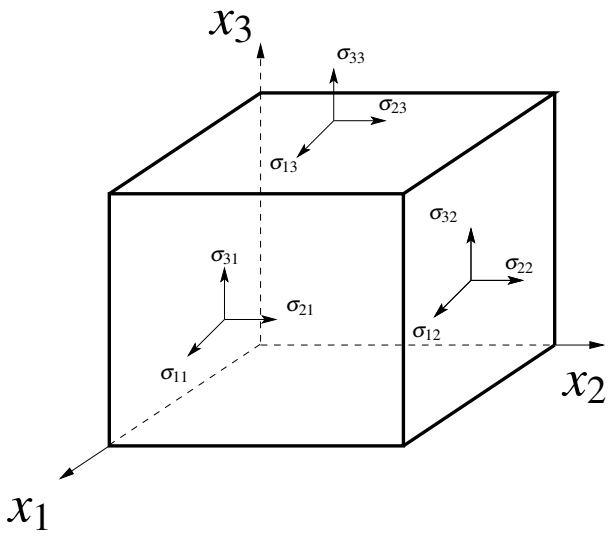

Figure 2.5: The Cauchy stress tensor components on a unit volume of a body.

2.4.4 Elastic moduli

The way that a material behaves under elastic compression can be described by elastic moduli. Three main elastic moduli are generally used and these are the bulk modulus, Young's modulus and the shear modulus. These moduli will now be described for an isotropic material. The bulk modulus of a material is a measure of its compressibility to uniform compression, i.e. it is a volumetric modulus. It is defined as:

$$K = V\frac{\partial P}{\partial V} \tag{2.19}$$

The bulk modulus is the inverse of a material's compressibility, κ. Young's modulus measures a material's resistance to deformation, it is defined as the uniaxial stress over the uniaxial strain:

$$E = \frac{\sigma}{\varepsilon} \tag{2.20}$$

Young's modulus holds only while the stress is in the region that Hooke's law holds. The shear modulus is similar to Young's modulus except it measures a material's resistance to shear. It is defined as:

$$G = \frac{\sigma_{xy}}{\varepsilon_{xy}} \tag{2.21}$$

where $x \neq y$. Figure 2.6 shows the situation where the shear modulus is used.

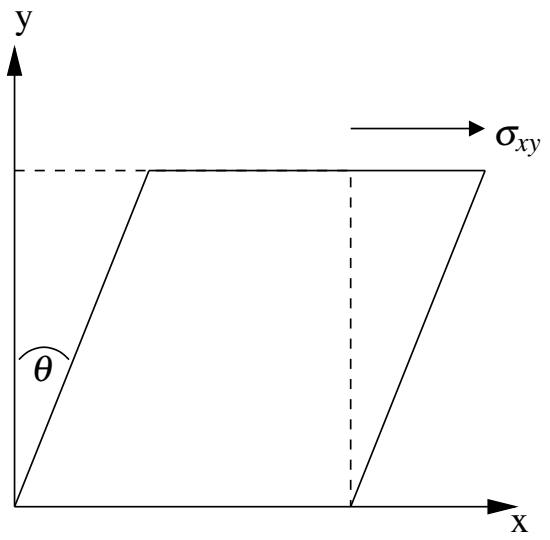

Figure 2.6: Shear modulus is used to describe the shear strain in one direction

2.4.5 Elastic constants

The general equation for Hooke's law is defined as:

$$\sigma_{ij} = c_{ijkl}\varepsilon_{kl} \tag{2.22}$$

where c_{ijkl} is the elastic constant tensor which has 81 components. However, due to symmetries of both the stress and strain tensors ($c_{ijkl} = c_{jikl} = c_{ijlk} = c_{jilk}$) and also those in the material (e.g. a cubic crystal only has three independent elements) the components of the elastic constant tensor can be significantly reduced. The simplified stress-strain relationship:

$$\sigma_{ij} = \lambda\delta_{ij}\varepsilon_{kk} + 2G\varepsilon_{ij} \tag{2.23}$$

where δ_{ij} is the Kronecker delta, λ and G are known as Lamé's parameters, with G being the shear modulus as defined above in equation 2.21. λ is related to the bulk modulus by:

$$\lambda = K - \frac{2}{3}G \tag{2.24}$$

A measure of how much a material expands sideways as it is compressed axially, is known as Poisson's ratio,ν and is defined as:

$$\nu = -\frac{\varepsilon_x}{\varepsilon_y} = \frac{\lambda}{2(\lambda + G)} \tag{2.25}$$

The above equations form a complete set of mathematical relations that capture all the deformations a material can undergo. Knowledge of the values of the above parameters allows predictions on how a material should respond under loading by a shock wave.

2.5 Response to shock wave loading

A material typically has three responses to shock wave loading . The first response is for small loads and is purely elastic; a single elastic wave propagates though the material causing little, if any, effect. These are not, strictly speaking, shock waves as there is no propagating discontinuity in the material. The second response to shock loading is a shock wave and the material also has an elastic wave however this is now followed by a plastic wave. In this context, the elastic wave is known as an elastic precursor as it precedes the plastic wave. The plastic wave causes irreversible changes in the structure of the material. This two-wave structure is called as weak shock wave. The third response is a known as a strong shock wave, where there is only the destructive plastic wave propagating in the material. Considering a shock in the weak regime, one can sub-divide the shock into three sections: the elastic wave, an unsteady "plastic precursor" and the plastic wave. The transition from an elastic to a plastic wave happens when the material is loaded beyond a critical yield stress. At this point the material deviates from its elastic response and begins to flow like a fluid. This behaviour is known as hydrodynamic deformation and happens at a stress known as the Hugoniot elastic limit (HEL). Figure 2.7 shows a pressure-volume Hugoniot of a material that is under the perfectly-elastic, perfectly-plastic approximation and the HEL.

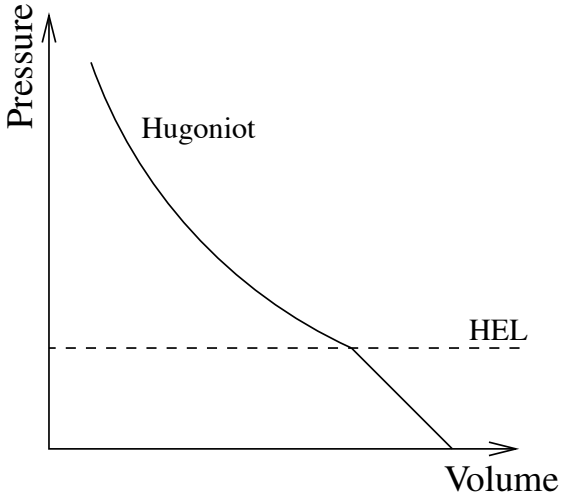

Figure 2.7: An illustration of the Hugoniot of a perfectly-elastic,perfectly-plastic material and the location of the Hugoniot elastic limit (HEL)

A material is likely to break or fracture if the stress and strain are large enough. The

underlying mechanisms for this failure can be due to imperfections in the material structure causing dislocations, bonds being broken between atoms, or a mixture of both. Figure 2.8 shows the stages that a material undergoes when subjected to stress and strain loading.

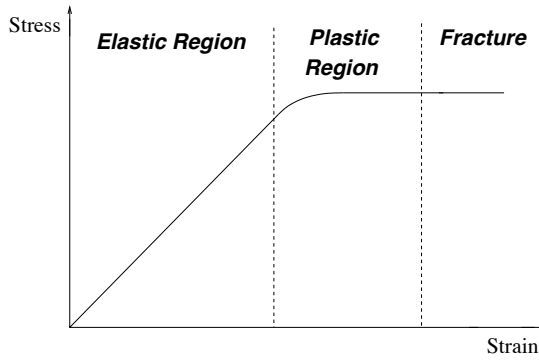

Figure 2.8: An illustration to show the elastic-plastic response of a material to stress and strain

2.6 Summary

The theory of shock compression in condensed matter is well established. Researchers have for a long time used the continuity equations to obtain good descriptions of the macroscopic processes that have been observed by experiment. Work is still ongoing however, to understand at the microscopic scale the nature of shock compression. Here is where computer simulation will play an important role in the continued research.

References

G.I. Kanel, S.V. Razorenov, and V.A. Fortov. *Shock-Wave Phenomena and the Properties of Condensed Matter*. Springer-Verlag New York Publishing, 2004. ISBN 0-387-20572-1.

L.D. Landau and E.M. Lifshitz. *Theory of Elasticity (3rd edition)*. Elssevier Butterworth-Heinemann, 2006. ISBN 0-7506-2633-X.

F. E. Prieto and C. Renero. Equation for shock adiabat. *J. Appl. Phys.*, 41:3876, 1970.

Ya. B. Zel'dovich and Yu.P. Raizer. *Physics of Shock Waves and High-Temperature Hydrodynamic Phenomena*. Dover Publications, New York, 2002. ISBN 0-486-42002-7.

Chapter 3

Computer simulation

3.1 Introduction

Computer simulation is a powerful tool for researchers. The ability to quickly and cheaply test hypotheses and ideas without having to resort to expensive laboratory testing is invaluable. However, computer simulation does have its drawbacks - the immense complexity of processes and interactions in materials means that approximations are inevitable and the limited availability of computer power requires still further approximations. That said, computer simulations are able to predict some material properties extremely accurately, such as lattice parameters to within mÅ. This chapter discusses the theory of computer simulation techniques and how they are applied to create a shock wave simulation.

3.2 Ensembles

The idea of using a thermodynamic ensemble comes from statistical mechanics. It is a way of realising many different states (or configurations) a system can be in all at once, in essence it is like performing the same experiment many times and obtaining a range of values for a measured property. Each ensemble has its own thermodynamic restrictions and these determine the ensemble's suitability for a particular problem. In the microcanonical ensemble (NVE) the number of particles, the volume, and total energy of the system is kept constant. This corresponds to an adiabatic process for an isolated system and is useful for computing the trajectories of molecular dynamics simulations. The canonical ensemble (NVT) is where the number of particles, the temperature, and the volume are kept constant and is more comparable to experiment, but does require the use of a thermostat to maintain a constant temperature. Phase boundaries and equations of state can be found using the NVT ensemble. Other ensembles

include the isothermal-isobaric ensemble (NPT), where the pressure is maintained using a barostat, and the grand-canonical ensemble (μVT) where density fluctuations in a system are maintained by coupling to a particle reservoir maintained at constant chemical potential, μ.

3.3 Molecular dynamics

Molecular Dynamics (MD) is a technique that simulates the interaction between atoms and molecules by solving the Newtonian classical equations of motion. Newton's second law states:

$$\mathbf{F_i} = m_i \mathbf{a_i} \tag{3.1}$$

where,

$$\mathbf{a_i} = \frac{\partial^2 \mathbf{r_i}}{\partial t^2} = \ddot{\mathbf{r}}_i \tag{3.2}$$

where $\mathbf{r_i}$ is the position of atom i, $\mathbf{F_i}$ is the force acting on it, m_i its mass and $\mathbf{a_i}$ its acceleration. Equation 3.1 gives a set of 2nd order differential equations to be solved subject to 3N initial conditions (N atoms with 3 degrees of spatial freedom). Newton's equations can be rewritten in Hamiltonian form:

$$\mathbf{F}_i = \frac{\partial \mathbf{p_i}}{\partial t} = \dot{\mathbf{p}}_i \tag{3.3}$$

$$\mathbf{p_i} = m_i \dot{\mathbf{r}}_i \tag{3.4}$$

where $\mathbf{p_i}$ is the momentum of atom i. As Newton's second law contains no time dependance, there exists a function of positions and velocities that is constant in time. This is called the Hamiltonian, $H(\mathbf{r}^N, \mathbf{p}^N)$. In an isolated system, total energy is conserved, thus we can define the Hamiltonian for this system as the sum of all the atoms' kinetic energy plus the potential energy associated with intermolecular interactions:

$$H(\mathbf{r}^N, \mathbf{p}^N) = \frac{1}{2m_i} \sum_{i=1}^{N} \mathbf{p_i}^2 + U(\mathbf{r}^N) = E \tag{3.5}$$

where N is the number of atoms and E is the total energy of the system. The subsequent equations of motion are:

$$\frac{\partial H}{\partial \mathbf{p_i}} = \frac{\partial \mathbf{r_i}}{\partial t} = \dot{\mathbf{r}}_i \tag{3.6}$$

$$\frac{\partial H}{\partial \mathbf{r_i}} = -\frac{\partial \mathbf{p_i}}{\partial t} = -\dot{\mathbf{p}}_i \tag{3.7}$$

These equations are equivalent to Newton's equations except that they are now 6N 1st order differential equations (3 degrees of spatial freedom plus 3 degrees of momentum freedom). Computationally, it is much easier to solve 6N 1st-order equations than 3N 2nd-order equations due to the computationally expensive integration procedures.

3.3.1 Phase space

The position coordinate of each atom can be plotted in a 3N-dimensional space, called the configuration space. In this space the axes of the 3N-dimensions are the time-dependant position vectors, $\mathbf{r_i}(t)$. Similarly, there exists a 3N-dimensional space containing the time-dependant momentum vectors, $\mathbf{p_i}(t)$, known as momentum space. These can be combined to form a 6N-dimensional space known as phase space:

$$\Gamma^N = (x_1, \ldots, x_{3N}, p_1 \ldots, p_{3N}) \tag{3.8}$$

Phase space is a useful concept and can be used describe all the possible configurations of a system - each configuration of the system is defined by the vector Γ. A trajectory in phase space defines how a system evolves over time.

3.3.1.1 Ergodicity

The ergodic hypothesis as applied to molecular dynamics simulation of an isolated system, says that the measured long-time average of an instantaneous property, X, is equal to the ensemble average [Haile, 1997].

$$\overline{X(r)} = \lim_{t\to\infty} \frac{1}{t} \int_{t_0}^{t_0+t} X(r,t')dt' = <X(r)> \tag{3.9}$$

Here we assume that t is sufficiently long that the time average no longer depends on the initial positions of the system. Therefore by taking the time averages of thermodynamic properties in a molecular dynamics simulation one would obtain the macro-

scopic measurement of that property.

3.3.2 The equations of motion

The velocities and positions of each particle in the system can be computed by integrating Newton's equations. Unfortunately, analytical solutions are not possible so numerical solutions are employed using finite difference methods. The most widely used is Verlet's algorithm, which is a third-order Störmer algorithm [Verlet, 1967]. It is derived from two Taylor series expansions of a particle coordinate; one forward in time, the other backward in time. These are summed to remove the odd-order terms resulting in the Verlet algorithm for positions:

$$x(t+\Delta t) \approx 2x(t) - x(t-\Delta t) + \frac{d^2x(t)}{dt^2}\Delta t^2 \tag{3.10}$$

The truncation error varies as $O(\Delta t)^4$ which is why it is called a third-order algorithm. Equation 3.10 contains no explicit velocities and so the Velocity Verlet algorithm was developed [Swope *et al.*, 1982]:

$$x(t+\Delta t) \approx x(t) + \frac{dx(t)}{dt}\Delta t + \frac{1}{2}\frac{d^2x(t)}{dt^2}\Delta t^2 \tag{3.11}$$

which is just a single forward-in-time Taylor expansion of truncation error $O(\Delta t)^3$. Velocities are stored at the same time from equation 3.12 which has a truncation error of $O(\Delta t)^2$.

$$\frac{dx(t+\Delta t)}{dt} \approx \frac{dx(t)}{dt} + \left(\frac{d^2x(t)}{dt^2} + \frac{d^2x(t+\Delta t)}{dt^2}\right)\frac{\Delta t}{2} \tag{3.12}$$

3.3.3 Periodic Boundary Conditions

Periodic Boundary Conditions (PBC) are needed for the simulation of large bulk systems. The typical MD simulation may have thousands or tens of thousands of atoms, but it is still dominated by the edges of the containers, which cause unwanted surface effects. PBC removes these effects by considering the system to be built from an infinite amount of blocks. Each block is a replica of the simulation cell (known as the primary cell) and these replica blocks are known as image cells and are periodically repeated in all directions to make a macroscopic sample. Atoms and images are free to move though the boundaries and enter or leave any cell, however total number of particles and total momentum is conserved. This is achieved by, for example, if an atom (or a molecule) leaves the primary cell on the right hand edge, then a particle

is introduced into the primary cell from the left hand edge with the same momentum. There is a minor issue when dealing with pairwise interactions such as forces between atoms. When computing forces, the forces exerted by atom j on atom i is:

$$\mathbf{F}_i = -\frac{\partial U(\mathbf{r}_{ij})}{\partial \mathbf{r}_i} \tag{3.13}$$

where U is the interaction potential. In order to ensure that only atom j or only *one* of its images exerts a force on atom i, the minimum image convention requires that the cut-off range for the pairwise forces is:

$$r_{cut} \leq \frac{L}{2} \tag{3.14}$$

where L is the length of the simulation box. This removes any artificial spatial correlation when using PBC. An illustration of PBC and the minimum image convention can be seen in figure 3.1.

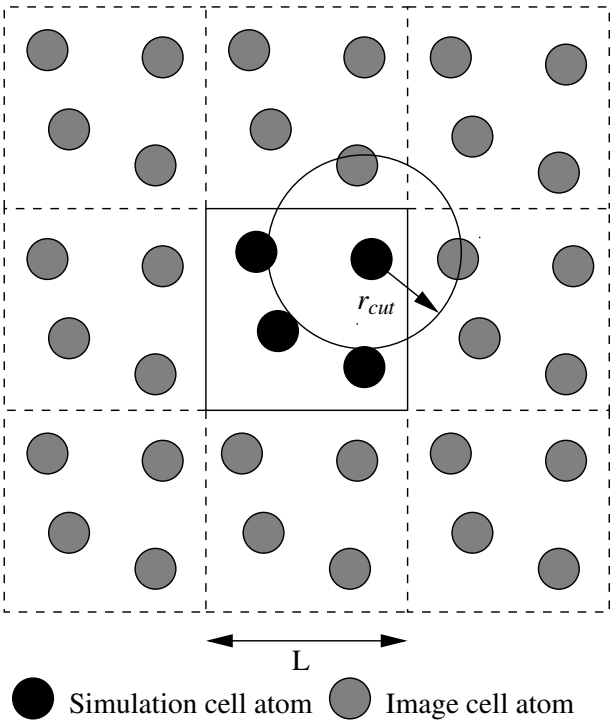

Figure 3.1: A 2D representation of Periodic Boundary Conditions. The primary simulation cell is surrounded by 8 image cells. The cut-off of the pairwise interactions, $r_{cut} \leq \frac{L}{2}$ is a requirement of the minimum image convention.

3.3.3.1 Periodicity effects

The effects of PBC for computing static properties are small and overshadowed by other systematic errors. Therefore repeating simulations with increasing numbers of atoms in the primary cell tests whether there is any periodicity effecting the system. For

dynamic properties however, especially time-correlation functions, using PBC requires sampling greater than the periodic correlation time, τ_{PBC}. A convenient means of estimating this time is from the sonic velocity v:

$$v = \frac{1}{\sqrt{\rho m \kappa_s}} \tag{3.15}$$

where ρ is the system density, m the atomic mass and κ_s is the adiabatic compressibility. Therefore the periodic correlation time is:

$$\tau_{PBC} = \frac{L}{v} \tag{3.16}$$

where L is the length of the simulation cell. Thus the larger the system, the larger the periodic correlation time.

3.3.4 Temperature

The temperature of a MD simulation is a statistical property and is related to the atoms' kinetic energy by:

$$\sum_{i=1}^{N} \frac{|\mathbf{p}_i|^2}{2m_i} = \frac{1}{2} k_B T N_{dof} \tag{3.17}$$

where N_{dof} is the number of degrees of freedom and k_B is Boltzmann's constant. The time-average of the instantaneous temperature, $< T >$ is regarded as the macroscopic temperature. The temperature in a (NVT,NPT) MD simulation is maintained by the use of a thermostat. There are a number of well known thermostats available to use for a molecular dynamics simulation, with the most popular being the Andersen and the Nosé-Hoover thermostats. An Andersen thermostat [Andersen, 1980] maintains the temperature by stochastic collisions with a heat-bath and yields good results for time-independant properties. However, for dynamical properties the Andersen thermostat should not be used as the collisions unrealistically effect the system, resulting in a decorrelation of particle velocities. Hence, the velocity autocorrelation function decays faster than it should and properties based on this (e.g. the diffusion coefficient) are effected. Nose [1984] developed a method that is both deterministic and suitable for dynamics, although the formalism that is usually used is that of Hoover [1985] and is known as a Nosé-Hoover thermostat.

A Nosé-Hoover thermostat is described by the extended Lagrangian (extended as the Lagrangian contains artificial coordinates and velocities):

$$\mathscr{L}_{Nose} = \sum_{i=1}^{N} \frac{m_i}{2} s^2 \dot{\mathbf{r}}_i^2 + \frac{Q}{2} \dot{s}^2 - g k_B T \ln s - U(\mathbf{r}^N) \tag{3.18}$$

where Q is an effective "mass" associated to the additional coordinate, s, and g is an integer parameter equal to the number of degrees of freedom of the system. From equation 3.18 it can be seen that:

$$\frac{\partial \mathscr{L}}{\partial \dot{\mathbf{r}}_i} = m_i s^2 \dot{\mathbf{r}}_i = \mathbf{p}_i \tag{3.19}$$

$$\frac{\partial \mathscr{L}}{\partial \dot{s}} = Q\dot{s} = p_s \tag{3.20}$$

The extended system creates a microcanonical ensemble of 6N + 2 degrees of freedom. Nosé introduced two sets of variables; real and virtual, and calculated the equations of motion for both. In a MD simulation, the real-variable formulation is the best one to use [Frenkel and Smit, 2002]. The equations of motion for the Nosé-Hoover thermostat can be simplified [Hoover, 1986] to yield:

$$\dot{\mathbf{p}}_i = -\varepsilon \mathbf{p}_i \tag{3.21}$$

$$\dot{\varepsilon} = \frac{1}{Q}\left(\sum_i \frac{p_i^2}{m_i} - g k_B T\right) \tag{3.22}$$

$$\frac{\dot{s}}{s} = \frac{d \ln s}{dt} = \varepsilon \tag{3.23}$$

where a thermodynamic friction coefficient $\varepsilon = s p_s / Q$ has been introduced.
The Nosé-Hoover thermostat has problems with solids, especially in small or rigid systems or in those where the interactions are harmonic (such as in near zero temperature system). This problem may be overcome by linking together successive Nosé-Hoover thermostats into what is called a Nosé-Hoover Chain [Martyna *et al.*, 1992] and then linking these chains of thermostats together to form a massive thermostat.
There is also a technique known as Langevin dynamics, named after the French physicist Paul Langevin that extends molecular dynamics away from isolated systems and attempts to emulate the effect of particles interacting with the system from the surroundings. Langevin dynamics allows the controlling of the temperature of the system through its equations of motion.

3.3.4.1 The Berendsen thermostat

It can take many time-steps for the temperature of a molecular dynamics simulation to reach equilibrium. However, there is a technique available that can push the system toward thermal equilibration. This technique is known as a Berendsen thermostat and can be used for both canonical as well as the microcanonical ensembles. The Berensden thermostat [Berendsen *et al.*, 1984] pushes a system rapidly to thermal equilibrium

at a desired target temperature. This is achieved by a re-scaling of the velocities after each time-step. It is worth noting that the Berendsen thermostat conserves momentum, but not the total energy. The temperature is controlled by a velocity scaling parameter, λ:

$$\lambda = \left[1 + \frac{\Delta t}{\tau_T}\left(\frac{T_0}{T} - 1\right)\right]^{\frac{1}{2}} \tag{3.24}$$

where T_0 is the target temperature and T is the actual temperature, Δt is the time-step of the simulation and τ_T is a coupling constant with dimensions of [time]. Care must be taken when choosing this constant as too large a value results in the system reverting to an NVE ensemble (as the Berendsen is effectively turned off) and too small a value results in large fluctuation in the system temperature which can take a long time to reach the required temperature. Once the system has reached the desired temperature, the Berendsen thermostat must be switched off and the standard ensemble methodology must be used to maintain the temperature. This is because the Berendsen thermostat has no physical association and the dynamics of the system would no longer be able to be correctly described by the statistical mechanical ensembles.

3.3.5 Pressure

The pressure is usually derived from the Virial theorem of classical dynamics where the pressure is calculated by taking one third the trace of the pressure tensor as in equation 2.18, or alternatively:

$$< P >= \frac{1}{3V}\left\langle \sum_i \left(\frac{\mathbf{p}_i^2}{m_i} + \mathbf{r}_i \cdot \mathbf{F}_i\right)\right\rangle \tag{3.25}$$

which is also invariant to the initial coordinates. However, for systems with periodic boundary conditions this form is unsuitable, as it assumes that there are walls or external forces to preserve the shape of the system. Therefore the form that is used is:

$$< P >= \frac{1}{3V}\left\langle \sum_i \frac{\mathbf{p}_i^2}{m_i} + \sum_i \sum_{j>1} \mathbf{r}_{ij}\mathbf{F}_{ij}\right\rangle \tag{3.26}$$

To perform a molecular dynamics simulation at constant pressure requires the use of a barostat. A barostat is introduced into the equations of motion similar to the method used for the Nosé-Hoover and Berendsen thermostats. For a Berendsen barostat, the

lattice parameters are scaled by a parameter χ:

$$\chi = \left[1 - \frac{\beta \Delta t}{\tau_{cell}}(P_{ext} - P_0)\right]^{\frac{1}{3}} \tag{3.27}$$

where P_0 is the calculated pressure and P_{ext} is the desired pressure, β is a measure of the system compressibility and τ_{cell} is a coupling constant.

3.3.6 Short-range forces

The short-ranged interactions between atoms can be described with the use of interatomic potentials. These models are created by curve fitting to experimental data and sometimes simulated data, such as from *ab initio* calculations, for example.

3.4 Interatomic potentials

Interatomic potentials are simple empirical functions that generate the potential energy surface of a system. The potentials can be specific to a particular property or generic for a material. Pair potentials govern the interaction between pairs of atoms and usually assume that this interaction only depends on the distance between each atom. A few specific potentials will now be discussed as they are used later in the thesis for shock wave calculations.

3.4.1 Lennard-Jones pair potential

Probably one of the most well known empirical pair potential is the Lennard-Jones potential derived by J.E. Lennard-Jones in 1924 [Jones, 1924a,b]. It has the form:

$$U(r) = k\varepsilon \left\{ \left(\frac{\sigma}{r}\right)^n - \left(\frac{\sigma}{r}\right)^m \right\} \tag{3.28}$$

where σ is the distance to the zero in $U(r)$, ε is the energy at the minimum

$$k = \frac{n}{n-m}\left(\frac{n}{m}\right)^{\frac{m}{n-m}} \tag{3.29}$$

where the integers follow $n > m$. The choice, $m = 6, n = 2m = 12$ results in the Lennard-Jones (12,6) potential [Haile, 1997]. This potential has a $1/r^6$ attractive term coupled with a $1/r^{12}$ repulsive term. The attractive term has a physical origin; from London's theory for dispersion whereas the r^{12} repulsive term is not physical - it was chosen to be numerically convenient when calculating the pairwise force:

$$\mathbf{F}(\mathbf{r}) = -\frac{\partial U(r)}{\partial r} = 24\frac{\varepsilon}{\sigma}\left\{2\left(\frac{\sigma}{r}\right)^{13} - \left(\frac{\sigma}{r}\right)^{7}\right\} \tag{3.30}$$

By convention, attractive forces are negative and repulsive forces are positive. Figure 3.2 shows a graphical form for the Lennard-Jones potential in reduced units. Reduced units are useful for computer simulations as many of the values that are held in memory are $\sim 10^{-40}$ and so numerical operations on these numbers could result in underflow or overflow. Reduced units remove this problem by choosing a set of basic units. A common (though not unique) choice for a LJ model is:

- Length = σ
- energy = ε
- mass = m (mass of atoms in the system)

using these basic units, all other units can be derived. Table 3.1 shows the conversion to reduced units for a LJ model.

Table 3.1: Reduced units conversion table

Unit	Reduced unit
temperature	ε/k_B
time	$\sigma\sqrt{m/\varepsilon}$
distance	r/σ
energy	$U(r)/\varepsilon$
force	$F(r)\sigma/\varepsilon$

If all the pair interactions are sampled during the course of a simulation then the number of samples increases with the square of the distance, this means that much computer time could be spent computing these interactions. It is much more convenient to use a truncated potential that sets the interactions between two atoms to zero for atoms that are further apart than a certain cut-off radius:

$$U(r) = \begin{cases} 4\varepsilon\left\{\left(\frac{\sigma}{r}\right)^{12} - \left(\frac{\sigma}{r}\right)^{6}\right\} & r \leq r_{cut} \\ 0 & r > r_{cut} \end{cases} \tag{3.31}$$

The step change in the energy at the cut-off radius, r_{cut}, can cause problems in the simulation as the force will have a discontinuity. This can be avoided by shifting the force so that it goes smoothly to zero at the cut-off radius and then integrating to get the corresponding energy.

$$F_{shift}(r) = \begin{cases} F(r) - \Delta F & r \leq r_{cut} \\ 0 & r > r_{cut} \end{cases} \tag{3.32}$$

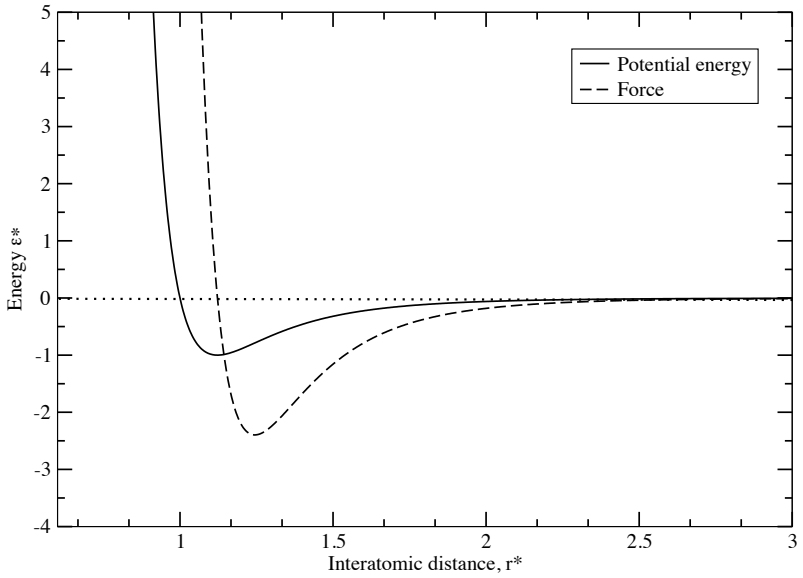

Figure 3.2: The Lennard-Jones (12,6) potential. Reduced units used: $r^* = r/\sigma$, Potential energy, $\varepsilon^* = U(r)/\varepsilon$ and Force = $\sigma F(r)/\varepsilon$)

where the shifted force, ΔF is given by:

$$\Delta F = -\left(\frac{\partial U(r)}{\partial r}\right)\Bigg|_{r_{cut}} \tag{3.33}$$

Thus the potential is:

$$U_{shift}(r) = \begin{cases} U(r) - U(r_{cut}) - [r - r_{cut}]\Delta F & r \leq r_{cut} \\ 0 & r > r_{cut} \end{cases} \tag{3.34}$$

3.4.2 Potentials for silicates

3.4.2.1 The BKS potential

A well known and used potential for silicates is the so-called BKS potential of Kramer, Farragher, van Beest, and van Santen [1991]:

$$U(r) = \sum_{i>j} \frac{q_{\alpha i} q_{\beta j}}{r_{\alpha i \beta j}} + \sum_{i>j} \left[\mathbf{A}_{\alpha i \beta j} exp(-\mathbf{b}_{\alpha i \beta j} r_{\alpha i \beta j}) - \frac{\mathbf{C}_{\alpha i \beta j}}{r^6_{\alpha i \beta j}} \right] \tag{3.35}$$

where α and β are atomic species, q_α and q_β are their charges and **A**, **b**, and **C** are con-

stants derived from curve-fitting to a mixture of experimental data and Hartree-Fock *ab initio* calculations. The author's found that the inclusion of experimental data was a necessity as their fit to *ab initio* data alone could not stabilise the predicted structures. This mixed empirical force-field approach couples the precise *ab inito* calculations on the local structure (accurately describing the nearest neighbour interactions) to the macroscopic (experimental) data. This was done by iterating between fitting the potential parameters to the *ab initio* calculations and optimising the bulk parameters (q_{Si} and b_{O-O}) by comparison with experimental elastic constants and unit-cell dimensions. Their force-field parameters, given in table 3.2 (machine precision), have been shown to be reasonably successful in describing the dynamic and structural properties of quartz (SiO_2) and some of its polymorphs [Murashov and Svishchev, 1998; Kimizuka *et al*., 2003]. The Coulomb term is usually computed using Ewald summation and form of the pair potential can be seen in figure 3.3. A notable problem can be seen with this potential if the interatomic distance between atoms becomes very small. In such an event, the BKS potential has the unphysical property of having the energy (and force) diverging to minus infinity. Therefore care must be taken when using this potential to ensure that this does not happen.

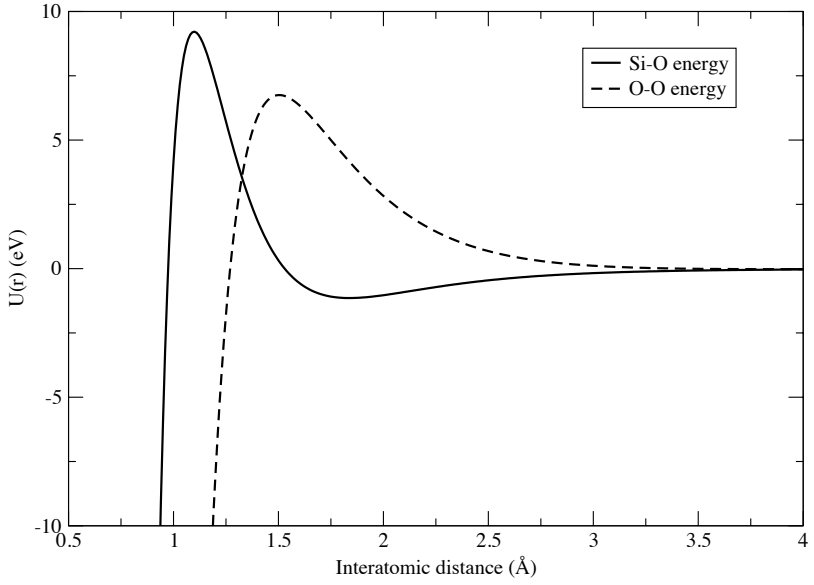

Figure 3.3: Plot of the pair part of the BKS potential.

3.4.2.2 The TTAM potential

Another well known and used potential derived by Tsuneyuki *et al*. [1988] is the so-called TTAM potential:

Table 3.2: Force-field parameters used for quartz in the BKS potential [Kramer *et al.*, 1991]

$\alpha_i - \beta_j$	$\mathbf{A}_{\alpha_i\beta_j}$ (eV)	$\mathbf{b}_{\alpha_i\beta_j}$ $(\AA^{-1})$	$\mathbf{C}_{\alpha_i\beta_j}$ $(eV\AA^6)$	q
Si-O	18003.7572	4.87318	133.5381	$q_{Si} = 2.40$
O-O	1388.77300	2.76000	175.0000	$q_O = -1.2$

$$U(r) = U_{ij}^{Coulomb}(r) + f_0(b_i + b_j)exp\left[\frac{(a_i + a_j - r)}{b_i + b_j}\right] - \frac{c_i c_j}{r^6} \tag{3.36}$$

where r is the interatomic distance and a_i is the effective radius of the ith atom with a force of $f_0 = 1$ kcal/Å/mol. This potential has the same form as the BKS, and was also parameterised using *ab initio* Hartree-Fock calculations on a tetrahedral cluster of SiO_4^{4-}. To obtain charge neutrality, the authors added 4 point charges at 1.65 Å away from the oxygen atoms and in-line with the silicon-oxygen bonds. The authors then performed a non linear fit and as there were more than one set of parameters, the authors chose the ones shown in table 3.3.

Table 3.3: Force-field parameters used for quartz in the TTAM potential [Tsuneyuki *et al.*, 1988]

α_i	a (Å)	b (Å)	c $(kcal^{1/2}\AA^3 mol^{-1/2})$	q
O	2.0474	0.17566	70.37	-1.2
Si	0.8688	0.03285	23.18	2.4

The authors found that MD simulations on α-quartz, α-cristobalite, coesite and stishovite were dynamically stable, despite the large differences in atomic structure.

3.4.3 Many-body empirical potentials

There have been a number of techniques developed to capture many-body effects, e.g. Daw and Baskes [1983]; Derlet *et al.* [1999]; Mei and Davenport [1992]; Johnson [1973]; Erkoc [1997]. One of the most well-known is the Embedded Atom Method that is used to describe metallic systems.

3.4.3.1 The Embedded Atom Method

The problem with simple pair potentials is that they fail when considering metallic systems. This is because they have no in-built many-body term that captures the electronic interactions between atoms. Stott and Zaremba [1980] introduced the concept of a quasiatom, which is an impurity ion plus its electronic screening cloud. Norskov

and Lang [1980] introduced the Effective Medium Theory that gives the interaction between an atom (or cluster of atoms) with an inhomogeneous electron system. Following these researchers work, Daw and Baskes [1983] introduced the Embedded Atom Method (EAM). This method uses a pair potential term plus a term that is dependent on the electron density of the system. It is a quick and computationally inexpensive way of capturing the atom-atom interactions. In the EAM potential the total energy has the form:

$$E_{tot} = \frac{1}{2}\sum_{i>j}\phi_{ij}(r_{ij}) + \sum_{i}F(\overline{\rho_i}) \tag{3.37}$$

$$\overline{\rho_i} = \sum_{j\neq i}\rho(r_{ij}) \tag{3.38}$$

where E_{tot} is the total energy, $\phi_{ij}(r_{ij})$ is a pairwise potential as a function of the distance, r_{ij}, between atoms i and j. F is the embedding energy, i.e. the energy required to place an atom i in an electron density $\overline{\rho_i}$, and where ρ_{ij} is the electron density function which is summed over all other atoms. [Johnson, 1988] has used the EAM for FCC metals and shows that the embedding function used in several models are essentially equivalent.

3.4.4 Long-range forces

Computing the interatomic potential up to a cut-off should be a reliable way of computing the short-ranged forces. However, this truncation of the potential can lead to serious inaccuracies. It can be shown [Frenkel and Smit, 2002] that the contribution of the missing tail of the interatomic potential (a tail correction) is estimated as:

$$U^{tail} = \frac{1}{2}\int_{r_c}^{\infty} 4\pi r^2 \rho(r) U(r)\, dr \tag{3.39}$$

where ρ is the average number density. However, unless $U(r)$ decays faster than r^{-3} then this tail correction diverges [Frenkel and Smit, 2002]. Therefore Coulombic interactions cannot be treated in this fashion. There exists a number of techniques available for computing long-range interactions, such as the Madelung Potential or the Fast Multipole Method [Greengard and Rokhlin, 1989], however the most widely used is known as Ewald summation and this method is used throughout the work in this thesis, and therefore merits further discussion.

3.4.4.1 Ewald summation

Consider an electrically neutral system of N charged particles located in a cubic unit cell. We assume the system has periodic boundary conditions. The Coulomb contribution to the potential energy is:

$$U^{Coul} = \frac{1}{2}\sum_{i=1}^{N} q_i \phi(r_i) \tag{3.40}$$

where $\phi(r_i)$ is the electrostatic potential at the position of ion i:

$$\phi(r_i) = \sum_{j,\mathbf{n}}{}' \frac{q_j}{|\mathbf{r_{ij}} + \mathbf{n}L|} \tag{3.41}$$

where the prime indicates that the sum is over all periodic images, **n**, except when $j = i$ in the primary cell, i.e. ion i interacts with all its images but not with itself. This expression can be thought of as a series of point charges, and therefore decays as $1/r$ and so is only conditionally convergent; thus is unsuitable to use in computing the electrostatic potential. Now consider what happens if we place a diffuse Gaussian charge distribution of opposite sign around each of the point charges, such that the total charge of this distribution exactly cancels q_i. This now means our system has an electrostatic potential that is due to the part of q_i that is not screened by the Gaussian charge distribution. This fraction, at long distances, rapidly decays to zero, so it is straightforward to compute the electrostatic potential by direct summation. However, we now need a correction for the screening charge. The correction takes the form of a smoothly varying compensating charge distribution located at each ion i. Figure 3.4 shows diagrammatically how the Ewald method is used to compute the electrostatic potential for a system of point charges - the point charges (left) can be considered as a set of point charges plus Gaussian screening charge cloud (right, top) plus the correction for the Gaussian charge cloud (right, bottom). The computational effort of the Ewald summation scales as $O(N^{3/2})$. Appendix B gives a detailed mathematical description of how the Ewald summation is performed.

3.5 Geometry optimisation

The starting point in any simulation is to relax the simulation cell to remove any residual stress and forces from the system. This process is know as a geometry optimisation and attempts to locate the local minimum in the potential energy surface of a system. It is an important start to any simulation as the experimentally or theoretically determined structure may not have the lowest energy configuration in a computer simulation

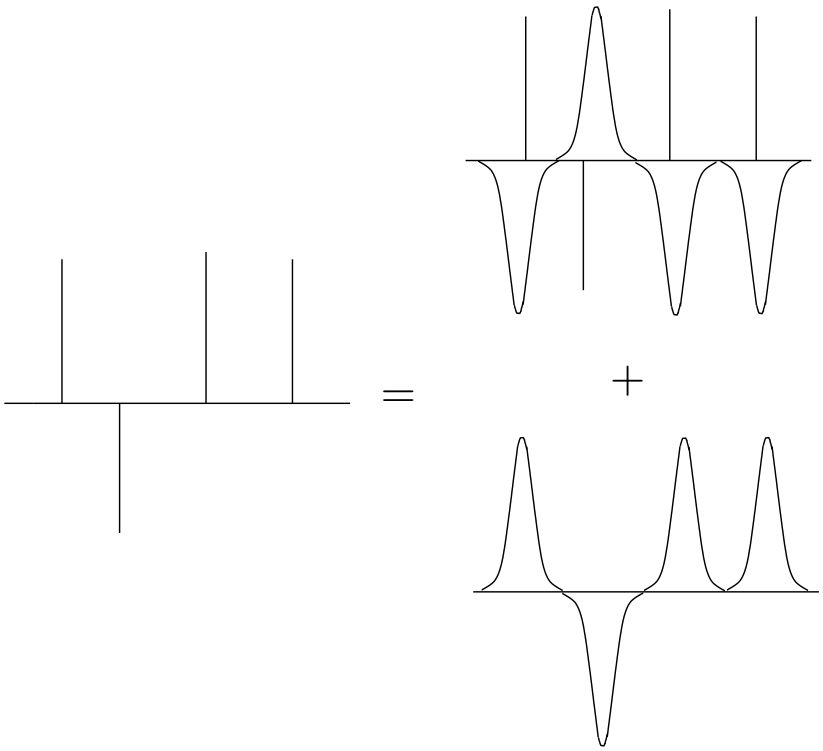

Figure 3.4: Illustration of the Ewald summation methodology: A set of point charges (left) can be considered as a set of screened charges (screened by oppositely charged Gaussians) (right,top) plus the smoothly-varying correction to the screening (Gaussians) (right bottom).

(although it should agree to within a few percent).

In essence the problem is one of a global optimisation and corresponds to the finding minimum potential energy configuration. There are a number of ways in which this can be achieved, with the simplest being the method of "Steepest Descents" (also called the gradient descent method). This, like many optimisation methods, is an iterative method where a point of lower energy is found by the following:

$$\mathbf{x}_{i+1} = \mathbf{x}_i + \lambda \mathbf{s}_i \tag{3.42}$$

where the subscript i denotes iteration number and the optimal step length, λ and the directions to step, $\mathbf{s}_i$ are to be determined. The method of Steepest Descents uses this form, where the minimum of the function f is found by minimising (stepping) along a line from a point, $\mathbf{x}_i$ to a point $\mathbf{x}_{i+1}$ in the direction of $\mathbf{s}_i = -\nabla \mathrm{f}(\mathbf{x}_i)$ and iterating this procedure until either the minimum is reached or the function starts to increase

$$\mathbf{x}_{i+1} = \mathbf{x}_i - \lambda \nabla \mathrm{f}(x_i) \tag{3.43}$$

If the function does start to increase, a new direction is chosen (typically orthogonal

to the local gradient direction) and the procedure continues. This method has severe drawbacks for functions of f that have long narrow valley structures as it may take many iterations to reach convergence. An improvement to this, known as the conjugate gradients method, may be derived in which the search direction is chosen that is both conjugate to the current and all previous search directions. Figure 3.5 shows a diagram of the above methods.

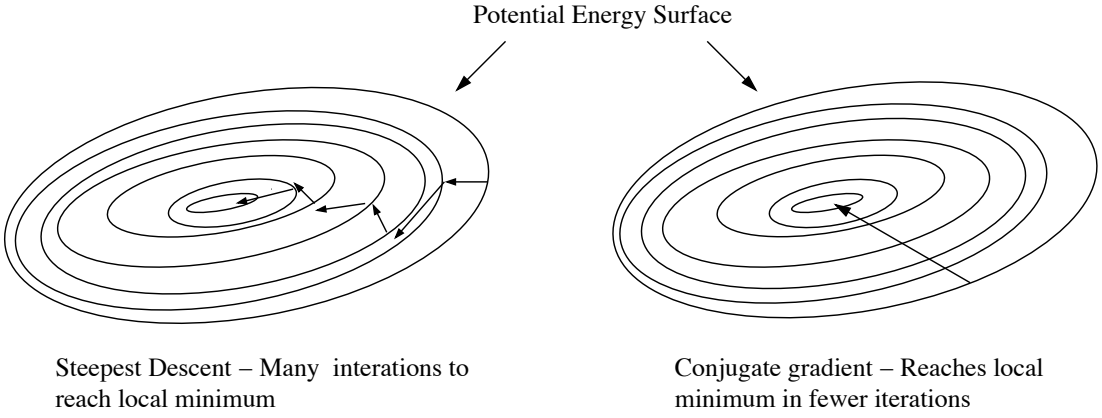

Figure 3.5: Methods of Steepest Descent (left) and Conjugate Gradients (right) used for global optimisation.

3.5.1 The BFGS algorithm

The so-called BFGS algorithm was named after its developers, Broyden,Fletcher,Goldfarb and Shanno [Broyden, 1970; Fletcher, 1970; Goldfarb, 1970; Shanno, 1970] and is a quasi-Newtonian optimisation technique. The theory of quasi-Newton methods is that an approximation to the curvature of a non-linear function can be computed without having to form the Hessian matrix [Gill *et al.*, 2004]. The Hessian matrix, **A** (an NxN matrix of second derivatives of a function) holds the curvature information of a function and is key to finding the minima of that function and has the form for a potential energy surface, E of:

$$\mathbf{A} = \begin{pmatrix} \frac{\partial^2 E}{\partial x_1^2} & \frac{\partial^2 E}{\partial x_1 x_2} & \cdots & \frac{\partial^2 E}{\partial x_1 x_N} \\ \frac{\partial^2 E}{\partial x_2 x_1} & \ddots & & \vdots \\ \vdots & & \ddots & \vdots \\ \frac{\partial^2 E}{\partial x_N x_1} & \cdots & \cdots & \frac{\partial^2 E}{\partial x_N x_N} \end{pmatrix} \tag{3.44}$$

The BFGS algorithm uses an initial guess at an approximate Hessian matrix and what is termed an update matrix to update the Hessian with information accumulated during the minimisation procedure. The basic idea is that around a local minima, the energy surface is assumed to quadratic for very small displacements. Let us take a step s_i from

a position x_i in a search direction p_i. To find this search direction, let us expand the gradient function around the point x_i as a Taylor series

$$\nabla f(x_i + s_i) = \nabla f(x_i) + \mathbf{A}_i s_i + \dots \tag{3.45}$$

The curvature of f can be approximated using first-order information:

$$s_i^T \mathbf{A}_i s_i \approx (\nabla f(x_i + s_i) - \nabla f_i)^T s_i \tag{3.46}$$

At the start of each optimisation iteration there exists an approximate Hessian, $\mathbf{B}_i$ which has the information of the curvature from all previous iterations. If this Hessian is taken to model a quadratic function, then we can find a search direction, p_i that is a stationary point satisfying the Newton direction, and is given by the linear equation:

$$\mathbf{B}_i p_i = -\nabla f(x_i) \tag{3.47}$$

This is equivalent to the method of Steepest Decent if on the first iteration and there exists no prior information available to the Hessian ($\mathbf{B}_0$ is taken as the identity matrix). To compute the new location we use the substitution:

$$s_i = x_{i+1} - x_i \equiv \lambda_i p_i \tag{3.48}$$

and re-arrange equation 3.47 to give

$$x_{i+1} = x_i - \lambda_i \mathbf{H}_i \nabla f(x_i) \tag{3.49}$$

where $\mathbf{H}_i$ is the inverse Hessian and λ a scalar step in that direction (similar to the Steepest Descent method). After the step has been computed, the Hessian (or inverse Hessian) is updated to take into account the new curvature information:

$$\mathbf{B}_{i+1} = \mathbf{B}_i + \mathbf{U}_i \tag{3.50}$$

where $\mathbf{U}_i$ is the update matrix. In order for the updated Hessian to satisfy the quasi-Newton condition we must have:

$$\mathbf{B}_{i+1} s_i = \nabla f(x_{i+1}) - \nabla f(x_i) \tag{3.51}$$

During an optimisation iteration, the only new information obtained about the function f is along only one direction. Thus the updated Hessian only differs from its previous

iteration by a matrix of low rank. Either a one-rank or a rank-two matrix correction is often used:

$$\mathbf{U}_i = auu^T - bvv^T \tag{3.52}$$

where a one-rank correction has the scalar $b = 0$ and u and v are vectors. Using the substitution: $y_k = \nabla f(x_{i+1}) - \nabla f(x_i)$, the BFGS formula can be show to become:

$$\mathbf{B}_{i+1} = \mathbf{B}_i + \frac{\lambda_i \nabla f(x_i) y_k^T}{y_k^T (x_{i+1} - x_i)} + \frac{y_k y_k^T}{y_k^T (x_{i+1} - x_i)} \tag{3.53}$$

Using the above methods a system can be relaxed to its lowest energy state by iteratively minimising the system energy (or enthalpy) with respect to the atoms' positions (which results in a zero force). It can be also done with respect to the system strain, resulting in zero pressure and stress in the system.

3.6 *Ab initio* computer simulation

3.6.1 The many-body problem

The many-body problem comes from considering a system with many atoms and electrons. As will be discussed, the electronic interactions pose an impossible problem for computer simulations due the enormous computational storage costs of the many-body wavefunction.

3.6.1.1 The Born-Oppenheimer approximation

The Born-Oppenheimer Approximation [Born and Oppenheimer, 1927] is a powerful approximation, as it separates the electronic and nuclear motion allowing the many-body wavefunction to be described as a product of the electronic and nuclear wavefunctions. The idea is that as electrons are much lighter and move much faster than the ions in the system, they are said to instantaneously respond to any ionic motion. The ions are treated to obey Newton's Laws for classical particles and the time-independant Schrödinger equation is used to describe the electronic wavefunction.

3.6.1.2 The Schrödinger equation

The goal of most approaches lies in solving the electronic time-independant Schrödinger equation:

$$\left\{-\frac{1}{2}\nabla^2+\hat{V}_{ext}(\mathbf{R}_I)+\hat{V}_e(\mathbf{r}_i)\right\}\Psi(\mathbf{r}_i,\ldots,\mathbf{r}_n)=E\Psi(\mathbf{r}_i,\ldots,\mathbf{r}_n) \tag{3.54}$$

where atomic units have been used ($\hbar = m_e = e = 1$), the first term is the kinetic energy operator, the second term is the Coulomb potential of the nuclei:

$$\hat{V}_{ext}(\mathbf{R}_I,\mathbf{r}_i)=-\sum_i\sum_I\frac{Z_i}{|\mathbf{R}_I-\mathbf{r}_i|} \tag{3.55}$$

and the third term is the electron-electron Coulomb interaction:

$$\hat{V}_e(\mathbf{r}_i)=\frac{1}{2}\sum_i\sum_{j\neq i}\frac{1}{|\mathbf{r}_j-\mathbf{r}_i|} \tag{3.56}$$

and $\Psi(\mathbf{r}_i,\ldots,\mathbf{r}_n)$ is the 3N-dimensional wavefunction. The electron-electron term in the Schrödinger equation makes numerical solutions for more than a few electrons impossible due to the huge storage cost of the wavefunctions. Therefore approximations have to be constructed to make this problem possible. Early work used a mean-field approximation which replaced the many-body wavefunction with a sum of many one-particle wavefunctions. This is called the Hartree approximation, and replaced the electron-electron interaction with:

$$\hat{V}_H=\int d\mathbf{r}'\frac{n(\mathbf{r}')}{|\mathbf{r}'-\mathbf{r}|} \tag{3.57}$$

where $n(\mathbf{r})$ is an average electron density. However, because the solution to the one-particle wavefunction depends on the electron density, which in turn, depends on the wavefunction, then solving this requires a self-consistent approach. A much better approximation was developed called the Hartree-Fock approximation which overcomes some of the failings of the Hartree approximation (e.g. the violation of the Pauli Exclusion principle for the wavefunction). This approximation replaces the many-body wavefunction with a Slater determinant that guarantees the antisymmetric requirement under exchange of electrons. This approximation gives reasonable values for the total energies of atoms but still has shortcomings - the difference between the actual energy and the energy calculated using this approximation was called the correlation energy.

3.6.2 Density Functional Theory

Density Functional Theory (DFT) is a quantum mechanical theory designed to investigate electronic structure. It was developed 1960's based on the work by Walter Kohn and P. Hohenberg [Hohenberg and Kohn, 1964]. The principle behind the theory is that

the total ground state energy of a system can be written in terms of a unique functional[1] of the electron ground-state density, $n(\mathbf{r})$, where the electron density is:

$$n(\mathbf{r}) = \int \dots \int d\mathbf{r}_2 \dots \mathbf{r}_n |\Psi(\mathbf{r}_i|^2 \tag{3.58}$$

The ansatz for the total energy is:

$$E[n(\mathbf{r})] = F[n(\mathbf{r})] + \int \hat{V}_{ext}(\mathbf{r}) n(\mathbf{r}) d\mathbf{r} \tag{3.59}$$

where the functional $F[n(\mathbf{r})]$ is unknown and therefore researchers re-wrote it as a sum of the kinetic and Hartree contributions plus a contribution that has both the exchange and the correlation effects. Knowledge of this last term would enable an exact solution to the many-body Schrödinger equation for the ground state energy. The terms above are calculated in DFT using the method introduced by Kohn and Sham [1965] in which the system of interacting electrons is replaced with a system of non-interacting electrons with the same electron density. The kinetic energy of a non-interacting system is:

$$E_K[n(\mathbf{r})] = -\frac{1}{2} \int \phi_n^*(\mathbf{r}) \nabla^2 \phi_i(\mathbf{r}) d\mathbf{r} \tag{3.60}$$

Thus the Schrödinger equation to solve [Refson, 2006] is:

$$\left\{ -\frac{1}{2}\nabla^2 + \hat{V}_{ext}(\mathbf{R}_I) + \hat{V}_H(\mathbf{r}) + \hat{V}_{XC}(\mathbf{r}) \right\} \phi_n(\mathbf{r}) = E_n \phi_n(\mathbf{r}) \tag{3.61}$$

where $\phi_n(\mathbf{r})$ are the one-particle Kohn-Sham wavefunctions (often called the Kohn-Sham orbitals) and the exchange-correlation potential is given by a functional derivative:

$$\hat{V}_{XC}(\mathbf{r}) = \frac{\delta E_{XC}[n(\mathbf{r})]}{\delta n} \tag{3.62}$$

and contains all the unknown information about $F[n(\mathbf{r})]$ including the difference between the kinetic energies of the interacting and non-interacting systems. Once again, this functional is unknown. It was hoped that the exchange and correlation effects would give a relatively small contribution and a reasonable approximation should yield good results. This is true for some systems such as metals, but for strongly correlated systems the exchange and correlation effects are large, and other methods, such as GW [Hedin, 1965] are required to find the ground state energy.

[1] A functional is a function of a function

3.6.2.1 Local Density Approximation

The Local Density Approximation (LDA) makes the approximation:

$$E_{XC}[n(\mathbf{r})] = \int d\mathbf{r}\, n(\mathbf{r})\, \varepsilon_{XC}(n(\mathbf{r})) \tag{3.63}$$

where $\varepsilon_{XC}(n(\mathbf{r}))$ is the exchange-correlation density at a point $\mathbf{r}$ as a function of the density. In a homogeneous electron gas this is known exactly (from Monte-Carlo simulations). Considering atoms, LDA tends to over-bind resulting in bond-lengths about 1% smaller than experiment. However, LDA remains a good approximation for many systems and gives a reasonable description of chemical bonding, surfaces and defects. The success of LDA can be partially attributed to it obeying the sum rule. That is, the amount of positive charge surrounding each electron in the homogeneous electron gas (due to electrostatic repulsion) is equal to exactly one electron. Many prospective improvements to LDA failed due to not obeying the sum rule.

3.6.2.2 Generalised Gradient Approximation

The Generalised Gradient Approximation (GGA) is a more sophisticated approximation for the exchange-correlation functional and is used for systems in which the electron density rapidly changes. The gradient of the electron density is taken into account in GGA. The GGA proposed by Wang and Perdew [1991] obeys the sum rule and is often used for calculations. GGA is successful in describing the binding and dissociation energies in many systems although does tend to under-bind.

3.6.2.3 Reciprocal space and the Brillouin zone

Reciprocal space is a useful concept in DFT and simplifies many computational problems. In crystallography the reciprocal lattice is defined as:

$$e^{\mathbf{k}\cdot\mathbf{r}} = 1 \tag{3.64}$$

for a wavevector, $\mathbf{k}$ and a position vector $\mathbf{r}$.

The position vectors in reciprocal space are given by the following formulae:

$$\begin{aligned} \mathbf{a}^* &= 2\pi \frac{\mathbf{b}\times\mathbf{c}}{\mathbf{a}\cdot(\mathbf{b}\times\mathbf{c})} \\ \mathbf{b}^* &= 2\pi \frac{\mathbf{c}\times\mathbf{a}}{\mathbf{a}\cdot(\mathbf{b}\times\mathbf{c})} \\ \mathbf{c}^* &= 2\pi \frac{\mathbf{a}\times\mathbf{b}}{\mathbf{a}\cdot(\mathbf{b}\times\mathbf{c})} \end{aligned} \tag{3.65}$$

where **a**, **b**, **c** are the real space lattice vectors, and $\mathbf{a} \cdot (\mathbf{b} \times \mathbf{c})$ is the volume of the unit cell. Points on the reciprocal lattice are defined as:

$$\mathbf{G} = h\mathbf{a}^* + k\mathbf{b}^* + l\mathbf{c}^* \tag{3.66}$$

where h,k,l are integers.

The Brillouin zone is the location in reciprocal space that has the smallest volume and the complete space group symmetry of the crystal. The first Brillouin zone therefore, is the primitive cell of the reciprocal lattice and is the dual of the Wigner-Seitz cell in real space. There are several points that are of special interest - and correspond to areas of symmetry. An important point is the center of the Brilloiun zone and is called the Gamma point (Γ point). In a calculation, the charge density is calculated using a sum over a discrete set of wavevectors (called k-points) in the Brillouin zone. Many k-points may be required to accurately sample the Brillouin zone however these can be reduced using the symmetry in the cell [Monkhorst and Pack, 1976]. As the energy of the system is dependent on the number of k-points chosen, care must be taken to ensure that the system is properly converged with respect to k-point density. Unfortunately, a large number of k-points also imposes a large computational burden, although there are effective methods to distribute the computational load when using large-scale supercomputers.

3.6.2.4 Basis sets

For computer simulations, it is convenient to express the wavefunction in terms of a basis set:

$$\phi(\mathbf{r}) = \sum_{\alpha} c_\alpha \phi_\alpha(\mathbf{r}) \tag{3.67}$$

where the complex coefficients c_α determine the outcome of all operations on the set of basis functions ϕ_α. This means that a computer can be used to store the coefficients and to solve an eigenvalue equation of the form:

$$Hc_\alpha = Ec_\alpha. \tag{3.68}$$

Popular basis sets include plane-waves, Gaussians, Slater-type orbitals and Muffin-tin orbitals. However plane waves are widely used in solid state calculations due to their inherent periodic properties [Refson, 2006] .

3.6.2.5 Plane waves

Many systems of interest are crystalline and therefore the external potential acting on the electrons is periodic. Bloch's theorem states that solutions to the Schrödinger equation for a periodic system can be written as

$$\Psi_k(\mathbf{r}) = e^{i\mathbf{k}\cdot\mathbf{r}} u_k(\mathbf{r}) \tag{3.69}$$

where k is an arbitrary wavevector within the first Brillouin zone and $u_k(\mathbf{r})$ is a periodic function of r with the same periodicity as the potential.

A Fourier series can be used to expand $u_k(\mathbf{r})$:

$$u_k(\mathbf{r}) = \sum_{\mathbf{G}} c_{\mathbf{k},\mathbf{G}} e^{i\mathbf{G}\cdot\mathbf{r}} \tag{3.70}$$

where $c_{\mathbf{k},\mathbf{G}}$ are the complex Fourier coefficients, and the sum is over all reciprocal lattice vectors. A plane-wave basis set of the form:

$$\phi_\alpha(\mathbf{r}) = e^{i\mathbf{G}\cdot\mathbf{r}} \tag{3.71}$$

is a natural basis for expressing the wavefunction of a periodic system. Therefore, the wavefunction (equation 3.69) can be written:

$$\Psi_k(\mathbf{r}) = \sum_{\mathbf{G}} c_{\mathbf{k},\mathbf{G}} e^{i(\mathbf{k}+\mathbf{G})\cdot\mathbf{r}} \tag{3.72}$$

From the variational principle in quantum mechanics we see that only an upper bound on the true ground state energy can be obtained when using a finite basis set size. Increasing the basis set size will always lead to a monotonic decrease in the computed energy however, the smallest number of plane-waves needed to accurately represent the system needs to be determined. This can be done using a parameter called the cut-off energy:

$$E_c = \frac{1}{2}|\mathbf{k}+\mathbf{G}|^2 \tag{3.73}$$

Of course, as the cut-off energy is variational then the computed ground state energy will always decrease with increasing cut-off. It is therefore important to use as many plane waves as sufficient to converge the ground state energy to a required tolerance.

3.6.3 Convergence of the ground-state energy

When performing DFT calculations one has to ensure that the parameters chosen ensure that the simulation is converged to the computed ground state energy. This means that the value of the ground state energy is, to some reasonable tolerance, unchanged with increased number of k-points and increased cut-off energy. One has to remember that the computation time increases with number of plane waves and with the number of k-points. Figures 3.6 and 3.7 give an example of a converged aluminium system of 108 atoms. In figure 3.6 the cut-off energy is converged (to meV precision) at 300 eV. Converging the cut-off energy is not sufficient for convergence; a series of different k-point sampling tests are also required, chosen to be performed at the value of converged cut-off energy. As can be seen from figure 3.7 the k-point density has converged (to meV precision) at a value of 0.005 $\AA^{-1}$ which corresponded to a Monkhorst pack grid of $15 \times 15 \times 15$ points in the Brillouin zone. As can be seen from the graph, the k-point sampling is a non-variational parameter and therefore the energy can fluctuate both down and up during convergence testing.

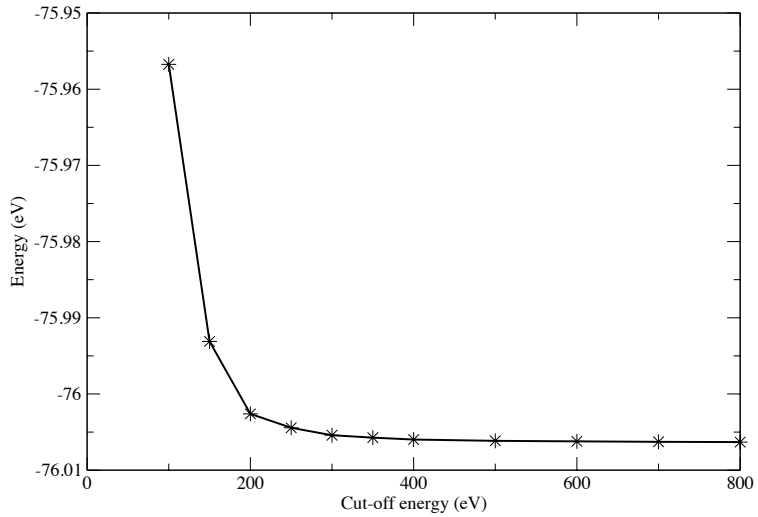

Figure 3.6: Cut-off energy convergence for a K-point spacing of 0.014 $\AA^{-1}$.

3.7 Structural analysis

3.7.1 The radial distribution function

The radial distribution function, g(r), of a system is a measure of the local structure of the system. g(r) can also be obtained from x-ray and neutron diffraction experiments

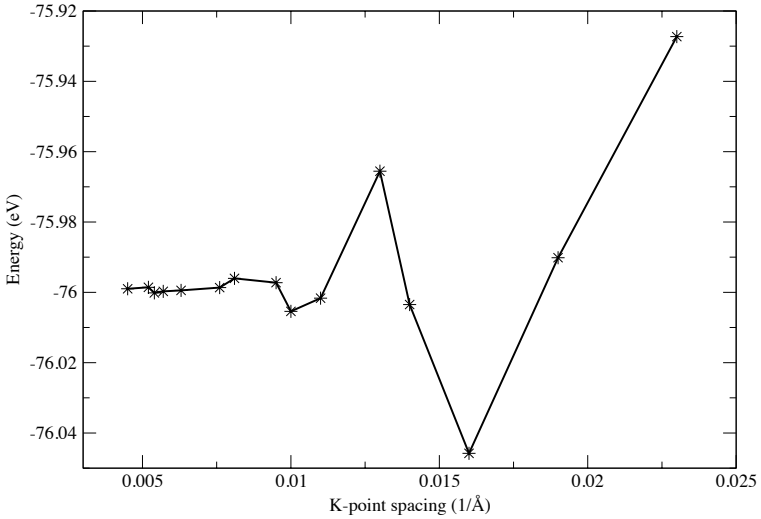

Figure 3.7: K-point density convergence for a cut-off of 300 eV.

and therefore gives a metric of evaluating the performance of computer simulations. g(r) is simple to compute in molecular dynamics simulations since the positions of each atom are available as a function of time. g(r) is defined by:

$$g(\mathbf{r}) = \frac{1}{\rho N} \left\langle \sum_{i}^{N} \sum_{j \neq i}^{N} \delta[\mathbf{r} - \mathbf{r}_{ij}] \right\rangle \tag{3.74}$$

where N is total number of atoms, ρ is the number density ($\rho = N/V$), and the angular brackets represent a time average. For homogeneous materials, the structural arrangement is independent of the orientation and only depends on distance between atoms. Also, the double sum in equation 3.74 only contains $\frac{1}{2}N(N-1)$ unique terms. Applying normalisation, and by integrating over all pairs of atoms we reduce to:

$$\int g(r) d\mathbf{r} = \frac{1}{\rho} N(N-1) \tag{3.75}$$

The above equation says that there are $N-1$ other atoms in the system surrounding a particular atom. This might appear obvious, but it is useful for the basis of a probabilistic interpretation of g(r). This says the probability of a finding an atom in a spherical shell of radius r, and thickness Δr , centered on a particular atom is:

$$\frac{1}{N-1} \rho g(r) V(r, \Delta r) \tag{3.76}$$

where $V(r, \Delta r)$ is the volume of the shell. For small separations, one atom has a large

influence on the surrounding atoms and $g(r) \approx 0$, whereas for large separations, one atom has little influence on the position of another and $g(r) = 1$. To compute g(r) in simulations we consider equation 3.74 with a small shell thickness Δr:

$$\sum_{\Delta r} g(r)V(r,\Delta r) = \frac{2}{\rho N}\sum_{\Delta r}\left\langle \sum_{i}^{N}\sum_{j\neq i}^{N}\delta[r - r_{ij}]\Delta r \right\rangle \tag{3.77}$$

where the double sum actually represents a counting operation, and equals the number of atoms in the spherical shell of thickness Δr. Therefore we can write the following expression for g(r):

$$g(r) = \frac{2 < N(r,\Delta r) >}{N\rho V(r,\Delta r)} \tag{3.78}$$

If we consider a simulation with M time steps, then the time-average of g(r) can be written explicitly:

$$g(r) = 2\sum_{i=1}^{M} N_i(r,\Delta r)\frac{1}{MN\rho V(r,\Delta r)} \tag{3.79}$$

where N_i is the counting operation result at time t_i in the simulation. The value of Δr is important as too small a value would yield a small population sample and therefore statistically unreliable results, whereas too large a value could miss important details of the structure.

3.8 Simulating Shock waves in condensed matter

Using the methods outlined above, equilibrium properties of the material under investigation are easily computed. However, a shock wave is a dynamic and non-equilibrium event and therefore further techniques are required before a successful shock wave simulation can be performed. The generation of a shock wave can be performed by a number of different methods already discussed in 1.3.2.1. In this work, the concept known as a momentum mirror was used and will therefore be described in detail.

3.8.1 The momentum mirror

A concept known as the momentum mirror was developed by Holian [1988] to generate a shock wave in computer simulations. This momentum mirror is (usually) located at $z = 0$ plane and acts as a perfect reflector for incoming atoms. It can also be located at $x = 0$ or $y = 0$ planes to investigate directional compressibility. The momentum mirror used in this work was invoked after the second step of the velocity-verlet integration

algorithm; any atom that had a $z < 0$ position had the sign of its velocity and position switched. This resulted in the atom effectively "bouncing" off a perfectly reflecting surface. Thus, on subsequent MD steps, any plane of atoms that had been reflected by the mirror would be closer to the next plane of atoms which would feel a strong force away from the mirror. This force creates the shock wave and propagates away from the momentum mirror ($z = 0$ plane). Figure 3.8 shows a schematic of a system with a momentum mirror.

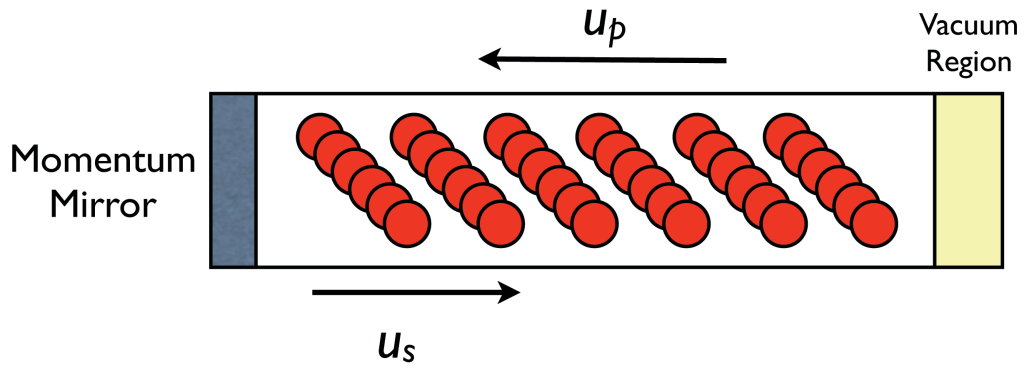

Figure 3.8: A schematic of a 3D system with a momentum mirror. u_p is the piston velocity towards the momentum mirror and u_s is the subsequent shock velocity away from the mirror. Periodic boundary conditions are used throughout, therefore a vacuum region is employed to avoid particle interactions through the momentum mirror.

The momentum mirror is essentially an infinitely massive piston that impacts with the system to start a shock wave. Holian [1988] outlined the problems associated with the momentum mirror approach; material near the mirror can react in a way different from normal impact shock wave experiments; as the momentum mirror approach is asymmetric, atoms near the mirror are trapped against a cold piston and heat up. Thus for calculating averages, the first few planes of atoms near the mirror should be disregarded. One other problem is that the free surface at the end of the system has to be properly equilibrated to prevent a shock propagating into the simulation cell due to relaxation.

3.8.2 Shock wave generation

The shock wave in the systems was generated by giving all the atoms in the system a velocity towards the $z = 0$ plane and the momentum mirror. The desired strength of the shock wave was determined by the velocity that the atoms impacted the momentum mirror. By Galilean invariance, this velocity is the piston velocity, u_p by analogy with the experimental work discussed in section 1.3. Molecular Dynamics using the micro-

canonical ensemble were performed until the shock wave reached the back plane of atoms. At this time, the whole system is in the shocked state and is under maximum compression.

3.8.3 Temperature effects

Holian and Straub [1979] studied the effect of temperature on shock wave simulations. They proposed that a system must have a temperature in order for the shock wave to become a steady wave. At $T_0 = 0K$ the system is said to be unable to sustain a steady shock wave through the simulation cell. The reason for this is that there is a transverse stress relaxation process that happens behind the shock front, which couples with the shock wave to form a steady wave. Steady waves are essential to allow the Rankine-Hugoniot relations to be obeyed. This coupling is absent in a perfect crystal at zero temperature. We performed a zero temperature shock wave simulation on a perfect crystal of 1000 argon atoms to verify this claim. The shock velocity used was the speed of sound in solid argon ($\approx$ 1000 m/s) and was considered to be a strong shock wave. The results showed that at $T_0 = 0K$, the system behaved as if one-dimensional, where each atom only moved in the z-direction and had no movement in either x or y directions. This caused a self-similar wave to propagate in the system and a shock wave was never established. Figure 3.9 shows snapshots of the system initially and at maximum compression. Figure 3.10 shows two velocity profiles for a plane of atoms located spatially at 10 Å and 18 Å from the momentum mirror in the z-direction. The profiles show that the atoms were oscillating in the z-direction as the planes of atoms collided and rebounded. This oscillatory motion destroyed the onset of a steady shock wave and was seen to have decayed with increasing distance from the momentum mirror. By 18 Å the oscillations had decayed to almost zero.The profiles showed no evidence of a steady shock wave, and therefore we can conclude that shock waves in three-dimensional systems must have a temperature greater than zero in order to facilitate the creation of a steady wave. A system with temperature would allow for transverse stress relaxation behind the shock front. It is worth noting that this effect is likely due to the simulation using a perfect crystal, and experiments would not see this effect. Also if an imperfect crystal was used, where the atoms where not located on their lattice points, then a shock wave should still be capable of forming.

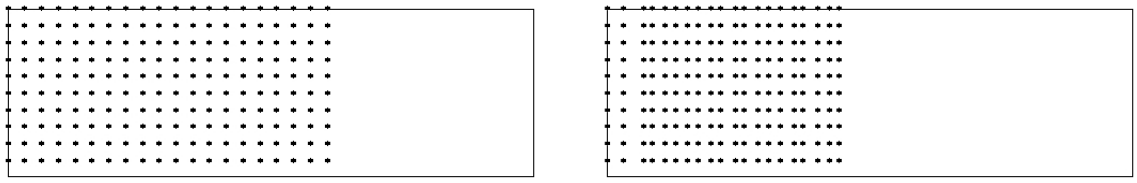

Figure 3.9: Snapshots of a T=0 shock wave simulation, presented as a 2D slice of a 3D simulation. Atomic positions (illustrated with black dots) are inside a rectangular simulation cell. System is moving towards the left where a momentum mirror is located at the far left boundary. Left: Initial system configuration. Right: System at maximum compression does not show the effect of a shock wave. Therefore a system at $T_0 = 0$K is unable to sustain a steady shock wave (see text for detailed discussion and also figure 3.10).

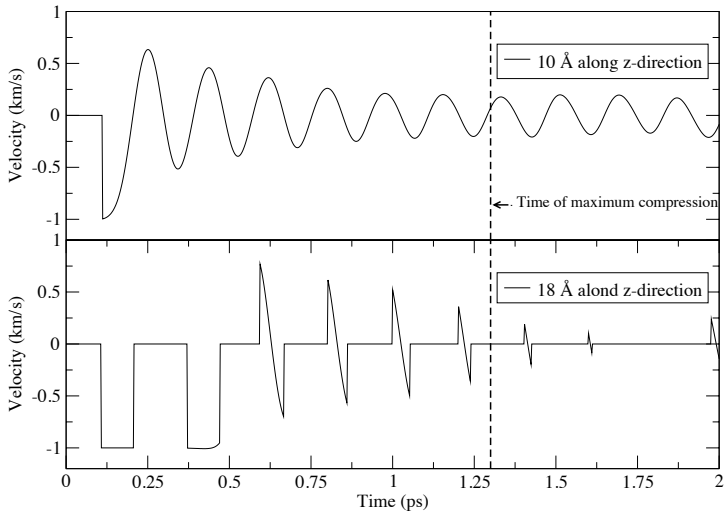

Figure 3.10: $T_0 = 0$K shock wave velocity profiles. Profiles are located at 10 Å and 18 Å from the momentum mirror along the z-direction. The system does not show a shock wave velocity profile and therefore the system was unable to sustain a steady shock wave (see text for discussion).

3.9 Summary

Computer simulation has matured into a valuable tool for scientists. The choice of whether to use interatomic potentials or to use the far more accurate, but far more computational costly, *ab initio* approaches (for which DFT is but one choice) depends on the particular problem at hand, but they are so far not suitable for shock wave simulation due to the large number of atoms required for a steady-state wave to propagate in the system. The methods for computing temperatures, pressures and other properties remain the same however, and the choice of ensemble and the choice of thermostat and/or barostat once again depends on the problem to be solved. For shock waves, it is evident (see also chapter one) that many atoms are required to capture the effects caused by the propagating discontinuity, and thus interatomic potentials are the best choice for computing the energies and forces, and using the NVE ensemble. An approach adopted by the majority of researchers in the field and also the approach adopted for the work in this thesis. Temperature plays an important role in simulation shock wave generation, without it there can be no steady-state wave as there would be no transverse directional stress relaxation mechanisms. This of course, only applies to perfect crystals and is therefore unlikely, if not impossible to observe experimentally.

References

Hans C. Andersen. Molecular dynamics simulations at constant pressure and/or temperature. *J. Chem. Phys.*, 72(4):2384–2393, 1980.

H. J. C. Berendsen, J. P. M. Postma, W. F. van Gunsteren, A. DiNola, and J. R. Haak. Molecular dynamics with coupling to an external bath. *J. Chem. Phys.*, 81(8):3684–3690, 1984.

M. Born and R. Oppenheimer. Quantum theory of molecules. *Ann. Phys.-Berlin*, 84: 0457–0484, 1927.

C. G. Broyden. Convergence of single-rank quasi-Newton methods. *Math. Comput.*, 24:365, 1970.

M. S. Daw and M. I. Baskes. Semiempirical, quantum-mechanical calculation of hydrogen embrittlement in metals. *Phys. Rev. Lett.*, 50:1285–1288, 1983.

P. M. Derlet, R. Hoier, R. Holmestad, K. Marthinsen, and N. Ryum. The embedded-atom model applied to vacancy formation in bulk aluminium and lithium. *J. Phys.-Condes. Matter*, 11:3663–3677, 1999.

S. Erkoc. Empirical many-body potential energy functions used in computer simulations of condensed matter properties. *Phys. Rep.-Rev. Sec. Phys. Lett.*, 278:80–105, 1997.

R. Fletcher. A new approach to variable metric algorithms. *Comput. J.*, 13:317, 1970.

D. Frenkel and B Smit. *Understanding Molecular Simulation,*From Algorithms to Applications. Academic Press, 2002. ISBN 0-12-267351-4.

E.P. Gill, W. Murray, and M. H. Wright. *Practical Optimization*. Elsevier Academic Press, 2004. ISBN 0-12-283952-8.

D. Goldfarb. A family of variable-metric methods derived by variational means. *Math. Comput.*, 24:23, 1970.

L. Greengard and V. Rokhlin. On the evaluation of electrostatic interactions in molecular modeling. *Chem Scr*, 29A:139–144, 1989.

J.M. Haile. *Molecular Dynamics Simulation, Elementary Methods*. Wiley-Interscience, John Wiley and Sons inc., 1997. ISBN 0-471-18439-X.

Lars Hedin. New method for calculating the one-particle Greenś function with application to the electron-gas problem. *Phys. Rev.*, 139(3A):A796–A823, Aug 1965.

P. Hohenberg and W. Kohn. Inhomogeneous electron gas. *Phys. Rev. B*, 136:B864, 1964.

B. L. Holian. Modeling shock-wave deformation via molecular-dynamics. *Phys. Rev. A.*, 37:2562–2568, 1988.

B. L. Holian and G. K. Straub. Molecular-dynamics of shock-waves in 3-dimensional solids - transition from nonsteady to steady waves in perfect crystals and implications for the Rankine-Hugoniot conditions. *Phys. Rev. Lett.*, 43:1598–1600, 1979.

William G. Hoover. Canonical dynamics: Equilibrium phase-space distributions. *Phys. Rev. A*, 31(3):1695–1697, 1985.

William G. Hoover. Constant-pressure equations of motion. *Phys. Rev. A*, 34(3):2499–2500, 1986.

R. A. Johnson. Empirical potentials and their use in calculation of energies of point-defects in metals. *J. Phys. F: Met. Phys.*, 3:295–321, 1973.

R. A. Johnson. Analytic nearest-neighbor model for fcc metals. *Phys. Rev. B*, 37: 3924–3931, 1988.

J. E. Jones. On the determination of molecular fields. I. From the variation of the viscosity of a gas with temperature. *Proc. R. Soc. A.*, 106(738):441–462, 1924a. ISSN 09501207.

J. E. Jones. On the determination of molecular fields. II. From the equation of state of a gas. *Proc. R. Soc. A*, 106(738):463–477, 1924b. ISSN 09501207.

H. Kimizuka, H. Kaburaki, and Y. Kogure. Molecular-dynamics study of the high-temperature elasticity of quartz above the alpha-beta phase transition. *Phys. Rev. B*, 67, 2003.

W. Kohn and L. J. Sham. Self-consistent equations including exchange and correlation effects. *Phys. Rev.*, 140:1133, 1965.

G. J. Kramer, N. P. Farragher, B. W. H. van Beest, and R. A. van Santen. Interatomic force-fields for silicas, aluminophosphates, and zeolites - derivation based on ab initio calculations. *Phys. Rev. B*, 43:5068–5080, 1991.

Glenn J. Martyna, Michael L. Klein, and Mark Tuckerman. Nosé-Hoover chains: The canonical ensemble via continuous dynamics. *J. Chem. Phys.*, 97(4):2635–2643, 1992.

J. Mei and J. W. Davenport. Free-energy calculations and the melting-point of Al. *Phys. Rev. B*, 46:21–25, 1992.

H. J. Monkhorst and J. D. Pack. Special points for Brillouin-zone integrations. *Phys. Rev. B*, 13:5188–5192, 1976.

V. V. Murashov and I. M. Svishchev. Quartz family of silica polymorphs: Comparative simulation study of quartz, moganite, and orthorhombic silica, and their phase transformations. *Phys. Rev. B*, 57:5639–5646, 1998.

J. K. Norskov and N. D. Lang. Effective-medium theory of chemical-binding - application to chemisorption. *Phys. Rev. B*, 21:2131–2136, 1980.

Shuichi Nose. A unified formulation of the constant temperature molecular dynamics methods. *J. Chem. Phys.*, 81(1):511–519, 1984.

K. Refson. First-Principles Simulation. CCP5/MCA Summer School, 2006.

D. F. Shanno. Conditioning of quasi-Newton methods for function minimization. *Math. Comput.*, 24:647, 1970.

M. J. Stott and E. Zaremba. Quasiatoms - an approach to atoms in nonuniform electronic systems. *Phys. Rev. B*, 22:1564–1583, 1980.

W. C. Swope, H. C. Andersen, P. H. Berens, and K. R. Wilson. A computer-simulation method for the calculation of equilibrium-constants for the formation of physical clusters of molecules - application to small water clusters. *J. Chem. Phys.*, 76:637–649, 1982.

S. Tsuneyuki, M. Tsukada, H. Aoki, and Y. Matsui. First-principles interatomic potential of silica applied to molecular dynamics. *Phys. Rev. Lett.*, 61(7):869–872, Aug 1988. doi: 10.1103/PhysRevLett.61.869.

L. Verlet. Computer experiments on classical fluids .I. thermodynamical properties of Lennard-Jones molecules. *Phys. Rev.*, 159:98, 1967.

Yue Wang and John P. Perdew. Spin scaling of the electron-gas correlation energy in the high-density limit. *Phys. Rev. B*, 43(11):8911–8916, 1991.

Chapter 4

Shock wave simulations in Lennard-Jones systems

4.1 Introduction

This chapter is concerned with simulations using the well known Lennard-Jones (LJ) empirical pair potential. Lennard-Jonesium systems are the ideal starting point to develop the methodology for shock wave simulations because of the computational simplicity of the LJ (12,6) pair potential. The LJ (12,6) pair potential has been shown to give a good representation for the equilibrium properties of the noble gas argon and therefore this material was used for the shock wave simulations discussed in this chapter. The chapter is organised as follows; first, a brief description of argon will be given followed by the results of equilibrium simulations on argon. The results of shock wave simulations in Lennard-Jonesium systems will then be discussed.

4.1.1 Argon

Argon was the first noble gas to be discovered and is located in Group 8 of the Periodic Table of elements. It is a colourless, odourless gas contributing less then 1% (by volume) of the Earth's atmosphere. It was discovered in 1894 by Lord Rayleigh and Sir William Ramsay after an experiment that removed oxygen and nitrogen from a sample of air [Rayleigh and Ramsay, 1894]. Today, argon is collected as a bi-product of the creation of liquid oxygen and liquid nitrogen. Argon is chemically inert, making it useful for applications such as fire extinguishers and shielding air-sensitive materials. However, the most common use is in traditional incandescent light bulbs where it protects the element from oxidisation. Solid argon has a Face-Centred Cubic (FCC) structure, space group Fm3m (space group number 225). Argon melts at 83.85 K and boils at 87.15 K. Figure 4.1 shows a unit cell structure for argon.

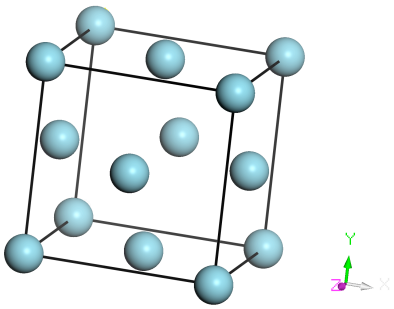

Figure 4.1: Conventional unit cell of crystalline argon

4.2 Equilibrium simulations

The usual parameters for the Lennard-Jones potential were used: $\sigma = 3.405$ Å, $\varepsilon = 120$ K and a cut-off distance, $r_{cut} = 2.5\sigma$. Therefore, the smallest simulation cell that could be used for argon is $4 \times 4 \times 4$ unit cells (256 atoms) due to the Minimum Image Convention (see 3.3.3) and this was used to calculate the equilibrium properties.

4.2.1 Geometry optimisation

The simulation cell was equilibrated using the geometry optimisation technique discussed in section 3.5. Stress and Force were converged to MPa and meV/Å, respectively. Figure 4.2 shows the convergence of the stress parameter. The lattice parameter was calculated to be $a = 5.305$ Å. This compares well with the experimental value of Henshaw [1958]: $a = 5.256$ Å.

4.3 Static compression

A series of hydrostatic compression calculations were performed and the PV graph can be seen in figure 4.3. It can be seen from the figure that the maximum compression achievable is tending towards 0.40 times the initial volume. Theoretical work on gases [Zel'dovich and Raizer, 2002] has shown that the maximum compression achievable for an ideal gas is 0.25. The discrepancy between the calculated value and the theoretical one is likely due the system being in the solid phase and also the unphysical r^{-12} part of the LJ potential.

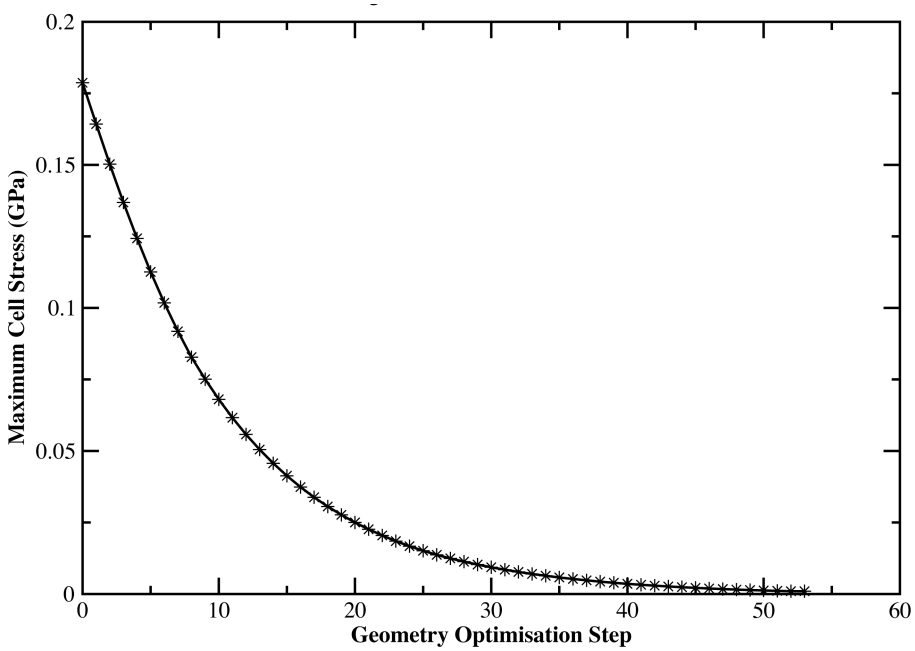

Figure 4.2: Simulation cell stress convergence of argon using the Lennard-Jones (12,6) potential

4.4 Shock wave simulations

As discussed above, argon has been extensively studied and its equilibrium properties well described by the LJ (12,6) potential. It is expected however that a shock wave will result in the energy and forces being calculated from the unphysical r^{-12} region of the potential. This is accepted, as the main purpose of this particular study was to verify that the shock wave simulations were being performed as accurately and error free as possible. The ease of computing the LJ energies and forces allows focus on the mechanics of the shock wave generation itself.

The shock wave simulations were performed on 1000, 2000 and 4000 atom systems. All systems were created from the equilibrium simulation cells and further equilibrated to ensure stress and forces were zero. A vacuum gap of 10.00 Å was added to the z-direction, which was parallel to lattice parameter “c” to ensure that atoms at either end of the simulation cell were separated by a distance greater than the cut-off distance of the LJ potential and so did not interact with each other. Periodic boundary conditions were still applied in the x and y-directions. The speed of sound in solid argon was taken as 1.05 km/s [Dobbs and Jones, 1957]. Figure 4.4 shows a snapshot at 1.5 ps of one of the shock wave calculations, with a shock wave propagating at 2 km/s from left to right. The shock front is clearly identified and the shocked argon has no structure behind the shock front, indicating an amorphous state. Figure 4.5 shows a typical velocity profile for this shock wave at simulation times between 1 and 4 ps. The particle velocity was

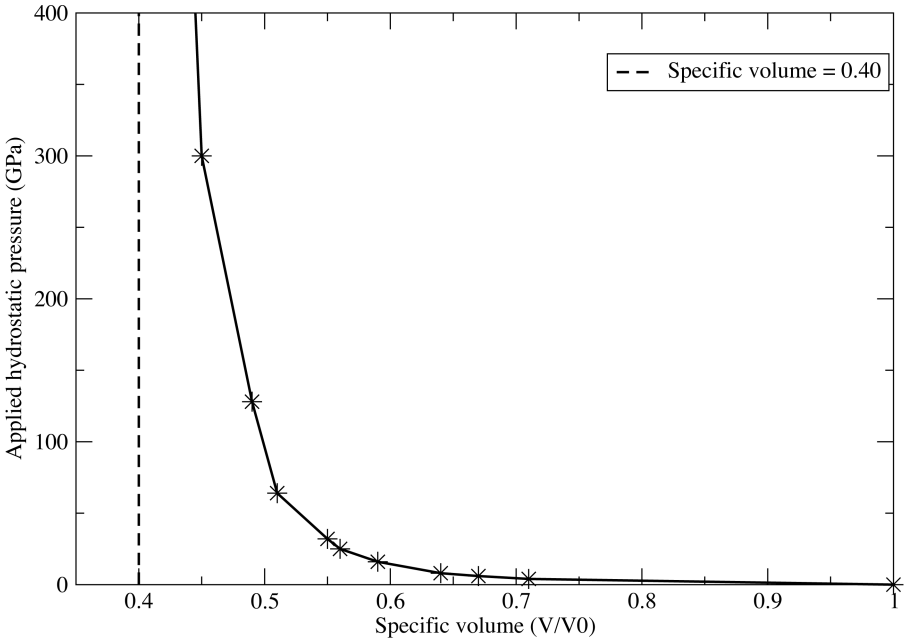

Figure 4.3: Hydrostatic compression of argon using the Lennard-Jones (12,6) potential. The compression is approaching a maximum compression of 0.4 times the initial volume, as marked on the graph by a dotted line.

obtained by dividing the system length (along z) into 1 Å segments, and the atoms' z-component of velocity in each bin averaged per atom. This spatial averaging then gave a snapshot of the atoms velocity along the simulation cell, and the shock front was the discontinuity in the velocity profile. The shock front clearly separates the shocked and equilibrium states in the material and was of a constant amplitude and velocity as can be seen in Figure 4.5.

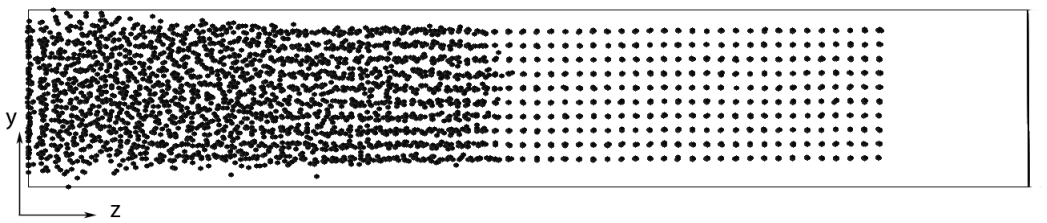

Figure 4.4: Snapshot of a shock wave in a system of 4000 argon atoms presented as a 2D slice (taken at $x = 0$) of a 3D simulation. Momentum mirror located at $z = 0$ plane, u_p = 2.0 km/s, $t = 1.5$ ps. The shock wave is propagating from left to right, leaving an amorphous state behind the shock front.

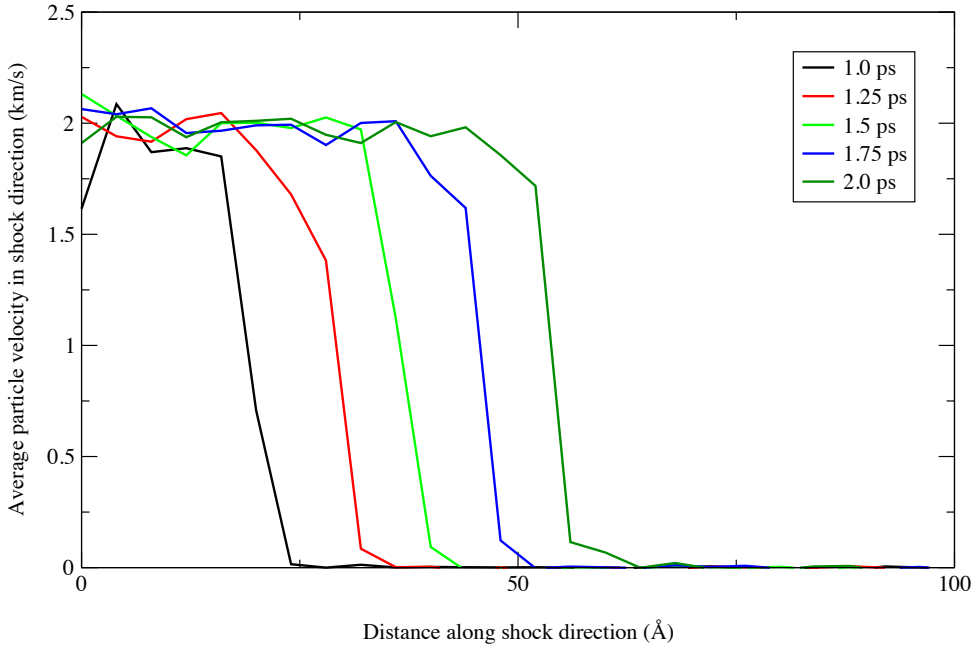

Figure 4.5: Average particle velocity profiles for a shock wave in a system of 4000 argon atoms. u_p = 2.0 km/s. The shock front (the discontinuity in the particle velocity profile) is constant in amplitude and velocity.

4.4.1 Relationship between the shock and the piston velocities

The relationship between the piston velocity and the shock velocity is also called a Hugoniot and is shown in figure 4.6 for the calculations here (atomistic data), and experimental data of Dick *et al.* [1970]. The dotted line is a linear fit to these data up to 10 GPa, using the formula:

$$u_s = au_p + c_0 \tag{4.1}$$

where a is the fitting variable and c_0 is the speed of sound in the material at zero pressure [Kanel *et al.*, 2004]. It can be seen that there is also a good agreement of the atomistic data with the linear Hugoniot equation (equation 1.1) with $a = 1.0$, up to 10 GPa. After this point the plot is in poor agreement with the linear Hugoniot equation, however the fit agrees with an intercept ($u_s = 0$) with the bulk sound speed calculated from adiabatic compressibility data [Dobbs and Jones, 1957].

The data points for piston velocity, u_p, were taken as the velocity given to the system towards the momentum mirror. The Rankine-Hugoniot relations were not used to compute the particle velocities at this time. The data points for the shock velocity, u_s,

were computed from the time the first plane of atoms hit the momentum mirror to the time the shock wave reached the free surface, i.e. to a point just after the maximum compression of the system.

The experimental data of Dick *et al.* [1970] is also plotted in figure 4.6. They used an explosive lens system to generate a shock wave in their samples of solid argon which were created by immersing the sample container of argon into a liquid nitrogen bath. Their shock velocities were calculated using the Rankine-Hugoniot relations. They used the method of least-squares fit to their data, and decided it was best fitted by using two regions: $2.00 \leq u_s \leq 5.79$ km/s and $5.79 \leq u_s \leq 8.50$ km/s. Good agreement of the atomistic data with the experimental data can be seen up to about $u_s = 5.0$ km/s. After this the experimental and the atomistic simulation data diverge. In figure 4.6 we see that there are differences in the computed Hugoniots for the three systems, but between 2000 and 4000 atoms these differences are very small. It is likely that finite-size effects were evident for the smallest system, but by 4000 atoms the effects had converged. Systems larger than 4000 atoms are likely to yield very similar results, and systems smaller than 4000 atoms may suffer from finite size effects.

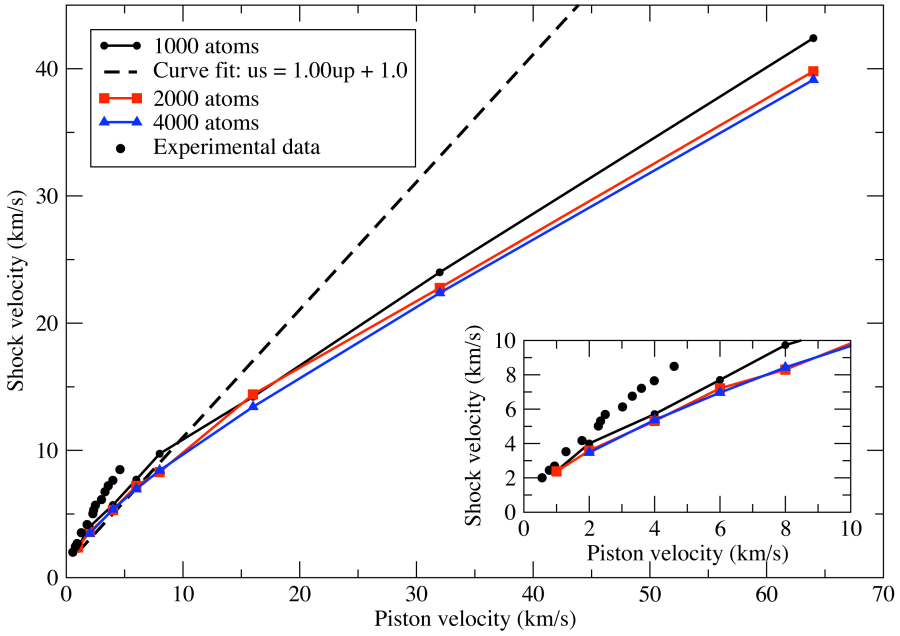

Figure 4.6: Piston and shock velocity relationship for three different system sizes and experimental shock wave data of Dick *et al.* [1970].

4.4.2 The Hugoniot

Figure 4.7 shows the calculated Hugoniot for the 4000 argon atom system along with static compression data from section 4.3 and experimental data of Dick *et al.* [1970]. The hydrostatic compression data more faithfully follows the experimental data than

the shock compression data. A reason for the difference may be attributed to the way the pressure was calculated for the shock compression data. The maximum of the σ_{zz} component of the stress tensor was chosen as the shock pressure, which may not be the same as for the hydrostatic or experimental pressures. However at the maximum pressure the system was under maximum compression before the shock wave exited the back plane. Comparing the maximum stress tensor (σ_{zz}) pressure and volume with the static compression data, it can be seen that the final volume is smaller for the static compression at the same (but hydrostatic) pressure. This could be due to the atoms re-arranging to minimise the stresses on the system. This is not possible for shock compression simulations as there is little time for the atoms to react as the shock front passes through the system. Therefore the location of the shock Hugoniot is expected to lie above the static compression Hugoniot on a PV plot. The failure to agree with the experimental data is more than likely due to the shock wave simulation probing the unphysical r^{-12} region of the LJ potential, whereas the static compression does not readily probe this region and therefore its data are in good agreement. This indicates that the potential is too rigid for shock compression simulations and that the that the r^{-12} term may be too strong.

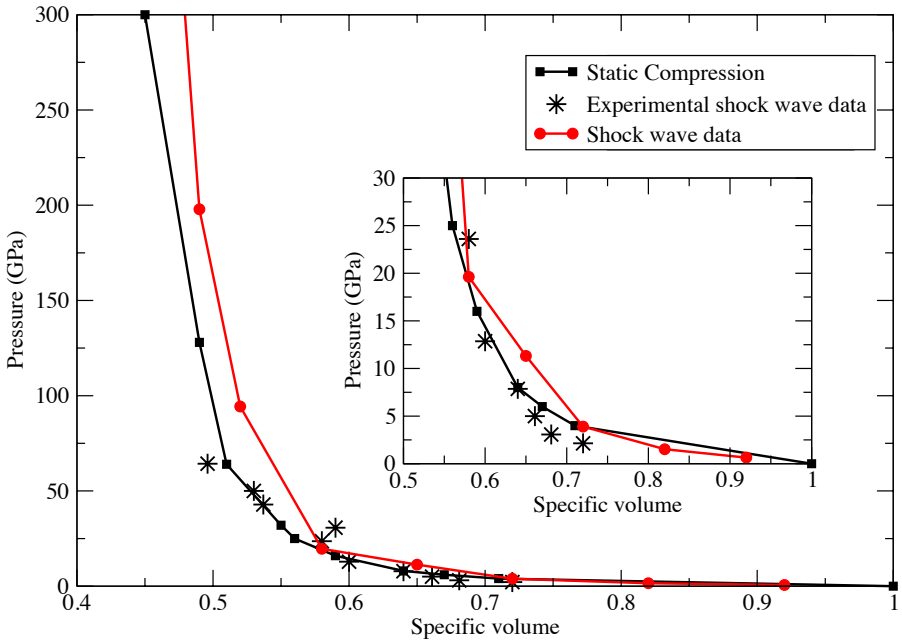

Figure 4.7: Hugoniot of argon using the Lennard-Jones (12,6) potential along with experimental shock wave data of Dick *et al.* [1970]. Also plotted is the hydrostatic compression data.

4.5 Summary

This chapter has described the use of the LJ potential in the simulation of shock waves through Lennard-Jones systems (argon was used as the LJ potential yields good agreement to its equilibrium properties). The purpose of these calculations was to verify the methodology for shock wave simulation (this methodology is outlined in Appendix C). The work in this chapter has allowed for a methodology to be built for shock wave simulations. The results obtained showed that the LJ potential under-estimated the final volume for shock wave simulations, possibly due to the unphysical r^{-12} part of the potential. As this functional form was chosen as a numerical convenience for equilibrium calculations, it is deemed unsuitable for the non-equilibrium situation of shock compression.

References

R. D. Dick, R. H. Warnes, and J. Skalyo. Shock compression of solid argon. *J. Chem. Phys.*, 53:1648, 1970.

E. R. Dobbs and G. O. Jones. Theory and properties of solid argon. *Rep. Prog. Phys.*, 20:516–564, 1957.

D. G. Henshaw. Atomic distribution in liquid and solid neon and solid argon by neutron diffraction. *Phys. Rev.*, 111(6):1470–1475, 1958.

G.I. Kanel, S.V. Razorenov, and V.A. Fortov. *Shock-Wave Phenomena and the Properties of Condensed Matter*. Springer-Verlag New York Publishing, 2004. ISBN 0-387-20572-1.

Lord Rayleigh and William Ramsay. Argon, a new constituent of the atmosphere. *Proc. R. Soc. (London)*, 57:265–287, 1894.

Ya. B. Zel'dovich and Yu.P. Raizer. *Physics of Shock Waves and High-Temperature Hydrodynamic Phenomena*. Dover Publications, New York, 2002. ISBN 0-486-42002-7.

Chapter 5

Simulations of quartz

5.1 Introduction

Silicon dioxide, SiO_2, is most commonly known as quartz and it is the second most abundant mineral in the Earth's crust. It is thought to comprise a large part of the Earth's mantle where it is at high-pressures of up to 136 GPa and high-temperatures up to 1200 K. At room temperature, quartz is naturally found in the α-quartz phase (also known as low-quartz) and has many uses from clock parts to an impedance match standard for VISAR experiments [Hicks *et al.*, 2005]. Quartz has a number of high-pressure and high-temperature polymorphs, with β-quartz (high-quartz), coesite, and stishovite being the most well-known. Figure 5.1 shows an experimentally determined phase diagram of quartz [Akhavan, 2005]. The low-pressure polymorphs of quartz all have each silicon atom surrounded by 4 oxygen atoms in the crystal lattice and therefore each silicon is said to have a coordination number of 4. Stishovite however, has a coordination number of 6 and has a very different arrangement of atoms in its crystal lattice to all the other quartz polymorphs [Sinclair and Ringwood, 1978]. It is also known that quartz becomes amorphous at high-pressures, between 25 and 35 GPa at 300K using static experiments, such as diamond anvil cells [Hemley *et al.*, 1988]. However, there is still some debate about the mechanisms that underlie such phase changes and whether the dynamic nature of shock compression could allow the formation of one of the high-pressure polymorphs of quartz, such as stishovite. This chapter investigates shock compression of quartz to determine whether such a high-pressure phase change is possible and the underlying re-structuring mechanisms at the atomic level.

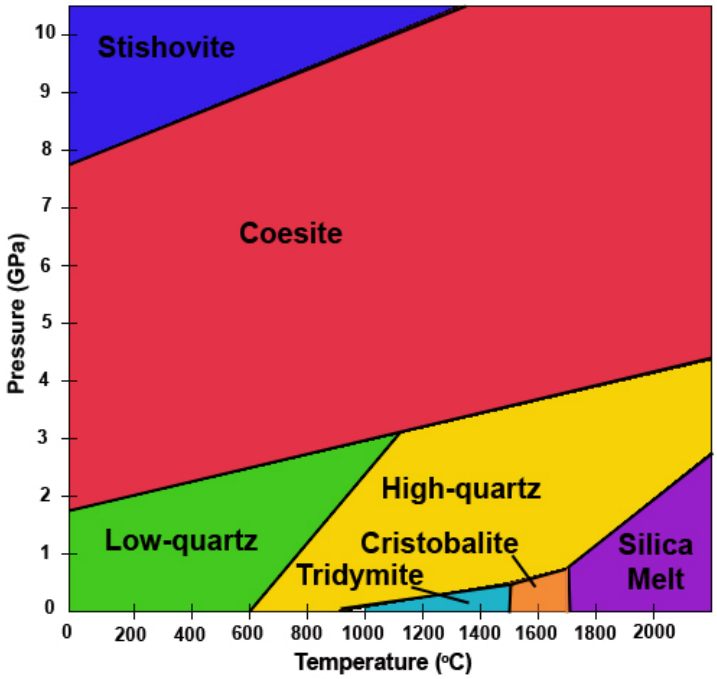

Figure 5.1: The phase diagram of quartz [Akhavan, 2005].

5.2 Equilibrium calculations

Figure 5.2 shows diagrams of the unit cell of α-quartz. The 9 atoms in the unit cell have a silicon to oxygen coordination number of 4, with the oxygens surrounding the silicon forming a tetrahedral shape.

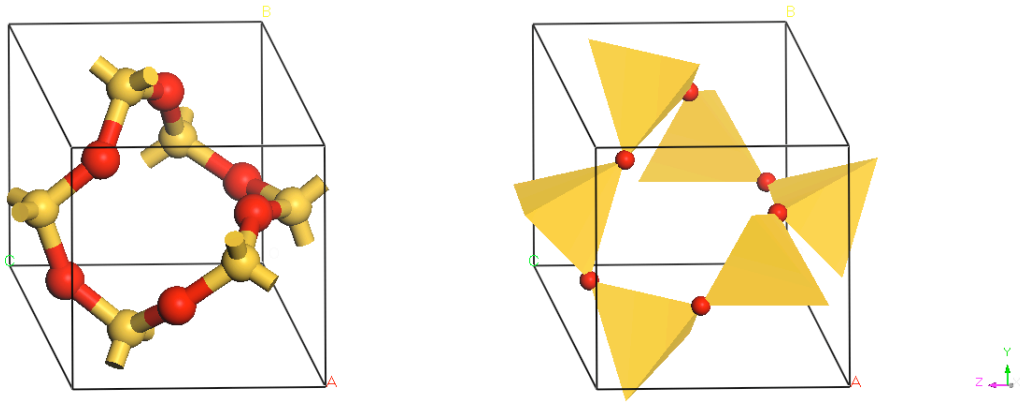

Figure 5.2: Unit cell of α-quartz, containing 9 atoms. Silicon is 4-fold coordinated with oxygen in a tetrahedral shape.

The BKS potential [Kramer *et al.*, 1991] was used with cut-off radii of 6.0 Å for both the silicon-oxygen bonds and oxygen-oxygen bonds, respectively. Therefore the smallest system that could be simulated was 243 atoms ($3 \times 3 \times 3$ unit cells). Figure 5.3 shows the force and stress convergence of a 243 atom system of α-quartz during a geometry optimisation.

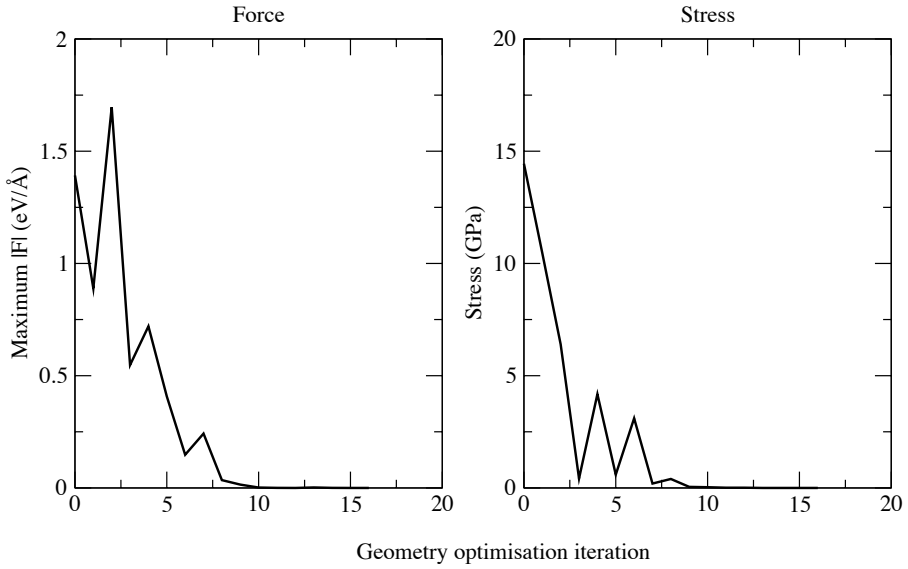

Figure 5.3: Geometry optimisation of α-quartz. Force (left) and stress (right) have been reduced to 1 meV/Å and 1 MPa, respectively.

The calculated lattice parameters of the optimised structure are shown along with DFT calculations[1] using the LDA and GGA functionals and experimental data of Gualtieri [2000] in table 5.1. The BKS potential tends to under-bind by about 2.5%. The under-binding and over-binding of the GGA and LDA functionals, respectively, is also evident.

Table 5.1: Lattice parameters calculated for quartz using the BKS potential and DFT with LDA and GGA functionals.

	a (Å)	**b** (Å)	**c** (Å)	α	β	γ
BKS	5.040	5.040	5.340	90.00	90.00	120.00
LDA	4.901	4.901	5.405	90.00	90.00	120.00
GGA	5.033	5.033	5.512	90.00	90.00	120.00
EXP	4.9158	4.9158	5.4091	90.00	90.00	120.00

[1]Performed by the Author using CASTEP [Segall *et al.*, 2002] with library pseudo-potentials, a cut-off of 600 eV and a k-point density of 0.04 $Å^{-1}$.

5.2.1 Effect of cut-off distance on the lattice parameters

The silicon-oxygen cut-off was investigated to determine the optimal value to use. Figure 5.4 shows the convergence of lattice parameters with cut-off distances. A cut-off of 6.0 Å was chosen as the parameters were changing only by mÅ.

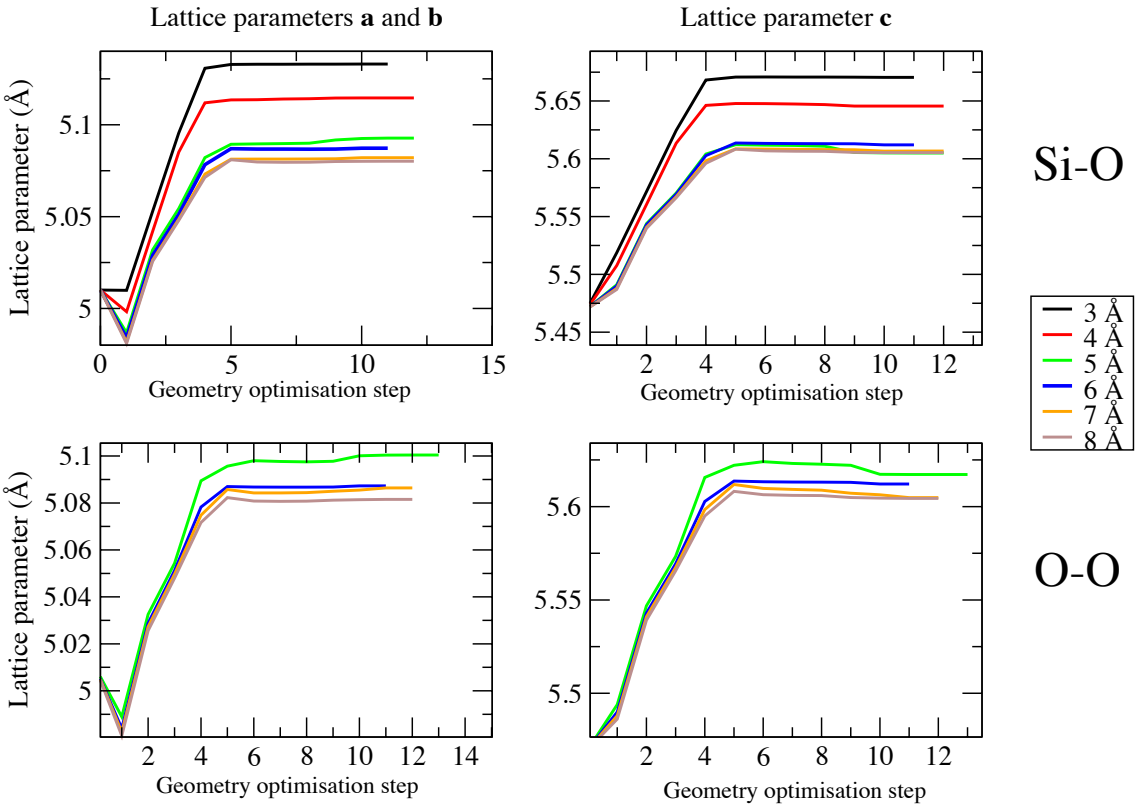

Figure 5.4: Variation of the calculated lattice parameters with different pair-potential cut-off distances. At the chosen cut-off of 6 Å, the lattice parameters are changing by mÅ.

5.2.2 Structure of geometry-optimised α-quartz

After the geometry optimisation it was found that the final structure of BKS potential optimised α-quartz was β-quartz. This was expected as the authors of the BKS potential also found this phase at zero temperature and pressure [Kramer *et al.*, 1991]. These two phases of quartz, α-quartz, and its high-temperature polymorph, β-quartz have similar structures [Bragg and Gibbs, 1925] as can be seen in figure 5.5. However, β-quartz has a slightly lower density and the distances to the second nearest oxygen neighbours of silicon are equal (whereas in α-quartz these distances are different).

These differences are highlighted in Table 5.2 that shows experimentally determined values [Akhavan, 2005]. The radial distribution function, g(r) for α-quartz and β-quartz can be seen in figure 5.6. It is clear that β-quartz retains more structure at longer distances, whereas α-quartz has lost its long-range ordering. The main peaks in the g(r) plot occur at 1.62 Å, 2.64 Å and 3.16 Å. These are the Si-O, O-O and Si-Si bond lengths, respectively for the SiO_2 tetrahedron. These compare well with experimental values of Si-O = 1.61 Å and O-O = 2.63 Å [Mozzi and Warren, 1969].

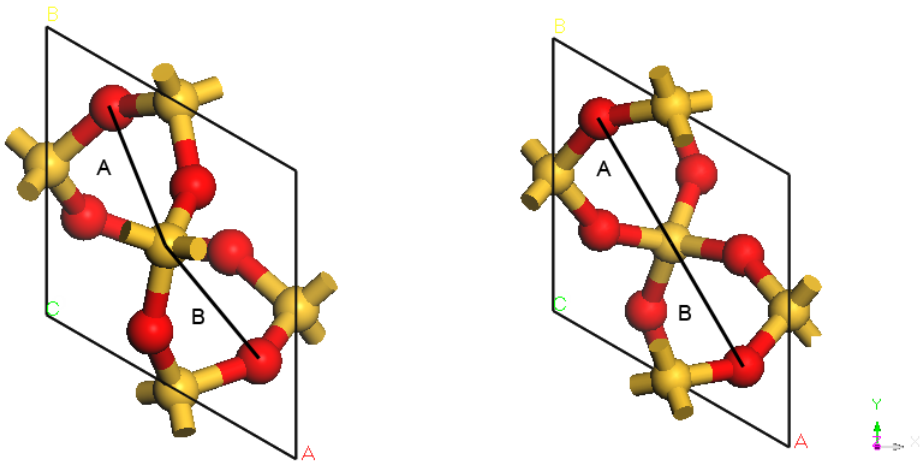

Figure 5.5: Comparison between the unit cells of α-quartz (left) and β-quartz (right). In α-quartz, $A \neq B$, whereas in β-quartz, $A = B$.

Table 5.2: Differences between the α and the β phases of quartz.

	α-quartz	β-quartz
Symmetry	Hexagonal (P3221)	Hexagonal (P6222)
Volume	113.00	118.11
Density	2.650	2.533

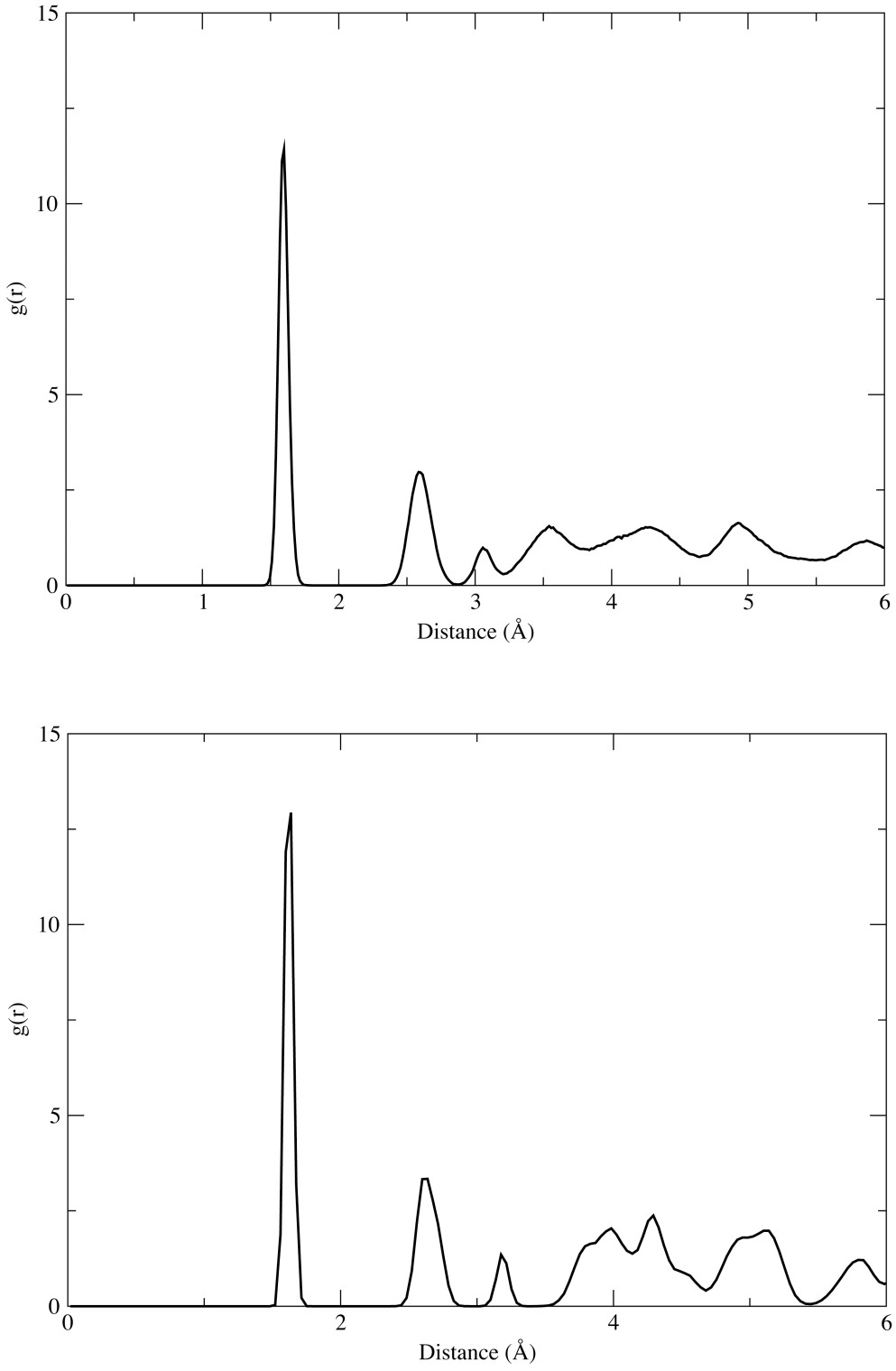

Figure 5.6: Comparison between the radial distribution functions of α-quartz (top) and β-quartz (bottom). See text for discussion.

5.2.3 Hydrostatic compression at T=0K

A series of hydrostatic compression simulations were performed on the geometry-optimised 243 atom system of quartz using the BKS potential. The initial structure was that of β-quartz as shown in figure 5.7. The simulations were performed as a series of geometry optimisations at different pressures, and therefore the compressions were performed at zero kelvin. The results of the hydrostatic compression simulations can be seen in figure 5.8. At 6 GPa the system underwent a phase transformation from β-quartz to α-quartz. The system then remained at α-quartz up to very high-pressures. Figure 5.9 shows the c/a ratio of the lattice parameters for the initial β-quartz system over the phase transformation region. It can be seen that at the transformation boundary, 6 GPa, the c/a ratio shows a discontinuity indicating a sudden structural change. To determine what order of phase transformation had taken place, the energy-volume curve was constructed seen in figure 5.10. This curve shows the total energy of the system (enthalpy minus pressure-volume term) against the system volume. The curve is continuous and therefore the transformation from α-quartz to β-quartz is a second-order phase transformation. Figure 5.11 shows the structure of the quartz system at 8 GPa alongside the structure of bulk α-quartz and it can be seen they are very similar in structure. Symmetry analysis performed on the quartz system at 6 GPa found that it had a P3221 space-group symmetry which is the same as α-quartz.

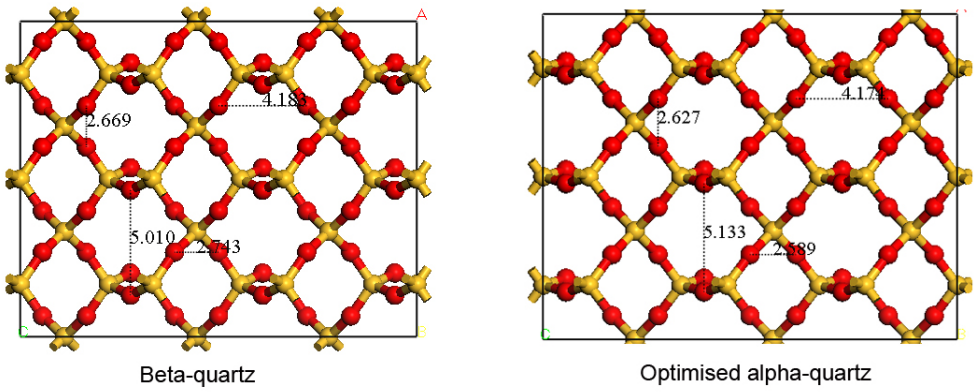

Figure 5.7: Left: Structure of bulk β-quartz. Right: Structure of α-quartz post geometry optimisation at zero pressure. The two structures both have P6222 space group symmetry, indicating the optimised structure is that of β-quartz.

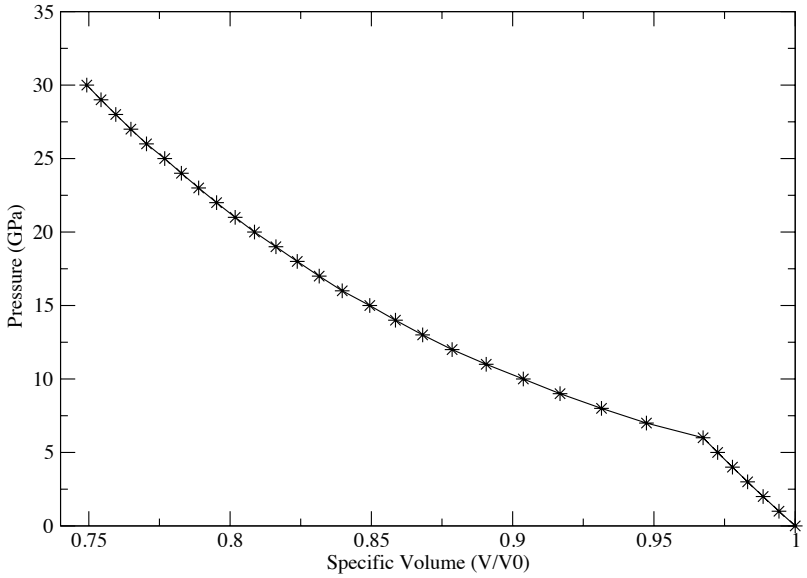

Figure 5.8: Static compression of quartz using the BKS potential. At 0 GPa up to 6GPa the structure remains β-quartz, then at 6 GPa the structure changes to α-quartz.

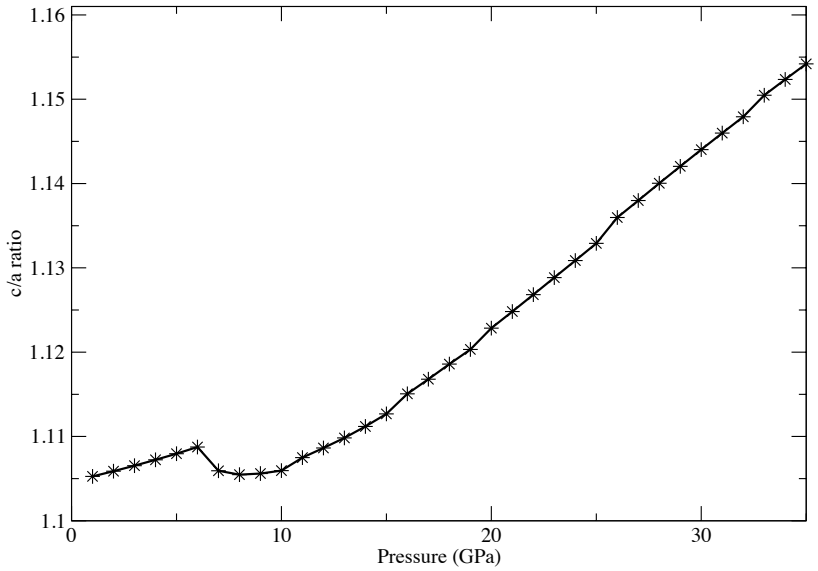

Figure 5.9: c/a ratio of the lattice parameters over a pressure range 0 to 37 GPa using the BKS potential. The discontinuity at 6 GPa corresponds to the sudden transformation of β-quartz to α-quartz.

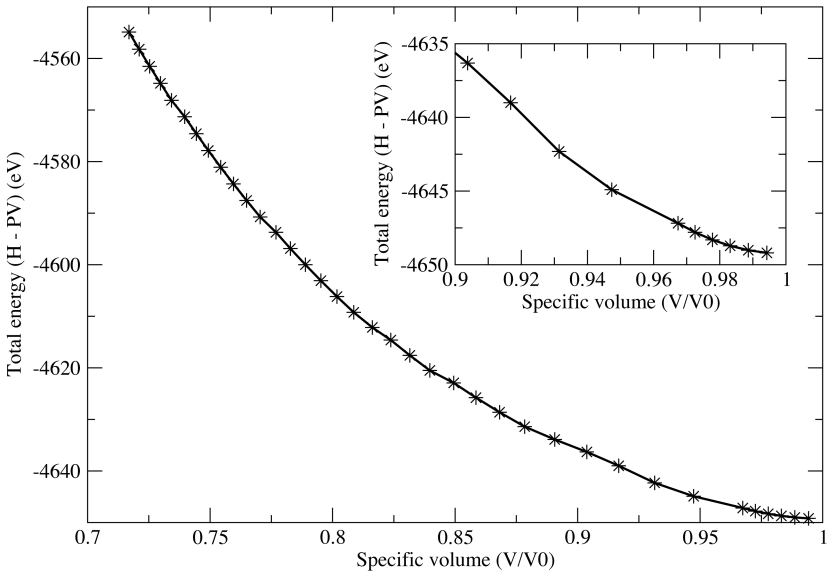

Figure 5.10: Static compression of quartz. Inset: The transition region from β-quartz to α-quartz. The energy-volume plot indicates a second-order phase transition occurs as the curve is smooth and continuous and so there are no discontinuities in its derivative.

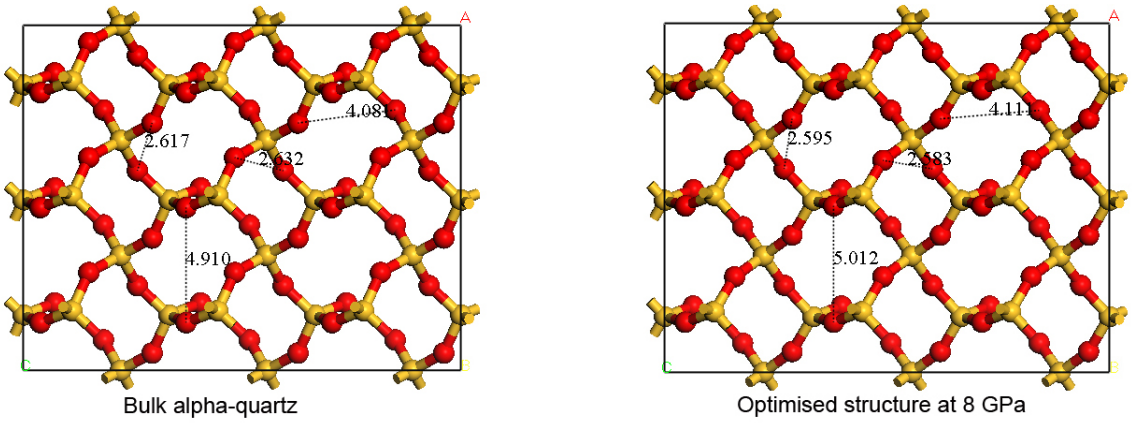

Figure 5.11: Left: Structure of bulk α-quartz. Right: Structure of the quartz system after geometry optimisation at 8 GPa. The two structures both have P3221 space group symmetry, indicating the structure is that of α-quartz.

5.2.4 Structure of high-pressure quartz

It is thought that α-quartz transforms to coesite between 2 and 3 GPa (at room temperature) and to stishovite between 8 and 10 GPa under shock loading. Recovered samples of stishovite have been found in meteorite craters in Arizona [Chao *et al.*, 1962]. Figure 5.12 shows the structure of stishovite (left) [Baur and Khan, 1971] and coesite (right) [Araki and Zoltai, 1969]. The density of coesite and stishovite was 2.896 gcm^{-3} and 4.287 gcm^{-3}, respectively [Sinclair and Ringwood, 1978].

Figure 5.13 shows structure of the quartz system after a geometry optimisation using the BKS potential at a hydrostatic compression of 40 GPa. The structure of this system was α-quartz but had a density of 3.823 gcm^{-3}, therefore putting it at a density between coesite and stishovite.

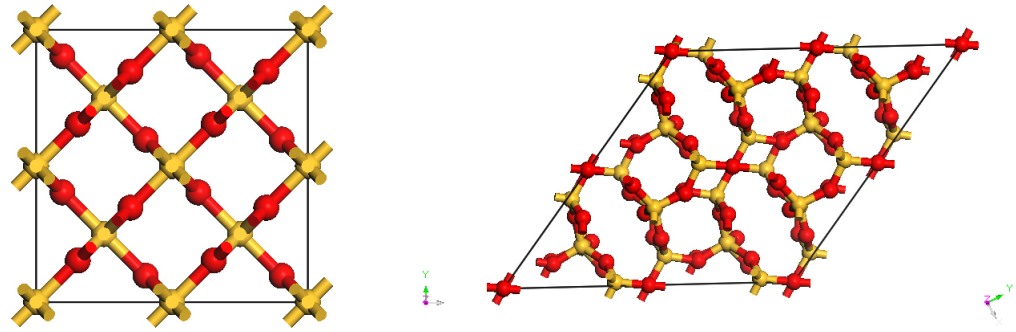

Figure 5.12: Structures of stishovite (left) [Baur and Khan, 1971], with space group symmetry P4/mnm and coesite (right) [Araki and Zoltai, 1969] with space group symmetry C2/c.

The hydrostatic compression was continued until the pair part of the BKS potential failed, that is, when the pressure was large enough to push the interatomic distances passed the point of inflection in the pair potential (zero of the second derivative). This was found to occur at 50 GPa. This had severe consequences for shock wave simulations where it was expected that the pressures would greatly exceed this value for strong shocks. Therefore, the pair part of the BKS potential was extended to allow high-pressure simulations to be performed.

5.2.5 Extending the BKS potential for high-pressure

The nature of shock compression creates very high-temperatures and high-pressures in the system and it is likely that atoms would have sufficient kinetic energy to overcome the pair-potential barrier of the BKS potential. As the BKS potential has the unphysical property of diverging to minus infinity should this happen, this needs to be corrected to allow for shock wave simulations. Several methods have already been employed to correct for this behaviour. Barmes *et al.* [2006] have fitted a 2nd order polynomial to

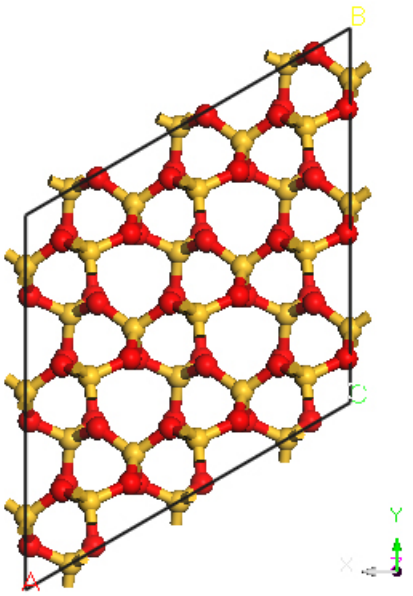

Figure 5.13: Quartz structure at 40 GPa. The structure has the same symmetry as α-quartz but a density between coesite and stishovite.

the (truncated and shifted) BKS pair-part of the potential, and then applied it to shock wave simulations of silica glasses. Guissani and Guillot [1996] have fitted a Lennard-Jones type potential although they were not using BKS, but the TTAM [Tsuneyuki *et al.*, 1988], and were investigating the liquid-vapour state of silica. For this study, a form similar to the latter method was chosen that would give a strong core repulsion at small separations. The pair-part of the BKS potential was replaced at the point of inflection (zero of the second derivative) with:

$$U(r) = \frac{\alpha}{r^2} + \frac{\beta}{r^6} + \gamma \qquad r < r^* \tag{5.1}$$

where α, β and γ are the parameters of the function, analytically derived such that the values of the potential, and the first and second derivatives match those of the potential at the point of inflection, r^*. Table 5.3 shows the fitting parameters calculated and figure 5.14 shows the new form of the potential.

Table 5.3: Numerical values of the fitting parameters used for BKS correction.

	$\alpha(eV\AA^2)$	$\beta(eV\AA^6)$	$\gamma(eV)$
Si-O	24.1700	23.8086	-3.5872
O-O	12.3435	18.9662	-6.9426

The hydrostatic compression simulations were extended to 200 GPa using the BKS potential plus extension. The pressure-volume curve can be seen in figure 5.15.

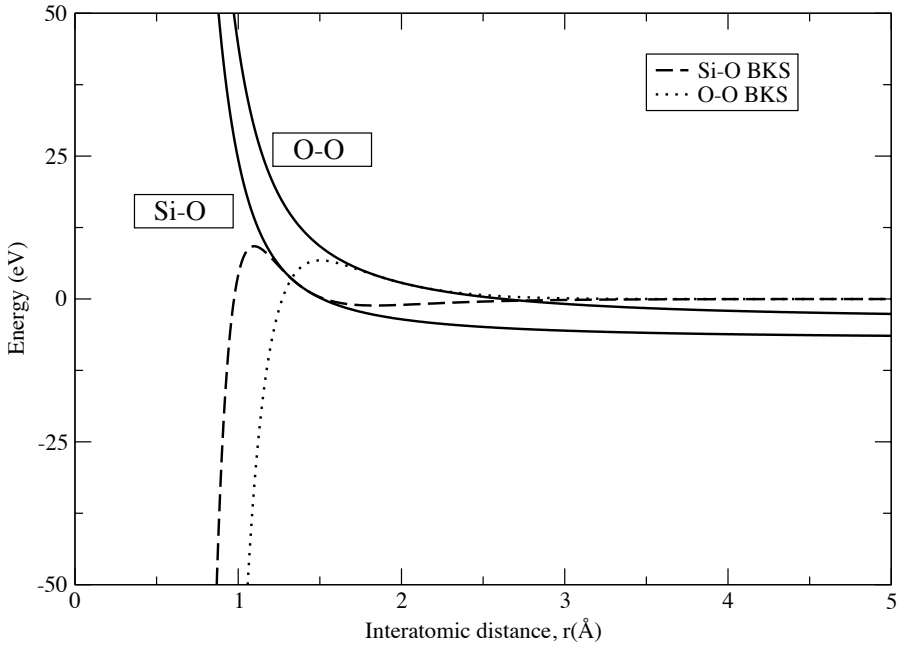

Figure 5.14: Plot of the interatomic potential used in this work. The dashed lines show the unphysical behaviour of the original BKS potential at small interatomic distances.

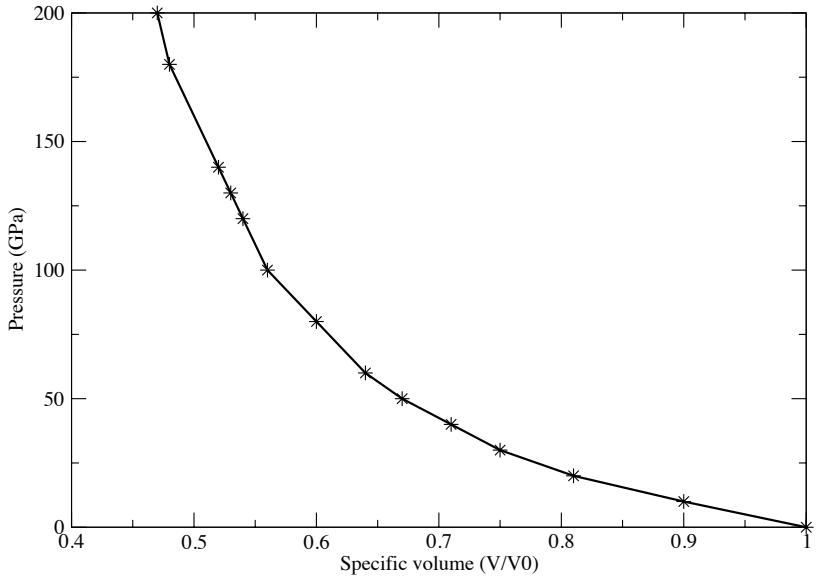

Figure 5.15: Static compression of quartz using the BKS potential plus extension. The points above 50 GPa are calculated using the extension to the BKS potential.

5.3 Shock wave simulations

5.3.1 Shock waves in systems with charge

The Lennard-Jones simulations approach for creating shock waves was used for creating the shock wave systems: a vacuum gap was added to ensure that there was no interaction between the end planes of atoms. For systems that have charge, such as quartz, this creates a large dipole moment in the system due to the removal of the periodicity in the z-direction. This has catastrophic consequences for the geometry optimisation as the ends of the system are drawn together across the vacuum region by Coulomb attraction to counteract the dipole moment. In order to get a stable system with which to perform the shock wave simulations, the Coulomb force computation (using Ewald summation) has to be performed only in the directions perpendicular to the shock propagation direction. Therefore the Ewald summation was performed essentially in two-dimensions and the system had the geometry of a slab of material. There are two-dimensional (2D) Ewald summation methods available [Spohr, 1997; Kawata and Nagashima, 2001; Grzybowski *et al.*, 2000], however these are computationally expensive, especially for large systems. A correction to the three-dimensional (3D) Ewald summation technique was proposed by Yeh and Berkowitz [1999], which they denoted as EW3DC and they showed that their correction to 3D Ewald summation is much more computationally efficient than using a 2D Ewald summation technique. The EW3DC uses a shape dependent energy correction, $J(\mathbf{M},P)$, where P is the summation geometry of the system. The total dipole moment is given by:

$$\mathbf{M} = \sum_{i=1}^{N} q_i \mathbf{r}_i \tag{5.2}$$

where q_i is the charge on the ith atom, at position $\mathbf{r}_i$. The systems studied here had the geometry of a rectangular slab (P=R) and therefore the energy correction term was given by:

$$J(\mathbf{M},R) = \frac{2\pi}{V}\mathbf{M}_z^2 \tag{5.3}$$

using atomic units, and where V is the volume of the (3D) system. The correction is also applied to the force calculation, which is obtained by differentiation of the energy term:

$$F(\mathbf{r}) = \frac{\partial J(\mathbf{M},R)}{\partial \mathbf{r}} = \frac{4\pi q_i}{V}\mathbf{M}_z \tag{5.4}$$

This correction holds provided that the length of the simulation cell in the shock di-

rection (the non-periodic direction) is at least greater than three times the length of the largest of the simulation cell lengths perpendicular to the shock direction, i.e. $L_z > 3 * max(L_x, L_y)$. This EW3DC technique was employed for the shock wave simulations presented here. System tests using the corrected 3D Ewald were performed and the results (seen in figure 5.16) show how the EW3DC using a small L_z gives the long-range limit convergence of the 3D Ewald summation technique (when $L_z \rightarrow \infty$). The test system was successfully geometry optimised using this correction to the Ewald summation and a vacuum gap just larger than $3 * max(L_x, L_y)$ resulted in a system that was stable for molecular dynamics simulations. The calculation time using the correction and the small vacuum gap was 200 times faster than using the 3D Ewald summation using a 2000 Å vacuum gap.

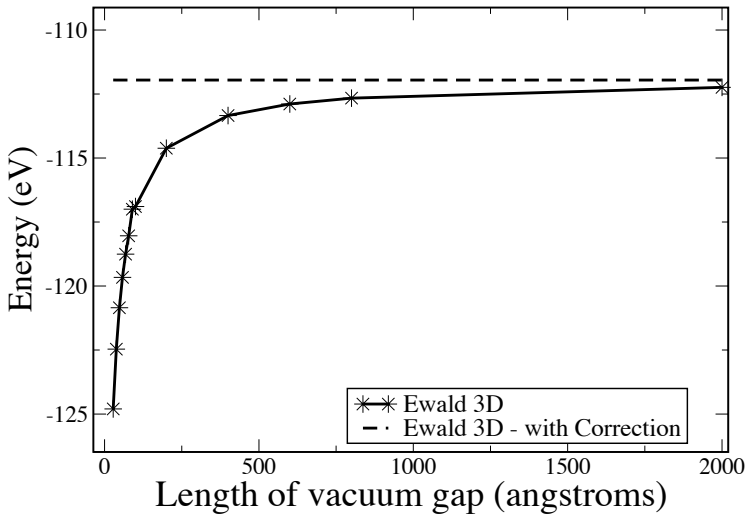

Figure 5.16: The energy with a correction to the 3D Ewald summation used for 2D systems gives the same value as the long-range limit of the 3D Ewald summation.

5.3.1.1 Shifting the system prior to optimisation

Prior to geometry optimisation of the larger shock wave simulation systems, all the atoms in the system were shifted away from the origin by up to 10 Å. This was a necessity, as a possible way for the geometry optimisation of the system to reduce the dipole moment was to move planes of atoms past the $z = 0$ plane, resulting in a negative contribution to the dipole moment. This is bad for a shock wave simulation as the momentum mirror would reflect the atoms passed the $z = 0$ plane thereby creating an unexpected high-density system. For this reason, a check after each geometry optimisation was performed to ensure the the 10 Å shift was sufficient.

5.3.2 Geometry optimisation of shock simulation systems

The geometry optimisation with correction to the Ewald summation was performed on systems of 1584 and 3600 atoms of α-quartz ($4 \times 4 \times 11$ and $4 \times 4 \times 25$ unit cells, respectively). The optimisation reduced the dipole moment of the systems to the order of 10^{-3} D. The variation in the dipole moment during geometry optimisation of the 3600 atoms system can be seen in figure 5.17. The majority of the bulk of the system remained unaltered however. This is determined by considering the radial distribution function (RDF) of the system, which is plotted in Figure 5.18 and indicates that the majority of the structure remained that of β-quartz.

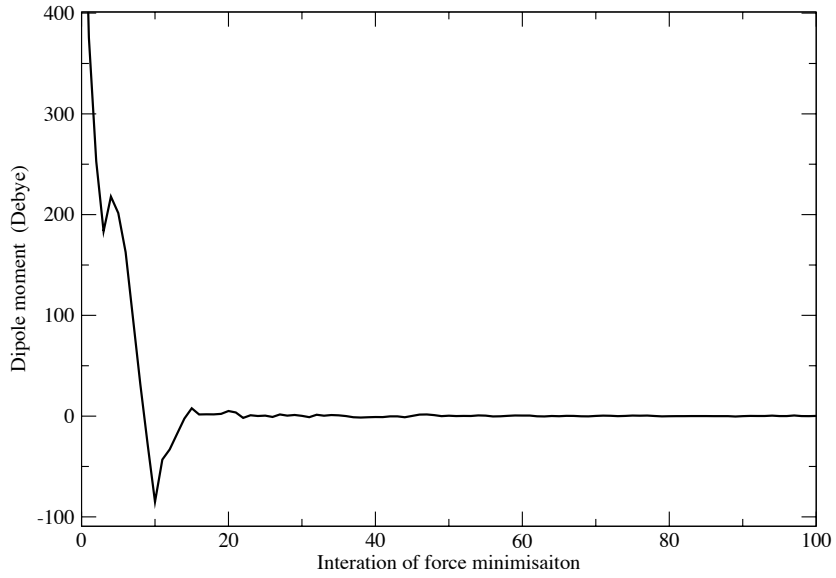

Figure 5.17: Dipole moment of quartz system during geometry optimisation. The geometry optimiser was able to reduce the moment to zero and thereby created a stable system for shock wave simulations.

5.3.3 Equilibration

The systems were equilibrated to 300 K using a Berendsen thermostat for 5 ps followed by a further 5 ps of NVE simulation. Figure 5.19 shows the temperature of the system over the equilibration period.

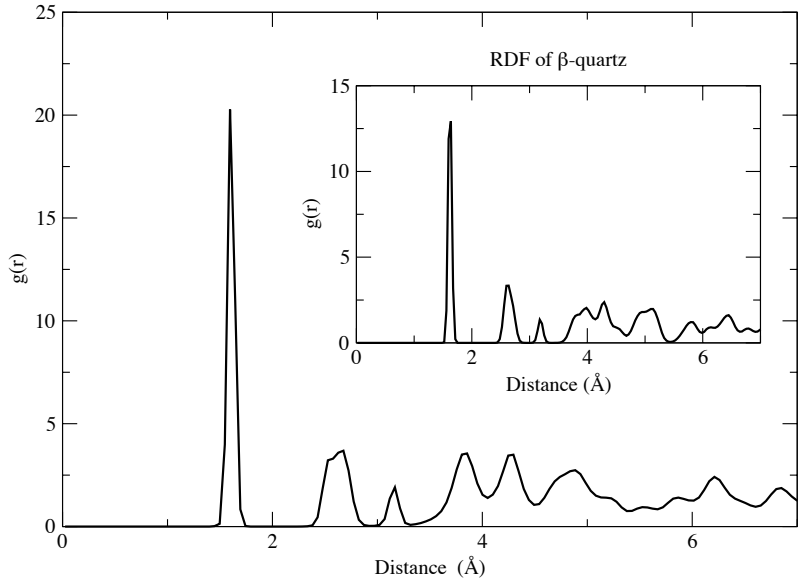

Figure 5.18: Radial distribution function (g(r)) of quartz system post geometry optimisation. Inset: g(r) of β-quartz for comparison.

5.3.4 Simulation results

A shock wave was created in the systems by using the so-called momentum mirror technique [Holian, 1988], located at $z = 0$. All atoms in the system were given a piston velocity of $-u_p = 1$ km/s,2 km/s,6 km/s,12 km/s towards the momentum mirror. A shock wave thus propagated in the positive z direction at velocity u_s. The system incorporated a vacuum gap in the z-direction which was created to be larger than the cut-off radii to ensure that the potential was not acting on atoms through the momentum mirror. The Ewald correction method of Yeh and Berkowitz was employed. Periodic boundary conditions (PBC) in all directions were used throughout. The system was equilibrated to 300 K using a Berendsen thermostat and then further equilibrated for 2 ps using standard NVE dynamics before the shock wave was initiated. The longitudinal sound speed in crystalline quartz is 5.7 km/s, and rises to 6 km/s in amorphous (fused) quartz.

5.3.4.1 Piston velocity

The piston velocity and shock velocity plots for the system are shown in figure 5.20. There is a clear linear relationship between the shock and piston velocities. This indicates that the piston passed through the system with little resistance. The system behaved like a fluid and this could be attributed to the momentum mirror being in-

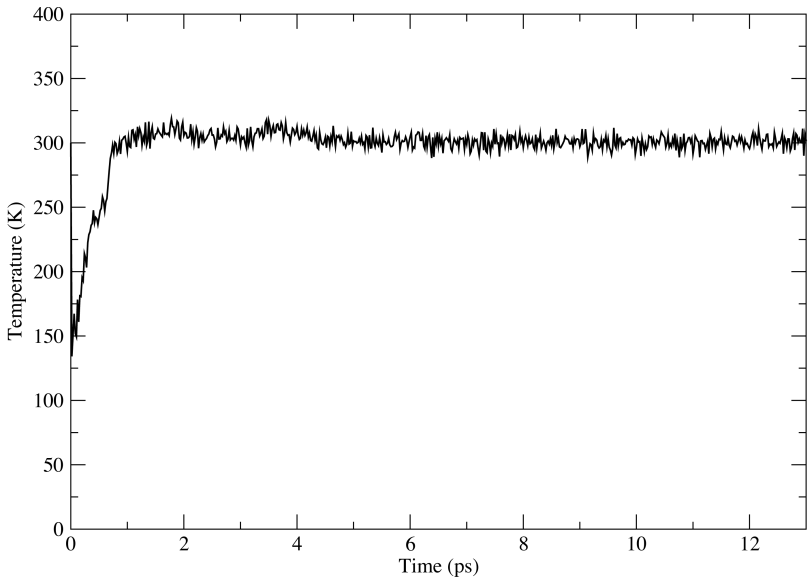

Figure 5.19: Equilibration of quartz system to 300K using a Berendsen thermostat for 5 ps, switching to NVE simulation for a further 5 ps.

finitely massive and therefore too "hard", although work by Wackerle [1962] indicates that quartz loses all rigidity at pressures above its Hugoniot Elastic Limit (HEL) which is around 6 GPa.

5.3.4.2 The Hugoniot

The Hugoniot generated for the quartz system is plotted in figure 5.21 along with the experimentally determined data of Wackerle [1962] and data from Los Alamos Scientific Laboratory (LASL) collated in Marsh [1980]. It is clear that the simulation data covers a much stronger shock compression region than the experimental data. The calculated maximum pressure (stress) along the shock direction is greater than that observed in the strongest shock compression experimental datum. Although the experimental data have no error bars, similar shock compression experiments performed by Fowles [1967] are in excellent agreement. Therefore the discrepancy between the calculated Hugoniot and the experiment is likely due to the probing of the region of the pair potential that was far from its equilibrium region, and consequently is not a good description of quartz at such high-pressures. However, there was another possibility; that the infinitely massive momentum mirror was causing the discrepancy. To investigate this an improved momentum mirror was constructed.

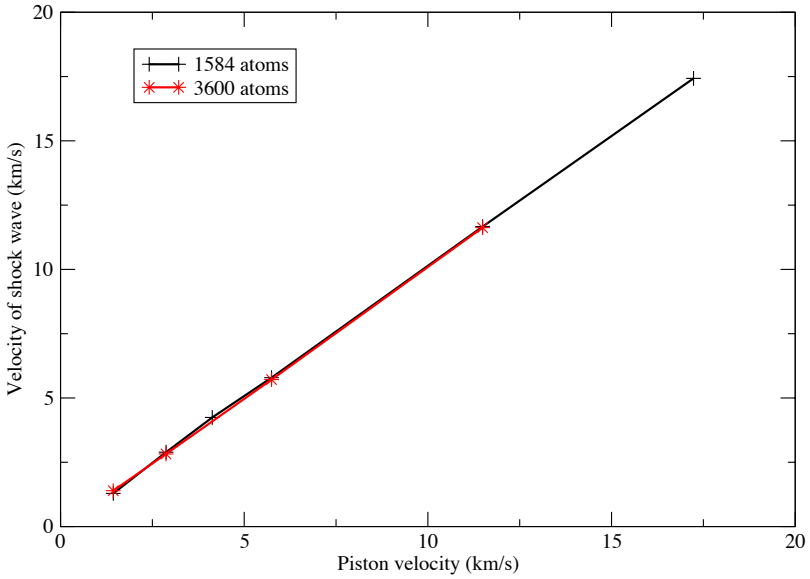

Figure 5.20: Shock velocity against particle velocity plot for quartz using an infinitely massive momentum mirror.

5.4 Improvements to the momentum mirror

The results above suggest that the momentum mirror is too hard and unrealistically compresses the quartz systems. An improvement to this "infinitely massive" momentum mirror to make the compression more realistic was to replace the momentum mirror by a block of the sample to be shocked (in this case, quartz). The block interacts with the system via the interatomic potential and is analogous to the flyer-plate for the experimentally created shock waves. Calculations using this momentum mirror shall be referred to as the flyer-plate simulations.

5.4.1 Considerations using a flyer-plate momentum mirror

As already discussed in section 3.8.1 there are implications to consider when using the hard momentum mirror. The flyer-plate momentum mirror also requires careful consideration as there were simulation difficulties to overcome. The main difficulty in using a block of the same material as the sample was to make sure that the sample did not destroy the flyer-plate on impact. One way of doing this was to zero any forces and velocities on the atoms that constituted the flyer-plate, but this had severe problems with the total energy of the system. The momentum mirror drained the energy of the incoming atoms and resulted in an unrealistic build-up of atoms at the interface. This approach also violated the conservation of momentum. A better method was to give the

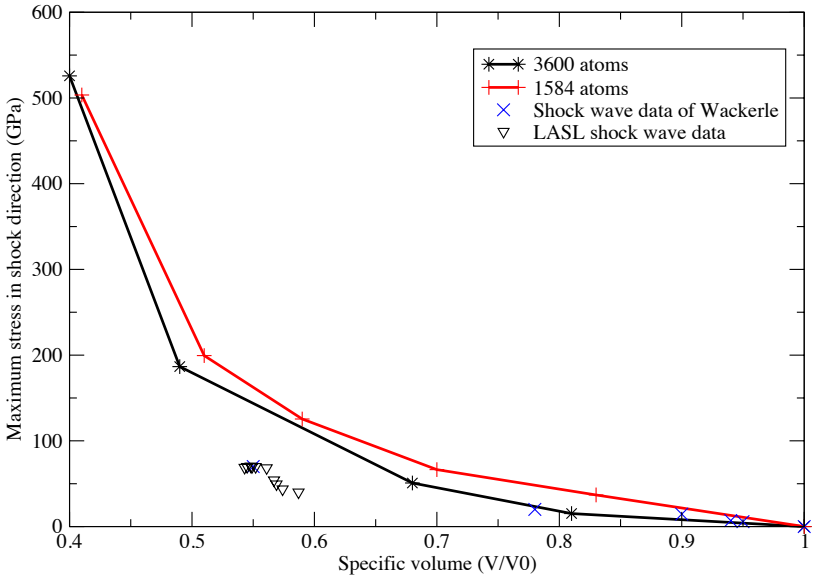

Figure 5.21: Hugoniot of quartz along with experimental data of Wackerle [1962] and Marsh [1980].

flyer-plate atoms a much larger mass than they would normally have. This ensured that the conservation of momentum was maintained as the flyer-plate would move slightly on impact with the sample. To ensure the surface of the flyer-plate was representative of a sample surface, the flyer-plate was geometry optimised in the same way as the simulation cell.

5.4.2 Flyer-plate simulations

Figure 5.22 shows a 2D slice (taken at $x = 0$ plane, which is into the paper) schematic of the flyer-plate momentum mirror (left) and the simulation atoms (right) separated with a vacuum gap of 10 Å (greater than the cut-off radii) so that the atoms in the flyer-plate and the simulation atoms were not interacting at the start of the simulation. Periodic boundary conditions were used throughout and a vacuum region (left of flyer-plate) was used to ensure no interactions between the simulation atoms and the flyer-plate atoms.

Figure 5.23 shows the average particle velocity profiles for a piston velocity u_p=5.74 km/s. From the figure the shock thickness is estimated to be 10 Å in width and the shock velocity is determined to be 6.44 km/s by considering the distance between the profiles, which means the shock front is moving 10% faster than the average particle velocity. Figures 5.24 and 5.25 illustrate the shock wave's progress as a snapshot during the

Figure 5.22: Schematic of a flyer-plate momentum mirror technique used for a quartz shock wave. Image is a 2D slice (taken at $x = 0$ plane, which is into the paper) of a 3D simulation. The flyer-plate (left) is created from an optimised quartz system. The simulation atoms (right) are moving towards the flyer-plate. The flyer-plate and the simulation atoms were separated by a vacuum gap to avoid interactions at the start of the simulation. Periodic boundary conditions were used throughout.

simulation. Behind the shock front there is clearly little structure, which indicates an amorphous state. The radial distribution function is plotted in figure 5.26. From the figure, it is clear that structural information is lost after the first oxygen-oxygen distance (approximately 2.6 Å). Therefore it was concluded that quartz transforms to an amorphous state when subjected to a strong shock compression.

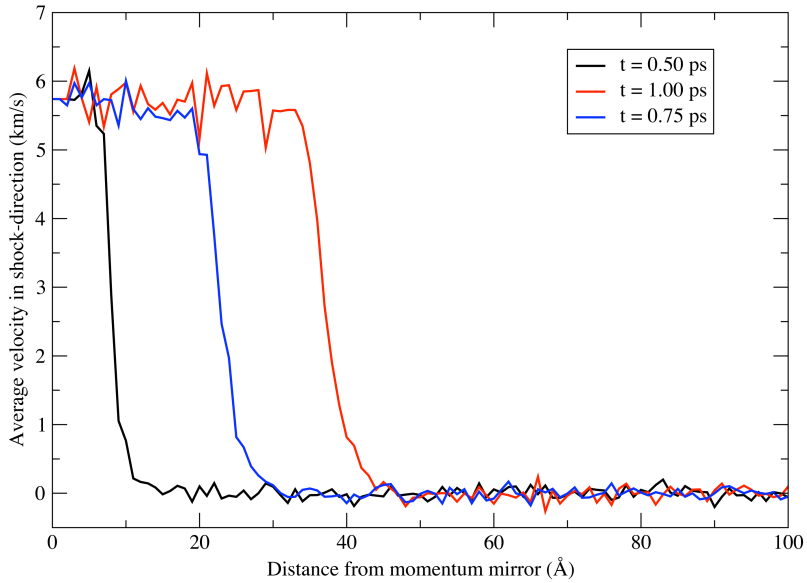

Figure 5.23: Average particle velocity profiles for a shock wave in quartz. u_p = 5.74 km/s.

The Hugoniot for quartz using the flyer-plate momentum mirror is shown in figure 5.27. Much better agreement is observed at lower pressures with the experimental data, indicating that the new momentum mirror is an improvement over the old momentum mirror. However, at high-pressure the Hugoniots diverge to very high pressures away from the experimental data. In this region, the pressures caused the atoms

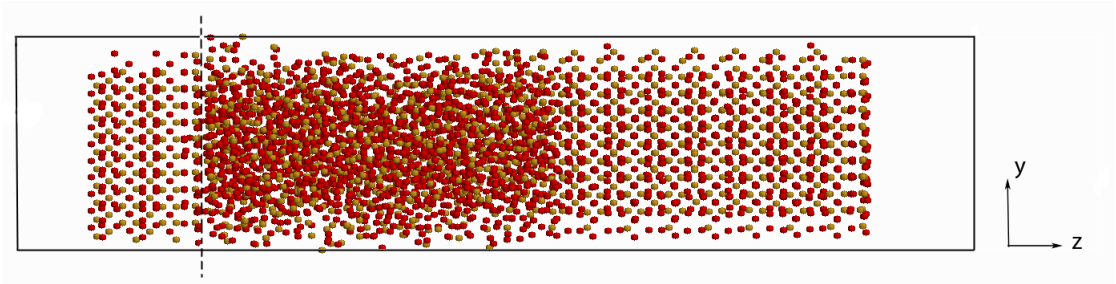

Figure 5.24: 2D slice of a 3D shock wave simulation taken at $x = 0$ plane. Snapshot of 3600 atoms of quartz half-way through the simulation. Left of dotted line is the flyer-plate momentum mirror. To the right of the dotted line the shock wave is propagating away from the flyer-plate and creating an amorphous region behind the shock front.

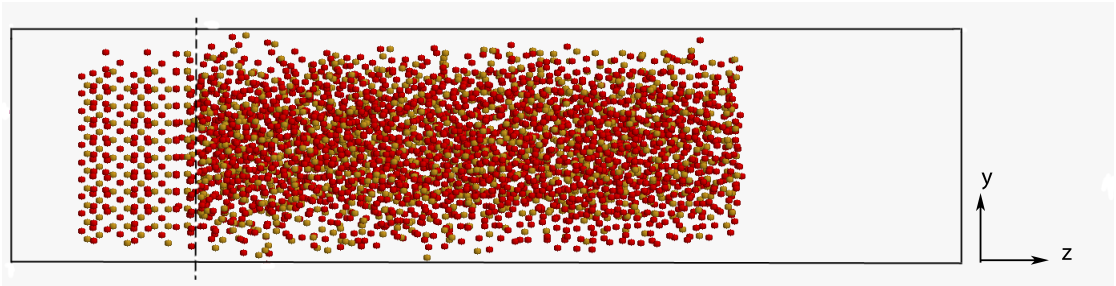

Figure 5.25: 2D slice of a 3D shock wave simulation taken at $x = 0$ plane. Snapshot of 3600 atoms of quartz at maximum compression. Left of dotted line is the flyer-plate. Right of dotted line it can be seen that there is no discernible structure in the system, indicating an amorphous state.

to be closer than could be modelled using the BKS potential and the modification for high-pressures was used almost exclusively. As this potential was a numerical fit to the BKS potential at the point of inflection and had no precise justification for this form, this diversion is unsurprising. It was concluded that this extension to the BKS potential should be re-visited to give a much stronger repulsion.

5.4.3 Stronger repulsive BKS extension

A single calculation using the flyer-plate momentum mirror was performed to see the effect on the Hugoniot of a BKS potential with a stronger repulsion term for the extension to high pressures. The form of the fitting term was:

$$U(r) = \frac{\alpha}{r^4} + \frac{\beta}{r^{12}} + \gamma \qquad r < r^* \tag{5.5}$$

Table 5.4 gives the fitted values of the extension at the point of inflection.

The effect on the Hugoniot can be seen in figure 5.28. The datum point is in much better agreement with the experimental data, although it is clear that the datum point still is above the experimental data.

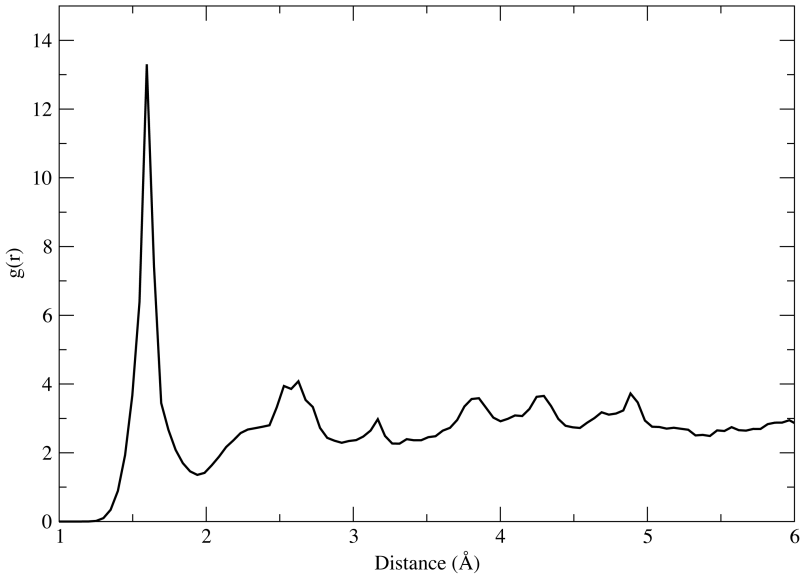

Figure 5.26: Radial distribution function of quartz system in the shocked state. The loss of structural information indicates the system is in an amorphous state.

Table 5.4: Numerical values of the fitting parameters used for BKS correction.

	$\alpha(eV\AA^2)$	$\beta(eV\AA^6)$	$\gamma(eV)$
Si-O	31.422	-15.048	-6.095
O-O	56.943	506.444	-0.810

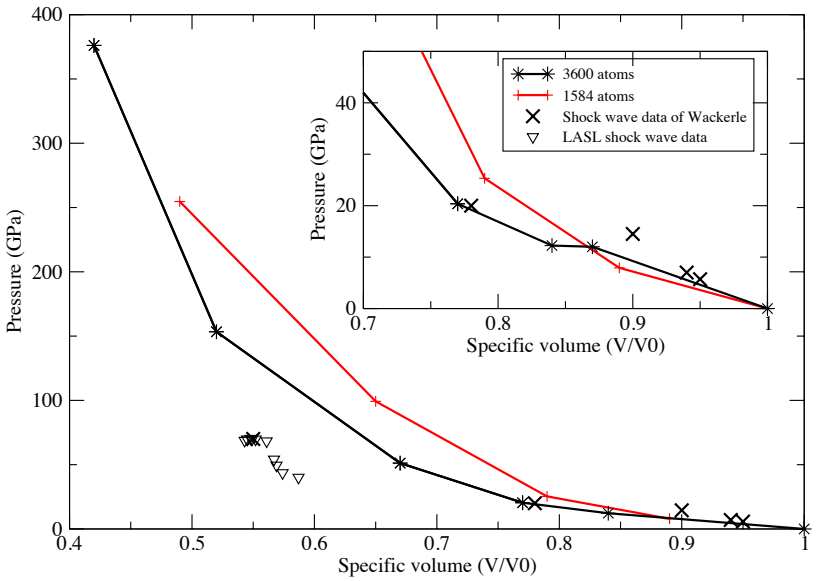

Figure 5.27: Hugoniot of shocked quartz using the flyer-plate momentum mirror technique along with experimental data of Wackerle [1962] and Marsh [1980]. Inset: Detailed view of 0 GPa to 40 GPa region.

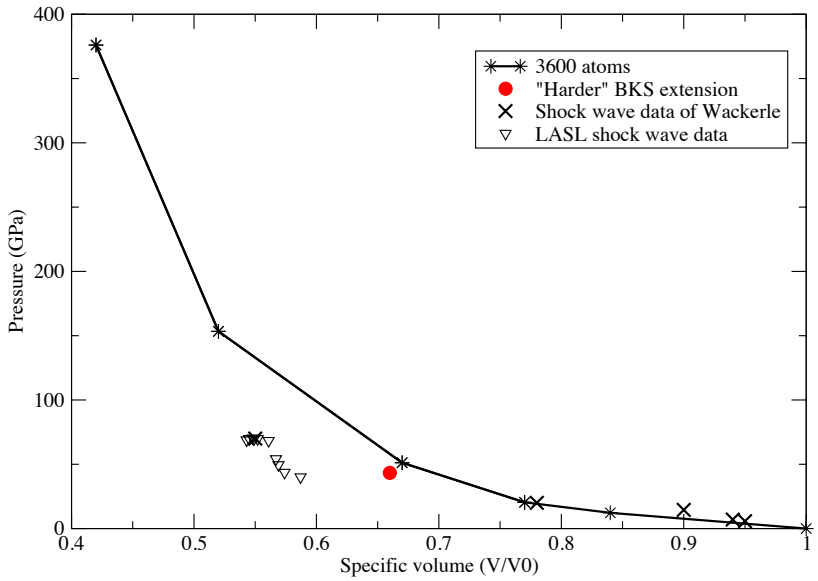

Figure 5.28: Hugoniot of shocked quartz using the flyer-plate momentum mirror technique. Red data highlights use of more repulsive BKS extension. Experimental shock wave data of Wackerle [1962] and Marsh [1980] is also plotted for comparison.

5.5 Summary

This chapter showed that simulations on quartz using the well-known BKS potential of van Beest *et al.* [1990] had issues with low temperature and pressure calculations due to the equilibrium structure of quartz (for this potential) being β-quartz. With that knowledge, hydrostatic compression and shock wave simulations were performed on β-quartz and it was found that under hydrostatic compression, a second-order phase transformation to α-quartz occurs at 7 GPa. It was also found that the BKS potential failed (went beyond the point of inflection of the pair part of the potential) at 50 GPa. An extension to the pair part of the BKS potential was proposed that was used when the interatomic separation became smaller than at the point of inflection. Any shock simulation that generated a pressure greater than 50 GPa would result in using the extension to the BKS potential and therefore would not necessarily provide an accurate description of high-pressure quartz, but should give an indication of the structure at that pressure.

The problem with using the current methodology for a periodic system containing point charges was outlined; that a dipole moment which is created when adding a vacuum gap to the shock direction creates an unstable system unsuitable for shock compression. This problem was overcome by using a correction to the three-dimensional

Ewald summation as proposed by Yeh and Berkowitz (EW3DC). The EW3DC was shown to give the correct long-range limit result for a 3D Ewald summation, and allowed for a stable system to be created in which to perform the shock wave simulations with less computational effort than that required for a completely 2D Ewald summation. The momentum mirror used for the Lennard-Jones systems was found to be too hard for the quartz systems, and resulted in a "fluid-like" response. It is known that above the HEL quartz does indeed lose all rigidity [Wackerle, 1962], however the computed Hugoniot was a poor fit to the experimental data and showed much larger pressures and smaller specific volumes. A new momentum mirror was devised that behaved similar to the flyer-plate shock wave experiments and was called the flyer-plate momentum mirror. The simulations involving the flyer-plate showed much better agreement with the experimental data at low pressures but still diverged at higher pressures. This was due to the extension to the BKS potential that allowed such pressures to be simulated, as it was the predominant function term of the potential being used at those pressures. This extension was a numerical fit to the point of inflection using a polynomial. An exemplar calculation was performed with a much stronger repulsion and showed a lowering in the calculated pressure which corresponded well with experimental data. It was concluded that a stronger repulsion polynomial would provide better agreement with the experimental results. It was found that the structure of the shocked state was amorphous which agrees with the "fluid like" response of quartz observed by experimental researchers. With regard to whether α-quartz (or β-quartz) transforms to stishovite or coesite, the high-pressure polymorphs of quartz, the result that the shocked state is amorphous does not mean that the transformation does not take place. Indeed, after the shocked state is released these polymorphs may crystallise out of the amorphous structure. Although the release structures are for future work, it is important to remember that stishovite was first located in meteorite craters [Chao *et al*., 1962; Martini, 1978] and coesite and stishovite are now readily achievable in high-pressure laboratory experiments [Stishov and Belov, 1962].

References

A. Akhavan. Overview of Silica Polymorphs. http://www.quartzpage.de, 2005. last visited: 1 May 2009.

T. Araki and T. Zoltai. Refinement of a coesite structure. *Zeitschift fur Kristallogaphie, Kristallgeometrie,Kristallphyik, Kristallchemie*, 129:381, 1969.

F. Barmes, L. Soulard, and M. Mareschal. Molecular dynamics of shock-wave induced structural changes in silica glasses. *Phys. Rev. B*, 73:224108, 2006.

W. H. Baur and A. A. Khan. Rutile-type compounds. IV. SiO_2, GeO_2 and a comparison

with other rutile-type structures. *Acta Crystallographica Section B*, 27(11):2133–2139, 1971.

W. Bragg and R. E. Gibbs. The structure of alpha and beta quartz. *Proc. R. Soc. Lond. Ser. A-Contain. Pap. Math. Phys. Character*, 109:405–427, 1925.

E. C. T. Chao, J. J. Fahey, J. Littler, and D. J. Milton. Stishovite, SiO2, a very high pressure new mineral from meteor crater, Arizona. *J. Geophys. Res.*, 67:419, 1962.

R. Fowles. Dynamic compression of quartz. *J. Geophys. Res.*, 72:5729, 1967.

A. Grzybowski, E. Gwóźdź, and A. Bródka. Ewald summation of electrostatic interactions in molecular dynamics of a three-dimensional system with periodicity in two directions. *Phys. Rev. B*, 61(10):6706–6712, 2000.

A. F. Gualtieri. Accuracy of XRPD QPA using the combined Rietveld–RIR method. *Journal of Applied Crystallography*, 33(2):267–278, 2000. doi: 10.1107/S002188989901643X.

Y. Guissani and B. Guillot. A numerical investigation of the liquid-vapor coexistence curve of silica. *J. Chem. Phys.*, 104:7633–7644, 1996.

R. J. Hemley, A. P. Jephcoat, H. K. Mao, L. C. Ming, and M. H. Manghnani. Pressure-induced amorphization of crystalline silica. *Nature*, 334:52–54, 1988.

D. G. Hicks, T. R. Boehly, P. M. Celliers, J. H. Eggert, E. Vianello, D. D. Meyerhofer, and G. W. Collins. Shock compression of quartz in the high-pressure fluid regime. *Phys. Plasmas*, 12:82702, 2005.

B. L. Holian. Modeling shock-wave deformation via molecular-dynamics. *Phys. Rev. A.*, 37:2562–2568, 1988.

M. Kawata and U. Nagashima. Particle mesh Ewald method for three-dimensional systems with two-dimensional periodicity. *Chem. Phys. Lett.*, 340:165–172, 2001.

G. J. Kramer, N. P. Farragher, B. W. H. van Beest, and R. A. van Santen. Interatomic force-fields for silicas, aluminophosphates, and zeolites - derivation based on ab initio calculations. *Phys. Rev. B*, 43:5068–5080, 1991.

S.P Marsh, editor. *LASL Shock Hugoniot data*. University of California Press, 1980.

J. E. J. Martini. Coesite and stishovite in Vredefort Dome, South-Africa. *Nature*, 272: 715–717, 1978.

R. L. Mozzi and B. E. Warren. Structure of vitreous silica. *J. Appl. Crystallogr.*, 2: 164–&, 1969.

M. D. Segall, P. J. D. Lindan, M. J. Probert, C. J. Pickard, P. J. Hasnip, S. J. Clark, and M. C. Payne. First-principles simulation: ideas, illustrations and the CASTEP code. *J.Phys.:Cond. Matt.*, 14:2717–2744, 2002.

W. Sinclair and A. E. Ringwood. Single-crystal analysis of structure of stishovite. *Nature*, 272:714–715, 1978.

E. Spohr. Effect of electrostatic boundary conditions and system size on the interfacial properties of water and aqueous solutions. *J. Chem. Phys.*, 107(16):6342–6348, 1997.

S. M. Stishov and N. V. Belov. Crystal structure of a new dense modification of silica SiO2. *DOKLADY AKADEMII NAUK SSSR*, 143:951, 1962.

S. Tsuneyuki, M. Tsukada, H. Aoki, and Y. Matsui. First-principles interatomic potential of silica applied to molecular dynamics. *Phys. Rev. Lett.*, 61(7):869–872, Aug 1988. doi: 10.1103/PhysRevLett.61.869.

B. W. H. van Beest, G. J. Kramer, and R. A. van Santen. Force-fields for silicas and aluminophosphates based on *ab initio* calculations. *Phys. Rev. Lett.*, 64:1955–1958, 1990.

J. Wackerle. Shock-wave compression of quartz. *J. App. Phys*, 33:922, 1962.

I. C. Yeh and M. L. Berkowitz. Ewald summation for systems with slab geometry. *J. Chem. Phys.*, 111:3155–3162, 1999.

Chapter 6

Re-parameterising the BKS Potential

6.1 Introduction

In this chapter the BKS potential for silicates as proposed by van Beest, Kramer, and van Santen [1990] which is a well known and used potential is re-parameterised using *ab initio* density functional theory data. The BKS potential has some limitations, such as predicting the wrong phase at zero kelvin and also the equation of state is not well reproduced. B.W.H. van Beest *et al.* used Hartree-Fock *ab initio* calculations and also experimental data for the original parameterisation. Carre *et al.* [2008] have re-parameterised the BKS potential using Car-Parrinello *ab initio* calculations and fitted the parameters for the charge, the silicon-oxygen terms, the oxygen-oxygen terms and also the silicon-silicon terms. The latter was excluded in the original BKS parameterisation as it was implicitly calculated using the functional form of the pair-potential. In this chapter the BKS parameters are re-evaluated by fitting to Density Functional Theory (DFT) calculations (using the GGA functional of Perdew-Burke-Ernzerhof (PBE) [Perdew *et al.*, 1996]) as the input vector to a non-linear fitting technique using the Newton method.

6.2 Non-linear fitting technique

A non-linear fitting technique using the Newton method was used to fit the BKS parameters to the DFT data. The Newton method is outlined as follows:

Consider a dataset as a sum of non-linear basis functions:

$$y(x) = \sum_{m=1}^{M} f_m(x, \mathbf{a}_m) \tag{6.1}$$

where $\mathbf{a}_m$ is a vector of input values into the function, $f(x)$. We seek to minimise the

error between the desired values and those that are generated using the above equation. The chi-squared function is a useful measure of the error:

$$\chi^2(\mathbf{a}) = \sum_{n=1}^{N} \left(\frac{y_n - y(x_n, \mathbf{a})}{\sigma_n} \right)^2 \tag{6.2}$$

where σ_n is a measure of the error in the data that is to be fitted. We require an iterative search to find the best solution. If we evaluate the gradient of the error with respect to the input parameters (equation 6.2) and also its second derivative (the Hessian) we get equations 6.3 and 6.4 respectively.

$$(\nabla\chi^2)_k = -2 \sum_{n=1}^{N} \frac{y_n - y(x_n, \mathbf{a})}{\sigma_n^2} \frac{\partial y(x, \mathbf{a})}{\partial a_k} \tag{6.3}$$

$$\mathbf{H}_{kl} = \frac{\partial^2 \chi^2}{\partial a_k \partial a_l} = 2 \sum_{n=1}^{N} \frac{1}{\sigma_n^2} \left\{ \frac{\partial y(x_n, \mathbf{a})}{\partial a_k} \frac{\partial y(x_n, \mathbf{a})}{\partial a_l} - [y_n - y(x_n, \mathbf{a})] \frac{\partial^2 y(x_n, \mathbf{a})}{\partial a_l \partial a_k} \right\} \tag{6.4}$$

It is customary in non-linear fitting to exclude the second term in the Hessian as it represents the sum of terms proportional to the residual between the model and the data and should be small if close to the minimum [Gershenfeld, 1999]. By taking a step in the direction that the error is decreasing the most rapidly, we can improve the parameters a_k and update the estimate in the error. This is the method of steepest descent as discussed in section 3.5 and the new values of the fitting parameters are given by:

$$\mathbf{a}_{new} = \mathbf{a}_{old} - \lambda \nabla \chi^2(\mathbf{a}_{old}) \tag{6.5}$$

where λ is the step size. However, if we are close to the minimum we can use Newton's method and expand χ^2 about a point $\mathbf{a}_0$ to second order:

$$\chi^2(\mathbf{a}) = \chi^2(\mathbf{a}_0) + \nabla\chi^2(\mathbf{a}_0) \cdot (\mathbf{a} - \mathbf{a}_0) + \frac{1}{2}(\mathbf{a} - \mathbf{a}_0) \cdot \mathbf{H} \cdot (\mathbf{a} - \mathbf{a}_0) \tag{6.6}$$

which has a gradient:

$$\nabla\chi^2(\mathbf{a}) = \nabla\chi^2(\mathbf{a}_0) + \mathbf{H} \cdot (\mathbf{a} - \mathbf{a}_0) \tag{6.7}$$

The new parameters are then given by iterating:

$$\mathbf{a}_{new} = \mathbf{a}_{old} - \mathbf{H}^{-1} \cdot \nabla\chi^2(\mathbf{a}_{old}) \tag{6.8}$$

where $\nabla\chi^2(\mathbf{a}) = 0$ at the minimum.

6.3 Sensitivity analysis

Prior to force matching with DFT data, the sensitivity of each of the BKS input variables was determined. Starting from the initial parameters, each parameter was perturbed from its value (up to $\pm 10\%$) and the effect on the pair potential plot was observed. Figure 6.1 shows that the A_{OO} and A_{SIO} parameters were most robust to changes in their values as a large change in the "A" parameters resulted in a negligible effect for the equilibrium values (interatomic distance=2.5 $\AA$ and 1.61 $\AA$ for O-O and Si-O bonds, respectively) of the BKS potential. Deviations from the original parameterisation only occured at high-pressure, when the interatomic distance is less than 2.5 $\AA$. In contrast, the potential was quite susceptible to changes in the "b" parameters as a change of only $\pm 20\%$ resulted in large deviations from the original potential. The C_{O-O} parameter was also very robust to large perturbations, more so than the C_{Si-O} parameter. Overall the analysis showed that a positive increase in the potential parameters would give the potential a stronger core repulsion and this was useful for shock wave simulations. However to maintain a physical justification for increasing the potential values force matching was still performed. It was expected that the force matching would yield increases in the variables' values.

6.4 Force matching

The force matching procedure adopted here was fitting (matching) the pair potential part of the BKS potential to *ab initio* DFT data. The details are as follows: An α-quartz system of 243 atoms ($3 \times 3 \times 3$ unit cells) was equilibrated at zero pressure using the BKS empirical potential with a Berendsen thermostat set to 300 K and then a further 15 ps using the NVE ensemble. This structure was not geometry optimised, as that would have resulted in a β-quartz state and our aim was to reparameterise the BKS pair potential for α-quartz. A single configuration of atoms was taken from the (NVE) molecular dynamics data to use as the input simulation system for the DFT calculations. A single MD step was performed using both the LDA functional and the GGA functional of Perdew-Burke-Ernzerhof (PBE) [Perdew *et al.*, 1996]) at a cut-off energy of 600 eV and a k-point spacing on 0.04 $\AA^{-1}$. The computed forces on each atom were used to make an input vector of 729 components for the force matching procedure (3 force components per atom). The input parameters to the BKS potential were A_{SiO}, A_{OO}, b_{SiO}, b_{OO}, C_{SiO}, C_{OO} and q_{Si}. However the latter was kept fixed at $q_{Si} = -1.2$ due to Mulliken population analysis of DFT calculations using

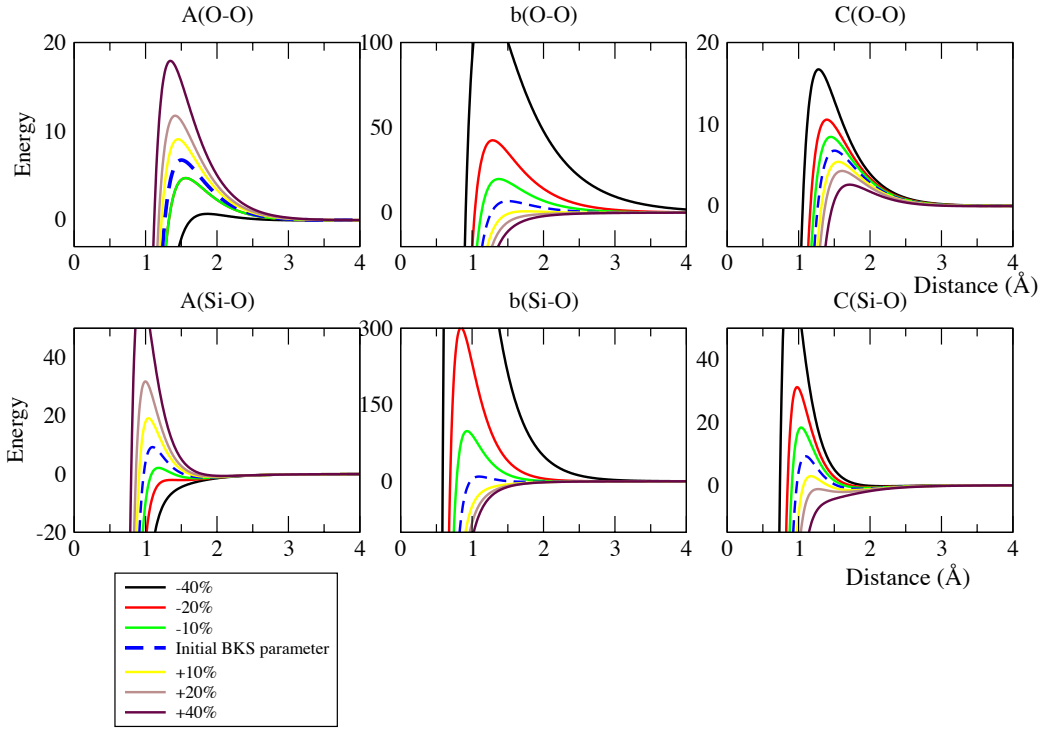

Figure 6.1: Variation of the pair-potential part of the BKS potential with input paramters. The dotted line represents the original BKS parameterisation. The "A" and "C" parameters were most robust to changes in their values whereas the "b" parameters showed most sensitivity.

CASTEP [Segall *et al.*, 2002] on α-quartz and β-quartz (for both LDA and GGA functionals) which showed that this was a good value to use. Therefore the Coulombic forces calculated by Ewald summation would be the same for the empirical and the *ab initio* DFT calculations and so the Ewald force was subtracted from the input vector. Therefore, in essence, the force matching was performed only on the pair-potential part of the BKS potential.

6.4.1 Previous re-parameterisations

The BKS potential has been re-parameterised recently by Carre *et al.* [2008] for amorphous silica. They used Car-Parrinello molecular dynamics simulations to obtain a pair-correlation function that they used to match the BKS potential variables using an iterative Levenberg-Marquardt algorithm. Figure 6.2 shows the form of their pair part of the BKS potential. The parameters used in the potential of Carre *et al.*, which they called CHIK, are given in table 6.1. The CHIK potential allowed the charge on the silicon and oxygen atoms to be used as fitting parameters and one can see that their final fitted parameters were different from those that were calculated from Mulliken

population analysis of DFT. They also included a silicon-silicon pair potential that in the original parameterisation was not required [van Beest *et al.*, 1990]. The CHIK potential gave good agreement for the structural and dynamic properties of amorphous quartz when compared to experimental values.

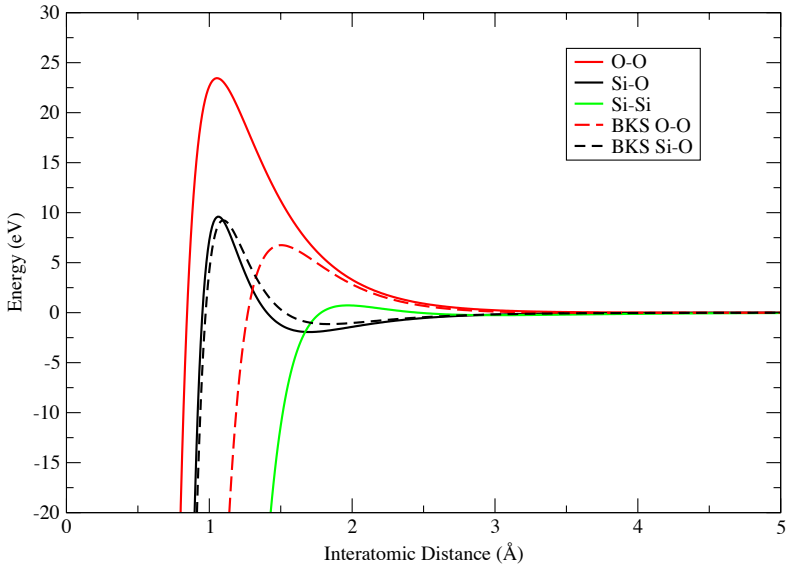

Figure 6.2: Plot of the pair part of the BKS potential using the parameters of Carre *et al.* [2008]. Dotted line represents the original BKS parameterisation.

6.4.2 Results of the force fitting

Force matching using the Newton method was performed on both the LDA and GGA functionals and each converged the value of χ^2 per degree of freedom to $\sim 10^{-5}$. The fitted BKS parameters for the functionals are given in table 6.2. The form of the fitted potentials as compared with the original BKS pair potential is shown in figure 6.3. It can be seen from the figures that the Si-O term gave a much stronger repulsion at small distances which is good for shock wave simulations. The parameters were used in a geometry optimisation of an α-quartz system of 243 atoms and the optimised structure remained that of α-quartz. The incorrect phase transformation to β-quartz did not take place. It is interesting to note that these are quite different numerically than those of the CHIK potential. This was likely due to the exclusion from the fitting of the charges on the silicon and oxygen and the fitting being performed on high-pressure α-quartz and not amorphous quartz as was done for the CHIK potential.

Table 6.1: Fitted parameters for CHIK potential [Carre *et al.*, 2008] used for amorphous quartz.

Parameter	CHIK	Units
q_i	1.910418	C
A_{OO}	659.595398	eV
b_{OO}	2.590066	$Å^{-1}$
C_{OO}	26.836679	eV$Å^6$
A_{SiO}	27029.419922	eV
b_{SiO}	5.158606	$Å^{-1}$
C_{SiO}	148.099091	eV$Å^6$
A_{SiSi}	3150.462646	eV
b_{SiSi}	2.851451	$Å^{-1}$
C_{SiSi}	626.751953	eV$Å^6$

Table 6.2: BKS pair potential parameters for quartz calculated using the LDA and GGA functionals

Functional		**A** (eV)	**b**($Å^{-1}$)	**C**($eVÅ^6$)
LDA	Si-O	11820.1278	5.2835	26.8727
	O-O	1787.3151	2.5472	628.1307
GGA	Si-O	11746.8622	5.2696	25.0866
	O-O	1814.6628	2.5346	645.2397

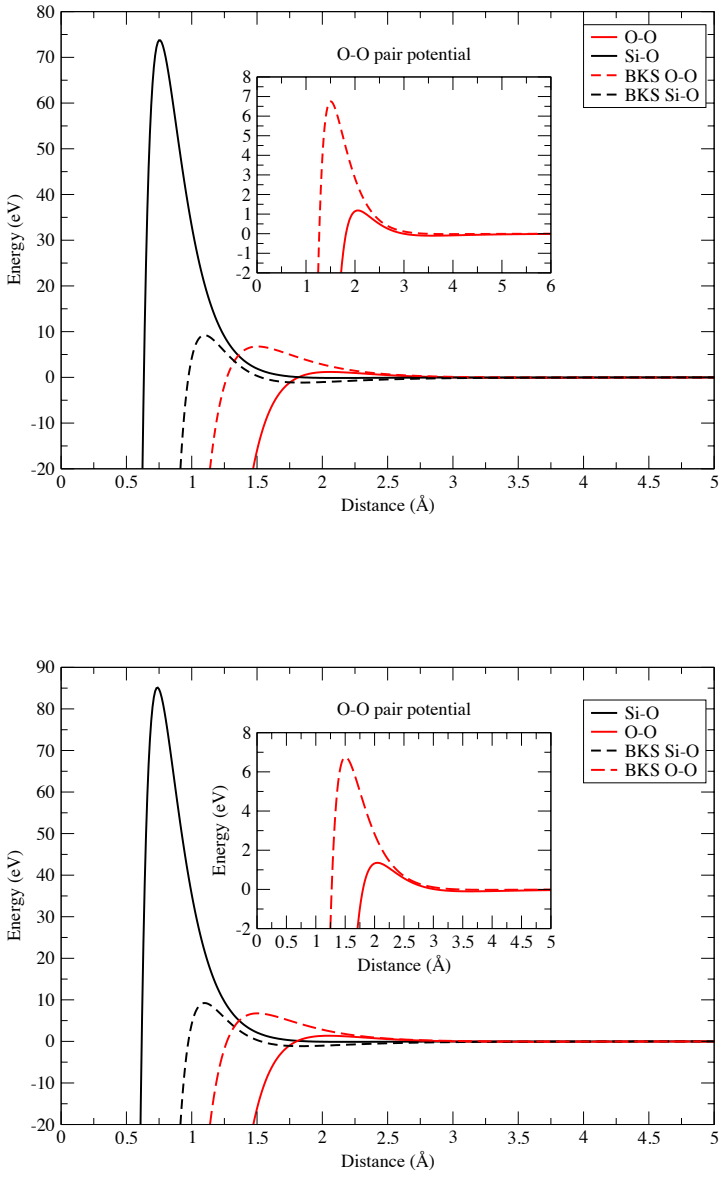

Figure 6.3: Plot of BKS pair potential with fitted parameters using LDA functional (top) and GGA functional (bottom). Original parameters plotted dashed for comparison. The Si-O term is much stronger, whereas the O-O term is softer for the fitted parameters than the original BKS parameters.

6.4.3 Hydrostatic compression

The new parameters for the BKS potential were tested for high-pressure behaviour by performing a series of hydrostatic compression calculations on 243 atom systems of α-quartz and β-quartz, a 864 atom system of coesite and a 1296 atom system of stishovite. The fitting parameters chosen were from using the GGA functional. The resulting pressure against specific volume plot can be seen in figure 6.4 alongside the original BKS parameterisation and an *ab initio* DFT calculation using the GGA functional of Perdew *et al*. [1996]. The structure of quartz remains that of α-quartz throughout the pressure range using the re-parameterised BKS potential and the pressure-volume curve much more closely follows the curve calculated from DFT using the PBE GGA functional. Although the re-parameterised BKS curve still tends to overbind much more than the *ab initio* curve there is a much better agreement at small pressures and compressions.
Using the re-parameterisation, the geometry optimisation failed to find a stable structure for the stishovite system. This was surprising as the original BKS parameterisation was able to optimise the same structure. The failure was put down to a number of factors such as the higher coordination number of stishovite (6 as opposed to 4 for the other polymorphs of quartz) and the fitting being performed on low pressure quartz whereas stishovite is a very high pressure polymorph of quartz. In fact, some researchers believe it to be quite distinct from the rest of the quartz "family", as it is regarded as an oxide rather than a silicate due to its structure being identical to other oxide minerals such as rutile (TiO_2) Sinclair and Ringwood [1978]. With the inclusion of high-pressure configurations of quartz in the fitting process, it is expected that a stable geometry-optimised structure of stishovite would be found.

6.4.4 Energy-volume curves

Figure 6.5 gives the energy-volume relationship for α-quartz, β-quartz and the high-pressure polymorphs, coesite and stishovite using both the original and the re-parameterised BKS potential. The energy-volume relationship between the two phases of quartz at the equilibrium volume (14 $\AA^3$) is almost identical using the original BKS potential (with β-quartz being slightly lower), whereas the α-quartz energy-volume curve is quite distinct from the β-quartz curve when using the re-parameterisation. The ordering of the coesite and stishovite polymorphs was the same for both parameterisations, however the re-parameterisation slightly favoured the coesite phase (lowest enthalpy). The β-quartz structure still had the lowest enthalpy for the larger volumes, away from the equilibrium volume and therefore the re-parameterisation offers no improvement over the original parameterisation for those situations, however overall the re-parameterisation was an improvement over the original.

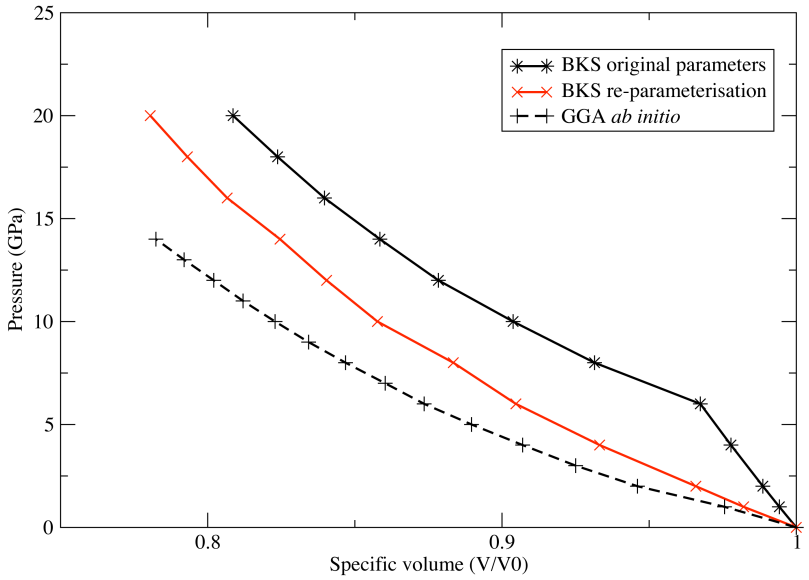

Figure 6.4: Hydrostatic compression curves of quartz. Plotted are re-parameterised BKS potential curve (with GGA functional fit parameters), original BKS parameterisation curve and an *ab initio* GGA functional of Perdew *et al*. [1996] DFT curve.

It was concluded that the re-parameterisation was an improvement on the original BKS potential for the low pressure phases of quartz but not for the high-pressure phases, as it yielded no improvement (however, it was not worse than the original parameterisation). This was a favourable result, noting that the fitting procedure was performed on low pressure α-quartz. Therefore to account for the high-pressure phases further configurations of high-pressure quartz would be needed in the DFT fitting process.

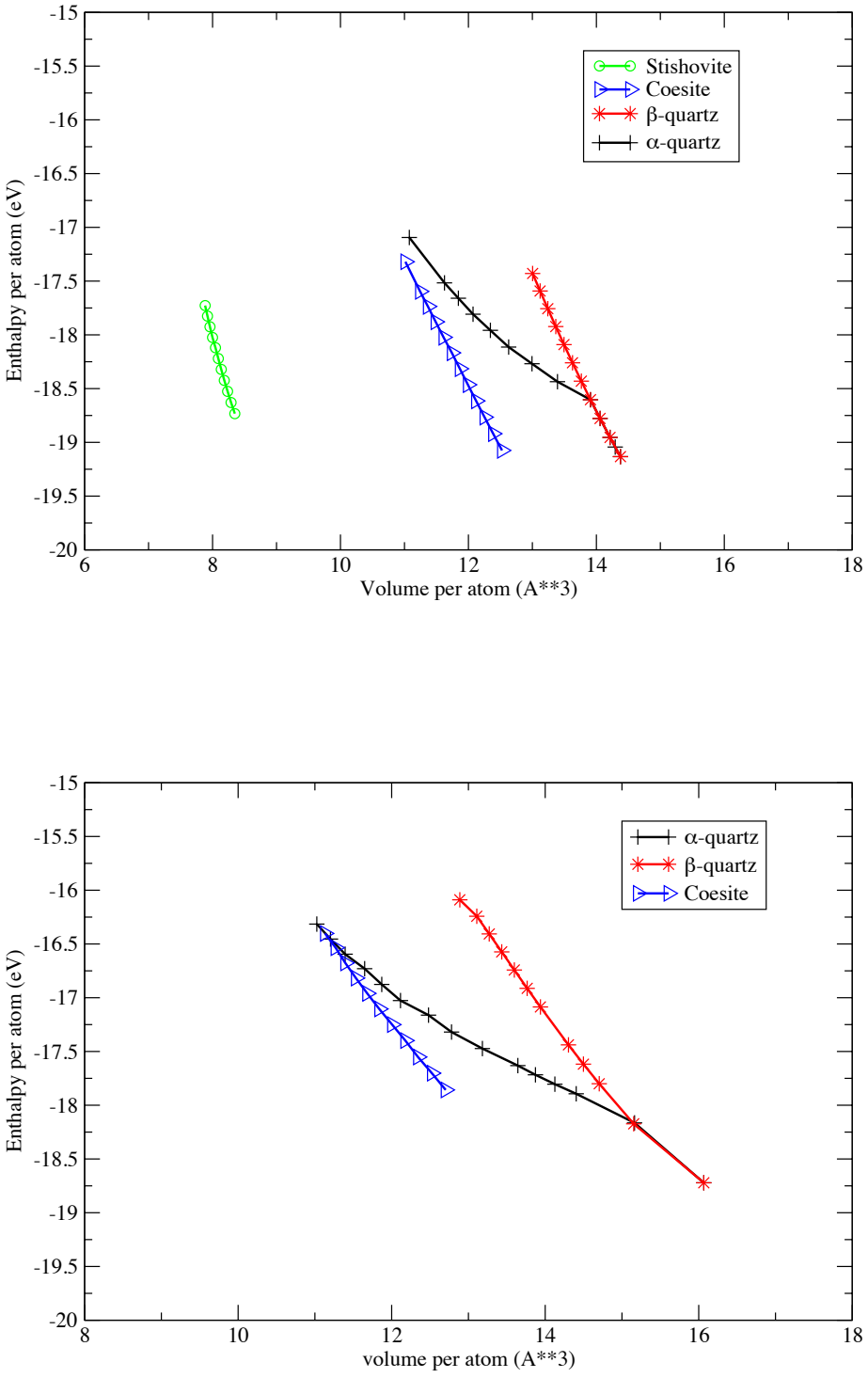

Figure 6.5: Energy-volume curves for hydrostatic compression of quartz and polymorphs. Top: Simulation using BKS parameters of van Beest *et al*. Bottom: Simulation using parameters calculated by fitting to DFT data.

6.4.5 c/a ratio

The c/a ratio for the (GGA functional) re-parameterised BKS potential was computed and can be seen in figure 6.6. The curve does not have the discontinuity of the original parameterisation (shown in figure 5.9) as the structure remains α-quartz throughout the pressure range.

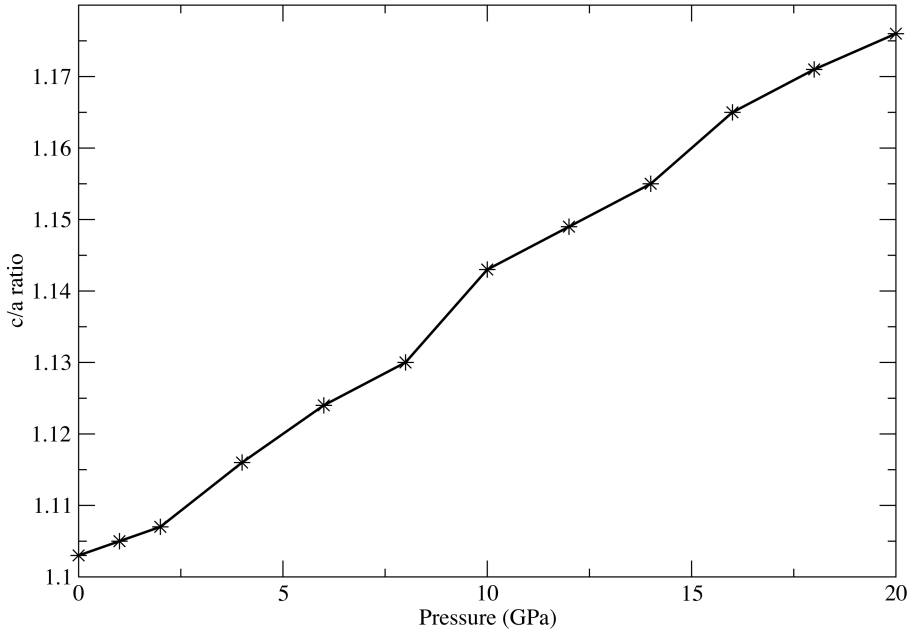

Figure 6.6: c over a ratio of hydrostatic compression of quartz using re-parameterised BKS potential with GGA functional fit parameters.

6.5 Summary

The well-known BKS potential has a number of shortcomings, such as the incorrect phase at zero pressure and the equation of state is not well reproduced. In this chapter the BKS potential was re-parameterised by force-fitting to *ab initio* density functional theory data on a low-pressure configuration of α-quartz using both the LDA and GGA functionals. The new parameters correctly gave α-quartz as the lowest phase for both functionals. The GGA functional re-parameterisation was then used to perform hydrostatic compression simulations and the pressure-volume curve much closely followed the *ab initio* DFT curve using the GGA functional over the original BKS parameterisation and did not result in any phase change across the pressure range considered. When considering the energy-volume curves, the reason for the re-parameterisation correctly giving α-quartz was apparent, as it had the lowest enthalpy of the two quartz phases. Calculations on coesite and stishovite were also performed and showed the same trend as the original parameterisation, although coesite was slightly lower in en-

thalpy than α-quartz for the re-parameterisation. A stable structure for stishovite could not be found using the re-parameterisation, however, the fitting was performed on low pressure α-quartz and so it was concluded that further configurations of high-pressure quartz were required in the fitting process to correctly describe the high-pressure structures. The re-parameterisation also allowed for compressions up to 70 GPa to be achieved, which is also an improvement on the original BKS parameterisation. Unfortunately, shock wave compression simulations using this re-parameterised potential were unable to be performed due to time constraints, however it is recommended that a Hugoniot is plotted for this re-parameterised potential as work for the future.

References

A. Carre, J. Horbach, S. Ispas, and W. Kob. New fitting scheme to obtain effective potential from Car- Parrinello molecular-dynamics simulations: Application to silica. *Europhys. Lett.*, 82:17001, 2008.

N. Gershenfeld. *The Nature of Mathematical Modeling*. Cambridge University Press, 1999. ISBN 0-521-57095-6.

John P. Perdew, Kieron Burke, and Matthias Ernzerhof. Generalized gradient approximation made simple. *Phys. Rev. Lett.*, 77(18):3865–3868, 1996.

M. D. Segall, P. J. D. Lindan, M. J. Probert, C. J. Pickard, P. J. Hasnip, S. J. Clark, and M. C. Payne. First-principles simulation: ideas, illustrations and the CASTEP code. *J.Phys.:Cond. Matt.*, 14:2717–2744, 2002.

W. Sinclair and A. E. Ringwood. Single-crystal analysis of structure of stishovite. *Nature*, 272:714–715, 1978.

B. W. H. van Beest, G. J. Kramer, and R. A. van Santen. Force-fields for silicas and aluminophosphates based on *ab initio* calculations. *Phys. Rev. Lett.*, 64:1955–1958, 1990.

Chapter 7

Future work and conclusions

7.1 Introduction

The purpose of this chapter is to give an outline of future work that has been made possible from the work in this thesis, and to provide an overall conclusion to the study.

7.2 Future work

7.2.1 Large-scale simulations

Although it has been shown that successful shock wave simulations are possible with just a few thousand atoms, there are a number of areas that are unable to be investigated. Large-scale simulations involving many hundred of thousands of atoms are capable of being simulated on modern supercomputer clusters. These simulations are desirable as they reveal features not available to the small systems such as atomic dislocations as well as crack propagation. The role of crack propagation is unable to be modelled in the systems studied here, and so large-scale simulations are required. Multi-thousand atom simulations are best performed (if not exclusively) on supercomputing resources. Therefore the focus of future work should be in allowing the current molecular dynamics code to be optimised for parallelisation to distribute the workload across the many nodes available. In any parallel computer code, the bottleneck in the speed of computation is the time it takes to perform the serial parts of the code. The BFGS algorithm for geometry optimisation is currently both serial and memory intensive which created an upper limit on the size of systems that could be investigated. Future work should focus on replacing this algorithm with a parallel version that is essential to allow for large-scale simulations to be performed.

7.2.2 Extension to BKS potential

It has been evident that shock waves in quartz produce pressure in excess of the maximum allowable pressure using the functional form of the BKS potential of van Beest *et al*. [1990]. Therefore a number of researchers have adopted various schemes to fit a repulsive potential for these higher pressures. In this thesis a polynomial approach was discussed that was analytically fitted at the point of inflection. This polynomial is by no means unique, and future work should investigate the effects this has on high-pressure quartz and also to investigate higher-order polynomials for the fitting, possible based on experimental data to provide a physical justification. However, the form of the extension proposed in equation 5.5 works well for the high-pressure Hugoniot of shock loaded quartz by comparison to experimental data.

7.2.3 Re-parameterisation of the BKS potential

The extension to the BKS potential at high-pressures could yield good results, however it is not based on any physical assumptions. Re-parameterising the BKS potential over a variety of pressures to *ab initio* density functional theory calculations of quartz gives the potential a physical basis, albeit within the errors of DFT. The original BKS potential was first derived using a mixture of Hartree-Fock calculations on a cluster of silicon dioxide, with experimental results also used in the fit. It is expected that DFT would perform much better than this approach and the work presented in this thesis gives this assertion credence. Future work could re-visit the same technique by the BKS authors but using DFT plus more recent experimental data to create a potential that mitigates some of the current failings of the original BKS empirical potential. The functional form of the potential used for force fitting could be also investigated. Choosing a functional form that has a strong core repulsion (for example a Lennard Jones type potential) to fit the high-pressure DFT data could yield a potential that would never fail if the atoms got too close together. Experimental data could also be used in the fitting procedure to constrain the potential to give realistic responses at high-pressures.

7.2.4 Shock unloading

This work considered shock loading and analysis of the shocked state. Investigating the physics involved in shock unloading and the relaxation mechanisms involved would provide a rich area to explore. One such method of obtaining the state that a system would be in a long time after the shock wave has passed through is known as a Hugoniostat [Maillet *et al*., 2001]. The Hugoniostat is an equilibrium molecular dynamics method that uses perturbed equations of motion that obey the Rankine-Hugoniot re-

lations. In this way, the equilibrium MD simulations result in the long-time relaxed structure after shock compression. A Hugoniostat has been used with some success by Ravelo *et al*. [2004] and Barmes *et al*. [2006] although it has not yet been applied to materials other than Lennard-Jonesium.

7.3 Conclusions

Experimental shock waves have been studied for many years with great success. These have given researchers creating computer simulations results to work towards re-creating. The advantages of computer simulations are manifold: being able to perform experiments on various time scales and over an endless range of materials quickly and cost-effectively to name but a few. Atomistic simulations can obtain information on the structure of the material and have been shown to also give good agreement with the macroscopic properties of materials obtained from experiment. The limiting factor for an atomistic computer simulation of shock waves lies in the choice of the interatomic potential. All interatomic potentials have been parameterised on either experimental data, *ab initio* data or sometimes a mixture of both. It is unlikely that any potential that has been designed to work well for equilibrium properties will also work well under conditions far from equilibrium.

Hydrostatic compression simulations were performed using the interatomic pair potential as parameterised by van Beest *et al*. [1990], which has been used successfully to model the equilibrium properties of quartz. This potential when coupled with a quasi-Newton geometry optimisation technique known as the BFGS algorithm [Broyden, 1970; Fletcher, 1970; Goldfarb, 1970; Shanno, 1970] was found to give the lowest stable state of β-quartz. However, it is known that α-quartz is the lowest stable state. The optimised structure underwent a second-order phase transformation at 8 GPa to α-quartz. This hydrostatic compression was continued until the BKS potential was unable to model the system due to the interatomic distances being so small that the spurious attractive region of the BKS potential was reached. This point was reached at 50 GPa and therefore it was concluded that any shock wave simulation that reached pressures beyond this were no longer using the BKS potential but a correction term that researchers have fitted to the BKS potential. These fits have no physical reasoning and therefore are not guaranteed to correctly model the high-pressure dynamics of quartz. The failure of the BKS potential has led some researchers to use alternative potentials [Tsuneyuki *et al*., 1988] or to re-parameterise the potential for their particular problem [Carre *et al*., 2008]. Re-parameterisation of the pair part of the potential has its merits as the original potential was parameterised using a mixture of *ab initio* Hartree-Fock calculations and experimental data on clusters. Density functional theory calculations have performed much better than Hartree-Fock and have given accurate descriptions of

matter, therefore using data from these calculations should result in a much better potential for quartz. This approach was used in this thesis, using the same functional form for the BKS potential. The resultant parameters for the re-parameterised BKS potential correctly gave the most stable equilibrium state (T=0, P=0) of quartz as α-quartz, although it did not perform well for the high-pressure polymorphs. It was concluded that the re-parameterisation was an improvement over the original BKS potential for the low pressure polymorphs, but further high-pressure configurations were required to be used as input configurations for the fitted procedure. This would improve the performance of the BKS potential for the high-pressure phases. The re-parameterised potential also allowed pressures up to 70 GPa to be achieved before requiring the use of an extension to prevent the system becoming infinitely attractive, which gained a further 20 GPa (+40%) on the original BKS parameterisation.

Shock wave simulation is an exciting and vibrant field with much work ongoing with experimentation and at the mesoscale. The complete spatial scales have still yet to be exploited fully, but with the advancement of large-scale computing coupled with modern computer simulation techniques the gaps between the atomistic and mesoscale, and the mesoscale and macroscopic will diminish, opening up the possibilities of explaining on all spatial scales the properties of matter. It is hoped that then shock wave simulations on ever more complex materials will be achievable.

References

F. Barmes, L. Soulard, and M. Mareschal. Molecular dynamics of shock-wave induced structural changes in silica glasses. *Phys. Rev. B*, 73:224108, 2006.

C. G. Broyden. Convergence of single-rank quasi-Newton methods. *Math. Comput.*, 24:365, 1970.

A. Carre, J. Horbach, S. Ispas, and W. Kob. New fitting scheme to obtain effective potential from Car- Parrinello molecular-dynamics simulations: Application to silica. *Europhys. Lett.*, 82:17001, 2008.

R. Fletcher. A new approach to variable metric algorithms. *Comput. J.*, 13:317, 1970.

D. Goldfarb. A family of variable-metric methods derived by variational means. *Math. Comput.*, 24:23, 1970.

J. B. Maillet, M. Mareschal, L. Soulard, R. Ravelo, P. S. Lomdahl, T. C. Germann, and B. L. Holian. Uniaxial Hugoniostat: A method for atomistic simulations of shocked materials. *Phys. Rev. E*, 6302:016121, 2001.

R. Ravelo, B. L. Holian, T. C. Germann, and P. S. Lomdahl. Constant-stress Hugoniostat method for following the dynamical evolution of shocked matter. *Phys. Rev. B*, 70:014103, 2004.

D. F. Shanno. Conditioning of quasi-Newton methods for function minimization. *Math. Comput.*, 24:647, 1970.

S. Tsuneyuki, M. Tsukada, H. Aoki, and Y. Matsui. First-principles interatomic potential of silica applied to molecular dynamics. *Phys. Rev. Lett.*, 61(7):869–872, Aug 1988. doi: 10.1103/PhysRevLett.61.869.

B. W. H. van Beest, G. J. Kramer, and R. A. van Santen. Force-fields for silicas and aluminophosphates based on *ab initio* calculations. *Phys. Rev. Lett.*, 64:1955–1958, 1990.

Appendix A

The Rayleigh line

The Rayleigh line comes from considering a Hugoniot. It is the straight line that connects the initial state of the material with the final state of the material. The equation for the Rayleigh line is derived from the Rankine-Hugoniot conservation relations. Here, u_0 is the initial particle velocity, U_s is the velocity of the discontinuity (shock front), u_p is the piston velocity that creates the discontinuity, V_0 and P_0 are the initial velocity and pressure (if initial conditions, we have no external pressure, then $P_0 = 0$).

From the equation of conservation of mass:

$$V = V_0 \left(\frac{U_s - (u_p - u_0)}{U_s} \right) \tag{A.1}$$

Noting that $V_0 = 1/\rho_0$ then

$$U_s V \rho_0 = U_s - (u_p - u_0) \tag{A.2}$$

Multiply by $\rho_0 U_s$

$$V {U_s}^2 {\rho_0}^2 = {U_s}^2 \rho_0 - \rho_0 U_s (u_p - u_0) \tag{A.3}$$

Using this with the equation of conservation of momentum:

$$P = P_0 + \rho_0 U_s (u_p - u_0) \tag{A.4}$$

we get:

$$V {U_s}^2 {\rho_0}^2 = {U_s}^2 \rho_0 - (P - P_0) \tag{A.5}$$

Re-arranging,

$$\begin{aligned} P - P_0 &= U_s{}^2\rho_0 - V U_s{}^2\rho_0{}^2 && \text{(A.6)} \\ &= U_s{}^2\rho_0{}^2\left(\frac{1}{\rho_0} - V\right) \\ &= U_s{}^2\rho_0{}^2(V_0 - V) && \text{(A.7)} \end{aligned}$$

For Rayleigh Line from equilibrium initial conditions, we have $P_0 = 0$ therefore the equation becomes:

$$P = U_s{}^2\rho_0{}^2(V_0 - V) \tag{A.8}$$

Figure A.1 shows a schematic of a Rayleigh line.

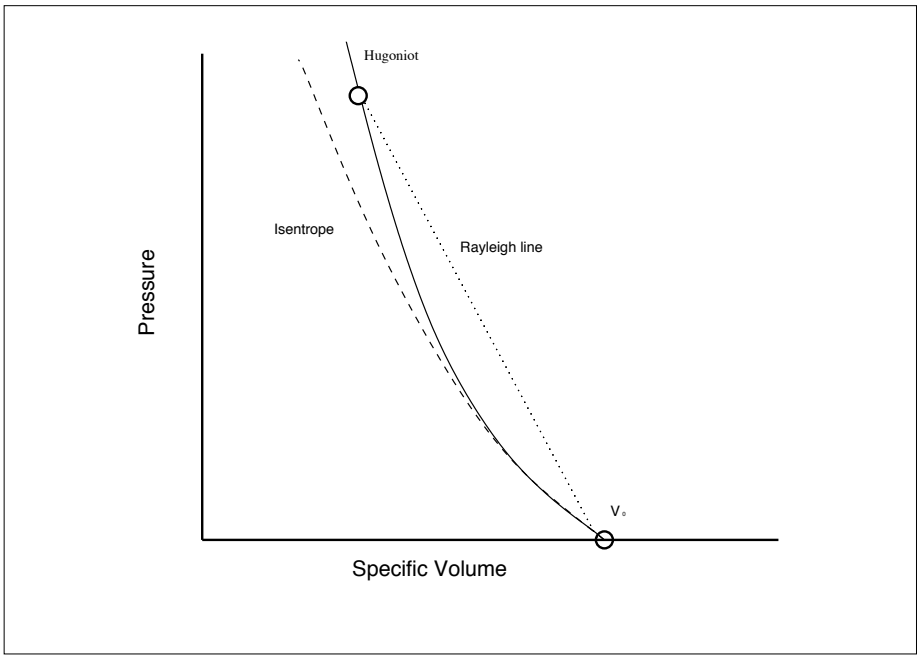

Figure A.1: Schematic of a Rayleigh line.

Appendix B

Ewald summation method

In this section a detailed description of the Ewald summation method is given. This method is used to calculate the long-range electrostatic forces in a simulation by surrounding each point charge with a set of "screening" Gaussian charge distributions. These distributions are then compensated in the simulation by another set of Gaussian charge distributions. The Ewald method first evaluates the electrostatic contribution to the potential energy, in Fourier space, due to the background charge then for the spurious "self" charge - the interaction between the point charge and the compensating charge distribution and finally, in real-space, the contribution from the screened charges.

The Ewald summation method makes use of the properties of a Gaussian charge distribution of the form:

$$\rho_G(r) = -q_i \left(\frac{\alpha}{\pi}\right)^{\frac{3}{2}} e^{-\alpha r^2} \tag{B.1}$$

The energy of a charge distribution is given by solving Poisson's equation for the electrostatic potential. It is convenient to solve this in reciprocal space, making use of the Fourier transformation. Poisson's equation in CGS notation is:

$$-\nabla^2 \phi(\mathbf{r}) = 4\pi\rho(\mathbf{r}) \tag{B.2}$$

where the charge density $\rho(\mathbf{r})$, for a collection of point charges is

$$\rho(\mathbf{r}) = \sum_{i=1}^{N} q_i \delta(\mathbf{r} - \mathbf{r}_i) \tag{B.3}$$

As the system is periodic, we can use the Fourier series:

$$\mathrm{f}(\mathbf{r}) = \frac{1}{V}\sum_{\mathbf{l}=-\infty}^{\infty} \tilde{\mathrm{f}}(k)e^{i\mathbf{k}\cdot\mathbf{r}} \tag{B.4}$$

where V is the volume of the system, $\mathbf{k} = (2\pi/L)\mathbf{l}$ and $\mathbf{l} = (l_x, l_y, l_z)$ the lattice vectors in Fourier space. The Fourier coefficients, $\tilde{f}(k)$ are calculated using:

$$\tilde{\mathrm{f}}(k) = \int_V d\mathbf{r}\mathrm{f}(\mathbf{r})e^{-i\mathbf{k}\cdot\mathbf{r}} \tag{B.5}$$

In Fourier space, Poisson's equation becomes:

$$-\nabla^2\phi(\mathbf{r}) = \frac{1}{V}\sum_{\mathbf{k}} k^2\tilde{\phi}(\mathbf{k})e^{i\mathbf{r}\cdot\mathbf{k}} \tag{B.6}$$

and the charge density becomes:

$$\rho(\mathbf{r}) = \frac{1}{V}\sum_{\mathbf{k}} \tilde{\rho}(\mathbf{k})e^{i\mathbf{r}\cdot\mathbf{k}} \tag{B.7}$$

Substituting the above into equation B.2 gives the Poisson equation in Fourier space:

$$k^2\tilde{\phi}(k) = 4\pi\tilde{\rho}(k) \tag{B.8}$$

For a collection of point charges, P each with a charge density given by equation B.3, we can write:

$$\tilde{\rho}_P = \sum_{i=1}^{N} q_i e^{-i\mathbf{k}\cdot\mathbf{r}} \tag{B.9}$$

Substituting in the Green's function, $\tilde{g}(k)$ for a unit charge:

$$\tilde{g}(k) = \frac{4\pi}{k^2} \tag{B.10}$$

we find that the energy of a charge distribution is given simply by multiplying $\tilde{g}(k)$ by $\tilde{\rho}(k)$ for all k vectors. The electrostatic potential at a point r_i due to a charge distribution given by a periodic sum of Gaussians is:

$$\rho(r_i) = \sum_{j=1}^{N}\sum_{\mathbf{n}} q_j \left(\frac{\alpha}{\pi}\right)^{\frac{3}{2}} e^{\left[-\alpha|\mathbf{r}-(\mathbf{r}_j+\mathbf{n}L|^2\right]} \tag{B.11}$$

Fourier transforming this charge density we get:

$$\rho(\mathbf{k}) = \sum_{i=1}^{N} q_j e^{-i\mathbf{k}\cdot\mathbf{r}_j} e^{\left(\frac{-k^2}{4\alpha}\right)} \tag{B.12}$$

Using Poisson's equation, we get

$$\phi(\mathbf{k}) = \frac{4\pi}{k^2} \sum_{j=1}^{N} q_j e^{-i\mathbf{k}\cdot\mathbf{r}_j} e^{\left(\frac{-k^2}{4\alpha}\right)} \tag{B.13}$$

and by Fourier transformation,

$$\begin{aligned} \phi(\mathbf{r}) &= \frac{1}{V} \sum_{\mathbf{k}\neq 0} \phi(\mathbf{k}) e^{i\mathbf{k}\cdot\mathbf{r}} \\ &= \sum_{\mathbf{k}\neq 0} \sum_{j=1}^{N} q_j e^{-i\mathbf{k}\cdot\mathbf{r}_j} e^{\left(\frac{-k^2}{4\alpha}\right)} \end{aligned} \tag{B.14}$$

Hence the potential energy due to this charge distribution is given by

$$\begin{aligned} U &= \frac{1}{2} \sum_{i=1}^{N} q_i \phi(r_i) \\ &= \frac{1}{2} \sum_{\mathbf{k}\neq 0} \sum_{j=1}^{N} \frac{4\pi q_j q_i}{V k^2} e^{-i\mathbf{k}\cdot\mathbf{r}_j} e^{\left(\frac{-k^2}{4\alpha}\right)} \\ &= \frac{1}{2V} \sum_{\mathbf{k}\neq 0} \tilde{g}(k) |\rho(\mathbf{k})|^2 e^{\left(\frac{-k^2}{4\alpha}\right)} \end{aligned} \tag{B.15}$$

This contribution to the potential includes the "spurious" term that comes from the interaction between the point charge located at the center of the Gaussian charge distribution and the Gaussian charge distribution itself. Poisson's equation can again be used to give:

$$-\frac{\partial^2 r\phi_G(r)}{\partial r^2} = 4\pi r \rho_G(r) \tag{B.16}$$

By integration,

$$\begin{aligned} r\phi_G(r) &= \int_0^r \int_\infty^r 4\pi r \rho_G(r) dr^2 \\ &= \int_0^r \left\{ -2\pi q_i \frac{\alpha}{\pi}^{\frac{3}{2}} \int_r^\infty e^{-\alpha r^2} dr \right\} dr \\ &= -2q_i \frac{\alpha}{\pi}^{\frac{1}{2}} \int_0^r e^{-\alpha r^2} dr \qquad \text{(B.17)} \\ &= q_i erf(\sqrt{\alpha} r) \qquad \text{(B.18)} \end{aligned}$$

where $erf(x)$ is the error function. This, computed at the center of the Gaussian charge

distribution ($r = 0$) is:

$$\rho_G|_{r=0} = 2q_i\frac{\alpha}{\pi}^{\frac{1}{2}} \tag{B.19}$$

Therefore the spurious energy contribution is:

$$U_s = \frac{\alpha}{\pi}^{\frac{1}{2}}\sum_{i=1}^{N} {q_i}^2 \tag{B.20}$$

This term does not depend on particle positions, and therefore provided that the values of the charges remains constant during a simulation, then this term too remains constant. This term needs to be subtracted from the sum of both the real-space and Fourier space contributions to the (Coulomb) potential energy.
The final part of the Ewald method requires the computation of the energy associated with point charges screened by oppositely charged Gaussian charge distributions. From the result of equation B.17 we can write down the electrostatic energy for this:

$$\begin{aligned}\phi_{screened}(r) &= \frac{q_i}{r} - \frac{q_i}{r}erf(\sqrt{\alpha}r) \\ &= \frac{q_i}{r}erfc(\sqrt{\alpha}r)\end{aligned} \tag{B.21}$$

where $erfc(x)$ is the complementary error function. The contribution to the Coulomb potential energy is thus:

$$U_{screened} = \frac{1}{2}\sum_{i\neq j}^{N}\frac{q_i q_j erfc(\sqrt{\alpha}r)}{r_{ij}} \tag{B.22}$$

Therefore the total electrostatic contribution to the potential energy is:

$$\begin{aligned}U_{Coulomb} &= \frac{1}{2V}\sum_{\mathbf{k}\neq 0}\tilde{g}(k)|\rho(\mathbf{k})|^2 e^{\left(\frac{-k^2}{4\alpha}\right)} \\ &- \frac{\alpha}{\pi}^{\frac{1}{2}}\sum_{i=1}^{N}{q_i}^2 \\ &+ \frac{1}{2}\sum_{i\neq j}^{N}\frac{q_i q_j erfc(\sqrt{\alpha}r)}{r_{ij}}\end{aligned} \tag{B.23}$$

Appendix C

Methodology for a shock wave simulation

This appendix gives the steps necessary for a successful shock wave simulation.

Choosing the system

As with all simulations the choice of system will determine the steps.

A simulation cell can be obtained from many different sources, such as the literature, dedicated databases of structures or even made up from scratch. The most important thing to remember is the choice of the potential - does it accurately reflect the high-pressure response of the material? Is it well established or new?

Optimisation

Once a system has been chosen, it is a good idea to test the potential by running a geometry optimisation on the bulk system. The questions that need answering in this step are: Did it optimise? i.e. is the structure stable and well behaved? Does it give the equilibrium properties of the material chosen?

Create a shock wave simulation cell

The shock wave simulation cell has a free surface at the opposite end to where the momentum mirror will be located (usually chosen to be at maximum z). Therefore a vacuum gap must be added to the system that is greater in length than the maximum cut-off range of the potential. Another consideration at this stage is to whether the

system's atoms have charge. i.e. will there be a long-range electrostatic force in the system? If so then the Ewald correction scheme of Yeh and Berkowitz must be used for correcting the long-range forces. This simulation cell should then be geometry optimised to ensure no residual forces remain in the system. The momentum mirror is then placed as z=0 and these atoms are to remain fixed into position during the shock wave simulation.

Shock velocity and the simulation

The system should be ready to perform shock wave simulations. Once a piston velocity has been chosen, each atom in the system is given this velocity so as to move each atom towards the momentum mirror. The shock wave simulation can now be performed.

Appendix D

Paper presented in New Models and Hydrocodes for Shock Wave Processes in Condensed Matter 2008

Shock wave simulations of alpha-quartz

M.R.Farrow and M.I.J.Probert
Department of Physics, The University of York, York, YO10 5DD, United Kingdom

Abstract

Silicon dioxide is one of the most abundant minerals in the Earth's continental crust and is thought to comprise a large part of the Earth's mantle where it is at high-pressures and temperatures. There are several high-pressure phases associated with silicon dioxide and there is still some debate where the phase boundaries lie. With this in mind, this paper presents the results of shock compression simulations of alpha-quartz and a comparison with experimental data.

Introduction

Silicon dioxide, SiO_2, is most commonly known as quartz and is the second most abundant mineral in the Earth's crust. It is thought to comprise a large part of the Earth's mantle where it is at high-pressures of up to 136GPa and high-temperatures up to 1200K. At room temperature, quartz is naturally found in the α-quartz phase, where each silicon atom is 4-fold coordinated with the oxygen atoms. Quartz has a number of high-pressure polymorphs, with coesite and stishovite the most well-known, the latter being 6-fold coordinated. It is also known that quartz becomes amorphous between 25 to 35 GPa at 300K using static experiments, such as diamond anvil cells [4]. However, there is still some debate about where the phase boundaries between the high-pressure polymorphs lie, and to the mechanisms that underlie such phase changes. Computer simulation is a powerful technique that is now widely used to study many materials. Modern computing power has allowed for million atom calculations to be performed on the latest supercomputers. However, such calculations are still rare and most research is performed on a smaller scale. Large-scale, empirically determined potentials are still the mainstay of this research as *ab-initio* calculations are still too computationally expensive to perform. In our study we have used atomistic molecular dynamics (MD) applied to the non-equilibrium state achieved during a shock compression of quartz using a well-known empirical potential.

Simulation details

We used non-equilibrium molecular dynamics (NEMD) in the micro-canonical ensemble (NVE) with 3-D periodic boundary conditions (PBC). The interatomic potential chosen was the so called BKS potential of Van-Beest, Kramer and Van-Santen [7]:

$$U(r) = \sum_{i>j} \frac{q_{\alpha i} q_{\beta j}}{r_{ij}} - \sum_{i>j} \left[\mathbf{A}_{\alpha i \beta j} exp(-\mathbf{b}_{\alpha i \beta j} r_{\alpha i \beta j}) - \frac{\mathbf{C}_{\alpha i \beta j}}{r^6_{\alpha i \beta j}} \right] \qquad (1)$$

where α and β are atomic species, q, is their charges and **A**, **b**, and **C** are constants derived from fitting to Hartree-Fock *ab-initio* calculations and selected empirical measurements. These force-field parameters have been shown to be reasonably successful in describing the dynamic and structural properties of quartz and some of its polymorphs [9, 6]. We used cut-off radii of 2.0 Å and 6.0 Å for the silicon-oxygen bonds and oxygen-oxygen bonds, respectively. The long-range Coulomb forces were calculated by Ewald summation and the pairwise forces only operated over oxygen-oxygen and silicon-oxygen bonds. The BKS potential has an unphysical maxima in the pair-potential at small bond lengths, corresponding to high-compressions that can occur during shock simulations. Several methods have already been employed to correct for this behaviour: Barmes *et al* [1] have used a 2nd order polynomial, whereas Guissani and Guillot [3] have added a Lennard-Jones type potential to the BKS. We chose a form similar to the latter method, and have replaced the pair potential part of the BKS potential at small bond lengths with the following polynomial form:

$$U(r) = \frac{\mathbf{D}_{\alpha i \beta j}}{r^2_{\alpha i \beta j}} + \frac{\mathbf{E}_{\alpha i \beta j}}{r^6_{\alpha i \beta j}} + \mathbf{F}_{\alpha i \beta j} \qquad (2)$$

where **D**, **E** and **F** are calculated analytically to match the BKS pair potential and derivatives at its point of inflection. Table 1 gives numerical values of these parameters and figure 1 shows the form of the potential.

Table 1: Numerical values of the parameters used for correcting the BKS pair potential at small bond lengths

$\alpha\beta$	$\mathbf{D}_{\alpha\beta}(eV\mathring{A}^2)$	$\mathbf{E}_{\alpha\beta}(eV\mathring{A}^6)$	$\mathbf{F}_{\alpha\beta}(eV)$
Si-O	24.1700	23.8086	-3.5872
O-O	12.3435	18.9662	-6.9426

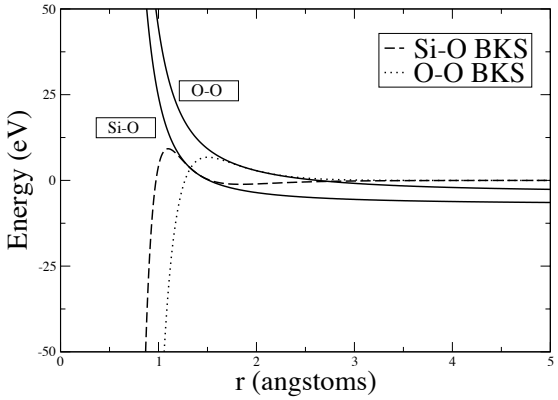

Figure 1: Plot of the interatomic potential used in this work. Dashed lines show the unphysical behaviour of the original BKS potential at small interatomic distances.

Periodic boundary conditions (PBC) in all directions were used throughout, and a shock wave was created in the system by using the so-called momentum mirror technique [5]. The mirror was located at z=0. All atoms in the system were given a "piston velocity" of $-U_p$ towards the momentum mirror. A shock wave thus propagated in the positive z direction at velocity U_s. Our systems incorporated a vacuum gap in the z-direction which was created to be larger than the cut-off radii to ensure that the potential was not acting on atoms through the momentum mirror. This initially creates a large dipole moment in the system that needed to be removed in order to get a stable system. Our system is essentially periodic in 2-D and finite in the shock direction. In order to overcome this problem we adopted a correction to the 3-D Ewald summation technique as proposed by Yeh and Berkowitz [11]. They showed that their correction to 3-D is much more computationally efficient than using a 2-D Ewald summation technique. Figure 2 shows how the 3-D corrected Ewald summation gives the long-range limit convergence of the 3-D Ewald summation technique. Thus it is clear that a small vacuum gap will give the same answers as that of the infinite limit, i.e. a non-periodic in the z-direction system.

Their energy correction, J($\mathbf{M}$,P) is shape dependent and depends on the Ewald summation geometry, P. $\mathbf{M}$ is the total dipole moment and is given by:

$$\mathbf{M} = \sum_{i=1}^{N} q_i \mathbf{r}_i \tag{3}$$

Our system had the geometry of a rectangular plate (P=R) and our

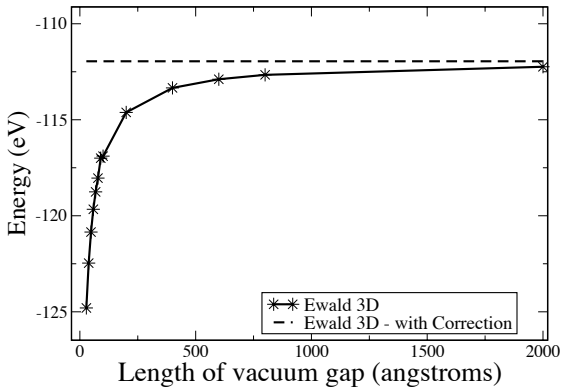

Figure 2: How the energies of Ewald 3-D with correction for 2-D systems gives the same value as the long-range limit of the 3-D Ewald summation technique.

energy correction term is given by

$$J(\mathbf{M}, R) = \frac{2\pi}{V} M_z^2 \tag{4}$$

A correction is also applied to the force calculation, which is obtained by differentiation of the energy term. The system was geometry optimised using a BFGS technique to ensure a stable system prior to shock wave simulation. This optimisation removed the dipole moment of the system by rotating the surface layers whilst leaving the main bulk of the system unaltered. Figure 3 shows the radial distribution function (RDF) of the system prior to shock wave simulation initiation. The structure is that of α-quartz.

The system studied contained 486 atoms of α-quartz ($3 \times 3 \times 6$ unit cells). The system was equilibrated to 300K using a Berendsen thermostat then further equilibrated for 2 ps using standard NVE dynamics before the shock wave was initiated. The shock wave simulations ran until the system reached the shocked state which typically took up to 2 ps.

Results

The resulting Pressure-Volume Hugoniot for the shock compression calculations are shown along with experimental data from Wackerle [10] in figure 4.

It can be seen that the Hugoniot lies lower than the experimental data, indicating a softer response than expected. One possible reason for the softer

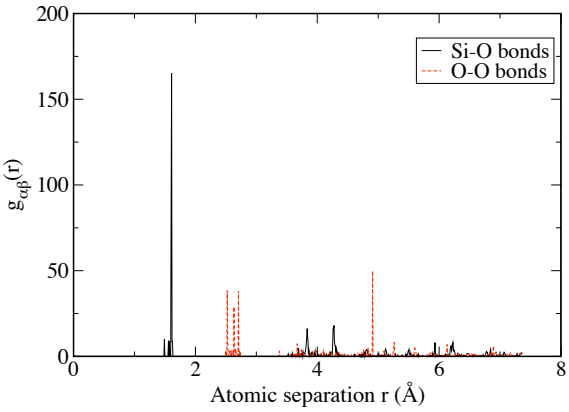

Figure 3: Radial Distribution Function of α-quartz prior to shock compression

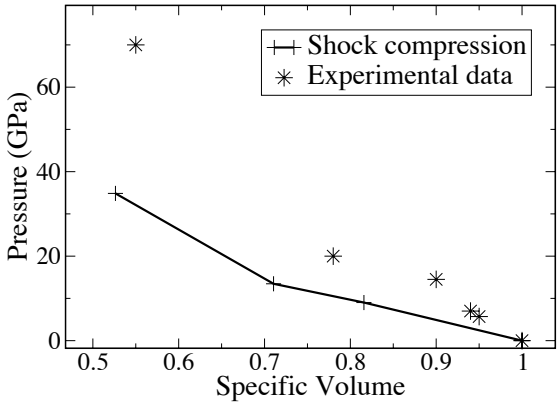

Figure 4: P-V Hugoniot of α-quartz. Experimental data from Wackerle [10]

response is that the momentum mirror used was that of a perfectly reflecting, infinite mass and zero temperature piston. This is not realistic and may be the reason for the larger compressions for lower pressures we observe in figure 4. We shall test this assumption in the future by creating a softer momentum mirror replacing the piston with a few unit cells of α-quartz to act as the momentum mirror [2]. This method will have the advantage of creating a piston that interacts with the system via the interatomic potential. Figure 5 shows the piston, U_p and shock, U_s velocity Hugoniot. As can be seen from the figure, our piston and corresponding shock velocities are very large. This is similar to that of a meteorite impact. Meteorites have a mean impact velocity of between 17 -20 km/s but can be as low as 10 km/s [8]. A near linear dependance can be seen, with the deviation from linear probably a result of finite size effects.

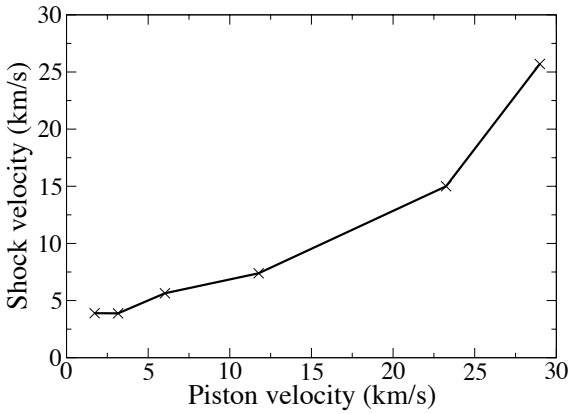

Figure 5: Up-Us Hugoniot of α-quartz

We found that at maximum shock compression, the system was in an amorphous state as can be seen from the RDF in figure 6. This was generated from a shock wave that was initiated by a 3 km/s piston velocity, that corresponds to half the speed of sound in α-quartz.

Conclusion

We have performed atomistic MD shock compression simulations on α-quartz with the aim determining into which high-pressure phase the system transforms. We chose the so-called BKS interatomic potential. In order to avoid complications with the unphysical maxima of the BKS potential we created a polynomial expression with an analytically determined fit to the

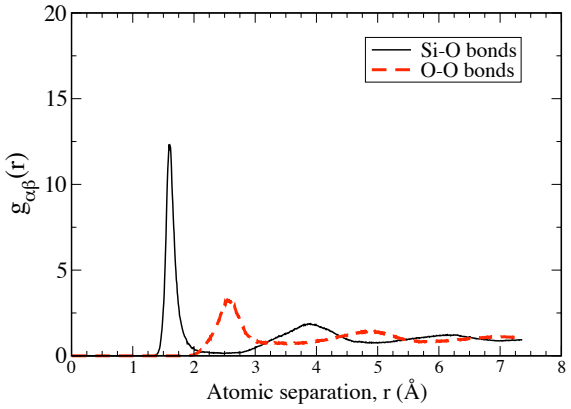

Figure 6: Radial Distribution Function of α-quartz at maximum shock compression using a 3 km/s piston velocity

BKS potential's point of inflection and its derivatives. Our analysis of the radial distribution functions showed that the shock compression transforms α-quartz into an amorphous phase. This was using a piston velocity of 3 km/s, corresponding to only half the sound velocity of bulk α-quartz. We found that in order to create a realistic simulation using the standard MD technique of PBC, a vacuum gap larger than the cut-off radii of the inter-atomic potential should be used to removed any spurious interactions between atoms either side of the momentum mirror. This vacuum gap means that charged systems require a correction to the long-range energies and forces to maintain equilibrium. In this study, we adopted the Ewald summation correction for 3-D systems as proposed by Yeh and Berkowitz due to its computational efficiency over a 2-D Ewald summation. We found that this correction gave a successful geometry optimisation prior to the shock compression calculations without changing the structure of the system.

Finally, we found that the although momentum mirror implementation (that of an infinitely massive piston) tended to underestimate the Hugoniot, a reasonable agreement was evident. Possible reasons for this underestimation could be the momentum mirror was too hard. We plan to test this in the future by replacing the mirror with unit cells of the material to be shocked. This would lead to interaction with the material and the piston via the empirical potential. Another possible reason for the underestimation of the Hugoniot is that of finite size effects. We will test this in the future by using a much larger simulation cell.

Acknowledgements

The authors would like to thank the Engineering and Physical Sciences Research Council (EPSRC) and the Institute of Physics for their financial support.

References

[1] F. Barmes, L. Soulard, and M. Mareschal. Molecular dynamics of shock-wave induced structural changes in silica glasses. *Phys. Rev. B*, 73, 2006.

[2] T. Germann. Private communication, 2008.

[3] Y. Guissani and B. Guillot. A numerical investigation of the liquid-vapor coexistence curve of silica. *J. Chem. Phys.*, 104:7633–7644, 1996.

[4] R. J. Hemley, A. P. Jephcoat, H. K. Mao, L. C. Ming, and M. H. Manghnani. Pressure-induced amorphization of crystalline silica. *Nature*, 334:52–54, 1988.

[5] B. L. Holian. Modeling shock-wave deformation via molecular-dynamics. *Phys. Rev. A*, 37:2562–2568, 1988.

[6] H. Kimizuka, H. Kaburaki, and Y. Kogure. Molecular-dynamics study of the high-temperature elasticity of quartz above the alpha-beta phase transition. *Phys. Rev. B*, 67, 2003.

[7] G. J. Kramer, N. P. Farragher, B. W. H. Vanbeest, and R. A. Vansanten. Interatomic force-fields for silicas, aluminophosphates, and zeolites - derivation based on *ab-initio* calculations. *Phys. Rev. B*, 43:5068–5080, 1991.

[8] H. J. Melosh and G. S. Collins. Meteor crater formed by low-velocity impact - the paucity of melted rock in this crater may be due to the striking projectile's speed. *Nature*, 434:157–157, 2005.

[9] V. V. Murashov and I. M. Svishchev. Quartz family of silica polymorphs: Comparative simulation study of quartz, moganite, and orthorhombic silica, and their phase transformations. *Phys. Rev. B*, 57:5639–5646, 1998.

[10] J. Wackerle. Shock-wave compression of quartz. *J. App. Phys*, 33:922, 1962.

[11] I. C. Yeh and M. L. Berkowitz. Ewald summation for systems with slab geometry. *J. Chem. Phys.*, 111:3155–3162, 1999.